

CHARLES UNIVERSITY IN PRAGUE
Faculty of Mathematics and Physics

DOCTORAL THESIS

2010

ALIAKSEI VETUSHKA

CHARLES UNIVERSITY IN PRAGUE
FACULTY OF MATHEMATICS AND PHYSICS



DOCTORAL THESIS

**Mechanical and Electrical Properties of
Microcrystalline Silicon Thin Films**

**Studied by Raman microspectroscopy and combined atomic
force microscopy**

by

Mgr. Aliaksei Vetushka

Prague, December 2010

A dissertation submitted in partial satisfaction of the requirements for the post-graduate degree of Charles University, Prague, Czech Republic

Mechanical and Electrical Properties of Microcrystalline Silicon Thin Films.

Supervisor:

RNDr. Antonín Fejfar, CSc.

Institute of Physics, Academy of Sciences of the Czech Republic

Consultants:

prof. RNDr. Ivan Pelant, DrSc.

RNDr. Jan Kočka, DrSc.

Institute of Physics, Academy of Sciences of the Czech Republic

Prague, December 2010

Acknowledgements

The major part of this work was done at the Department of Thin Films, Institute of Physics, Academy of Sciences of the Czech Republic in Prague.

First of all I would like to thank my supervisor, RNDr. Antonín Fejfar, CSc. for his unprecedented help and support during the whole time since I arrived in Prague, for his guidance during the research and writing of this thesis.

I would like to thank my colleague and friend RNDr. Martin Ledinský, PhD. for all kind of the accompaniment and assistance during Raman microspectroscopy measurements, for fruitful discussions of physical problems and measurements. I would also like to thank Ing. Tomáš Mates, PhD. for his thoroughness and patience during the introduction to the AFM measurement techniques and image processing. I want to express my thanks to Ing. Jiří Stuchlík, CSc. and Ing. Ha Stuchlíková, CSc. for the preparation of samples and various technical assistance.

I am very grateful to all my colleagues from the Department of Thin Films who shared their results and contributed to the completion of this work. My thanks belong to RNDr. Bohuslav Rezek, PhD. for providing advanced instruction of various AFM techniques and physical discussions, RNDr. Kateřina Kůsová, PhD. for help with L^AT_EX, Ing. Emil Šípek CSc. for the co-operation on combined AFM, prof. RNDr. Ivan Pelant, Dr.Sc. and RNDr. Kateřina Dohnalová, PhD. for all their help with experiments, Ing. Jiří Červenka, PhD. for assistance with Ultra High Vacuum AFM measurements, RNDr. Jan Čermák, PhD., Shinya Honda, PhD., Ing. Vladimír Cháb, CSc., Mgr. Pavel Shukrynau, PhD., and Mgr. Martin Švec, PhD. for teamwork in the AFM laboratory and Veronika Kalusová for numerical calculations and comparing with experimental data. My big thanks go to our secretary Petra Šnajdrová.

I greatly appreciate the assistance of Ing. Jiří Vyskočil, CSc. and Ing. Andrea Mašková (Urbanová) from HVM Plasma s.r.o. for the help with confocal microscopy experiments.

I am also indebted to colleagues from other departments and institutions, especially to prof. RNDr. Tomáš Šikola CSc. and his groups members: Ing. Miroslav Bartošík, PhD. for the assistance with local anodic oxidation experiments, Ing. Ondřej Tomanec for consultations and sample preparation.

Special thanks belong to RNDr. Jan Kočka Dr.Sc., the head of the Department of Thin Films and Nanostructures for his excellent ideas, many of which are the basis of this work.

Last but not least, I would like to express grateful thanks to my whole family for a great support during my doctoral studies.

Abstract

Amorphous and nano- or micro- crystalline silicon thin films are intensively studied materials for photovoltaic applications. The films are used as intrinsic layer (absorber) in p-i-n solar cells. As opposed to crystalline silicon solar cells, the thin films contain about hundred times less silicon and can be deposited at much lower temperatures (typically around 200 °C) which saves energy needed for production and makes it possible to use various low cost (even flexible) substrates.

However, these films have a complex microstructure, which makes it difficult to measure and describe the electronic transport of the photogenerated carriers. Yet, the understanding of the structure and electronic properties of the material at nanoscale is essential on the way to improve the efficiency solar cells.

One of the main aims of this work is the study of the structure and mechanical properties of the mixed phase silicon thin films of various thicknesses and structures. The key parameter of microcrystalline silicon is the crystallinity, i.e., the microcrystalline volume fraction. It determines internal structure of the films which, in turn, decides about many other properties, including charge transport and mechanical stability. Raman microspectroscopy is a fast and non-destructive method for probing the microstructure. The factors which can influence the measurement are considered for the case of silicon thin films. The method of crystallinity evaluation by the Raman microspectroscopy is described. It is also shown that Raman mapping can be done with very high resolution which sometimes can overcome the resolution limit due to optical diffraction.

The Raman spectroscopy can not only distinguish amorphous tissue from microcrystalline grains but it also provides information about local stress in the film, which has a special importance for the properties and stability of the films on flexible substrates. We introduced an original setup for the stress creation in which the silicon films were deposited on the AFM cantilevers and then bent by a micromanipulator to introduce an extrinsic stress. We demonstrated that the positions of the Raman peaks changed linearly with the applied stress both for amorphous and microcrystalline silicon and we were able to compare the same film in stressed and relaxed states.

Another aim of this work was the microscopic study of the charge transport in hydrogenated microcrystalline silicon with nanometer resolution. The final part of the thesis covers the results of the conductive atomic force microscopy (C-AFM) study. Thin films of microcrystalline silicon were studied both in coplanar configuration as well as in "sandwich" setup. Results of C-AFM made in ultra high vacuum and in ambient atmosphere are discussed and compared, including the local I-V characteristics. It was demonstrated that in ambient atmosphere (under which the silicon film is covered by a layer of native oxide and thin layer of condensed water) the C-AFM measurement itself may change the properties of measured sample due to the local anodic oxidation and charge trapping at the interface between silicon and its oxide. It was shown how both these processes can lead to artifacts which can fundamentally change character of the conductive maps, leading for example to the appearance of conductive rings at the grain edges. We have identified the neighboring line oxidation as the origin of this artifact which occurs even upon the first scan of a pristine surface. We also show how to avoid these artifacts. To support our conclusions the native oxide was stripped away by HF acid and we demonstrated that after the etching the character of maps of local currents measured in ambient air became comparable to the maps measured in ultra high vacuum.

Abstract

Amorfni a nano- nebo mikro- krystalické tenké vrstvy křemíku jsou intenzivně studované materiály pro fotovoltaické aplikace. Jsou používány jako intrinsické vrstvy (absorbéry) v p-i-n solárních článcích. V porovnání se solárními články založenými na deskách řezaných z krystalického křemíku, tenkovrstvé články obsahují asi 100x méně křemíku a mohou být deponovány při výrazně nižších teplotách (typicky okolo 200 °C). To umožňuje ušetřit energii nutnou pro výrobu a dovoluje použití různých levných (i ohebných) podložek.

Nicméně, tyto vrstvy mají komplexní mikrostrukturu, která komplikuje měření a popis elektronického transportu fotogenerovaných nosičů náboje. Pochopení struktury a elektronických vlastností materiálů v měřítku nanometrů je přitom zásadní na cestě ke zlepšení účinnosti tenkovrstvých solárních článků.

Jedním z hlavních cílů této práce je studium strukturních a mechanických vlastností smíšených tenkých vrstev křemíku s různými tloušťkami a strukturou. Klíčovým parametrem mikrokrytalického křemíku je krystalinita, tj. objemový podíl mikrokrytalické fáze. Ten určuje interní strukturu vrstvy, která rozhoduje o mnoha dalších vlastnostech jako je transport náboje a mechanická stabilita. Ramanovská mikrospektroskopie je rychlá a nedestruktivní metoda pro měření mikrostruktury. Faktory, které pro případ tenkých vrstev křemíku mohou ovlivnit měření, jsou v práci podrobně diskutovány. Je zde také popsána metoda pro výpočet krystalinity z Ramanovských spekter. Ukázali jsme také, že ramanovské mapování může být provedeno s velmi vysokým rozlišením, které v některých případech může překonat omezení dané optickým difrakčním limitem.

Ramanovská spektroskopie může nejen rozlišit amorfni fázi od mikrokrytalických zrn, ale také poskytnout informace o lokálním pnutí ve vrstvě, které je důležité pro vlastnosti a stabilitu vrstev na ohebných podložkách. Zavedli jsme originální způsob vytváření mechanického pnutí, kdy křemíkové vrstvy deponujeme na AFM raménka, která pak ohýbáme pomocí mikromanipulátoru a vytváříme tak dodatečné (extrin-sické) pnutí. Ukázali jsme, že pozice Ramanovského pásu se mění lineárně s aplikovaným napětím pro amorfni a mikrokrytalický křemík. Mohli jsme tak porovnat také stav vrstvy pod napětím a v relaxovaném stavu.

Dalším cílem této práce byla mikroskopická studie transportu náboje v hydrogenovaném mikrokrystalickém křemíku s nanometrovým rozlišením. Poslední část práce popisuje výsledky studia vrstev pomocí vodivostní mikroskopie atomárních sil (C-AFM). Tenké vrstvy mikrokrystalického křemíku byly studovány jak v koplanární, tak v sandwich konfiguraci. Výsledky C-AFM naměřené v ultra vysokém vakuu a na vzduchu jsou diskutovány a porovnány, včetně lokálních I-V charakteristik. Bylo demonstrováno, že na vzduchu (kdy je vrstva křemíku pokryta vrstvou nativního oxidu a tenkou vrstvou zkondensované vody) může samotné C-AFM měření měnit lokální vlastnosti měřeného vzorku díky lokální anodické oxidaci a záchytu náboje na rozhraní mezi křemíkem a jeho oxidem. Ukázali jsme, jak oba tyto procesy mohou vest k artefaktům, které zásadně mění charakter vodivostních map, například ke vzniku prstenců zvýšené vodivosti na hranicích zrn. Odhalili jsme oxidaci sousedních řádků jako zdroj artefaktů, který se objevuje i po prvním měření na dosud nedotčeném povrchu. Ukázali jsme také, jak tomuto artefaktu zamezit. Pro podporu našich závěrů byl odleptán nativní oxid pomocí kyseliny fluorovodíkové. Demonstrovali jsme tak, že po oleptání jsou mapy lokálních proudů měřené na vzduchu porovnatelné s měřením v ultra vysokém vakuu.

Contents

1	Introduction	4
1.1	Thin film silicon solar cells	4
1.2	Outline of the thesis	6
2	Microcrystalline hydrogenated silicon	9
2.1	Structure of amorphous and microcrystalline hydrogenated silicon thin films	9
2.1.1	Amorphous hydrogenated silicon	10
2.1.2	Microcrystalline hydrogenated silicon	11
2.2	Film deposition methods	12
2.2.1	Physical vapor deposition (PVD)	13
2.2.2	Plasma enhanced chemical vapor deposition (PECVD)	14
2.3	Film growth process and the intrinsic stress evaluation	16
2.3.1	Nucleation	17
2.3.2	Origins of film stress	18
2.3.3	Stress induced nucleation	20
3	Raman spectroscopy and local probe techniques	22
3.1	Raman micro-spectroscopy	22
3.1.1	Raman scattering	23
3.1.2	Measurement of Raman spectrum	23
3.1.3	Artifacts of Raman spectroscopy	26
3.2	Atomic Force Microscopy (AFM) based techniques	27
3.2.1	Conductive Atomic Force Microscopy (C-AFM)	28
3.2.2	Artifacts of AFM	30
3.3	Memory effects	32
4	Sample preparation and measurement details	33
4.1	Sample deposition	33
4.1.1	Regular substrates	33
4.1.2	Cantilevers as substrates for thin films	34
4.1.3	Thin film preparation	34
4.2	Raman spectroscopy setup	36
4.2.1	Stress creation and Raman measurements	37
4.3	3-D confocal optical microscopy	37
4.4	AFM characterization	37
5	Raman micro-spectroscopy of $\mu\text{c-Si:H}$	40
5.1	Application of Raman spectroscopy to $\mu\text{c-Si:H}$	40
5.1.1	Spectra of crystalline Si, a-Si:H, and $\mu\text{c-Si:H}$	40
5.1.2	Dependence on the excitation wavelength	40

5.1.3	Crystallinity evaluation	42
5.1.4	Raman mapping with high resolution	43
5.2	Stress investigation and elastic properties of μc -Si:H	47
5.2.1	Position of Raman peak	47
5.2.2	Stress creation	48
5.2.3	Growth stress estimation. Stoney formula	49
5.2.4	Profiling of bent cantilevers by confocal microscopy and curvature calculation	50
5.2.5	Raman spectroscopy of the stressed μc -Si:H thin films	52
	Microcrystalline silicon	52
	Amorphous silicon	53
6	C-AFM of μc-Si:H. Local electrical properties	55
6.1	Charge transport in μc -Si:H	55
6.1.1	Model of charge transport in μc -Si:H	55
6.1.2	Macroscopic measurements of the μc -Si:H resistance	56
6.2	Ultra high vacuum C-AFM	58
6.2.1	Charge trapping	59
6.2.2	Results for in-situ samples	59
6.3	Ambient C-AFM	60
6.3.1	Main difficulties during ambient C-AFM	60
6.3.2	Tip induced LAO during C-AFM on μc -Si:H	62
	Neighbor line oxidation artifact	65
6.3.3	Discussion of C-AFM results affected by LAO	66
6.3.4	Measurement of local I-V characteristics in ambient	67
6.4	HF etch for restoring local electrical properties of the sample	68
6.5	Dependence of local current on the grain dimensions	70
6.6	Coplanar contacts geometry	72
6.6.1	Model for mechanism of charge transport parallel to a substrate	72
6.6.2	Dependence of the average current registered on the different grains at various distances from gold contact	74
7	Conclusions	77
	Bibliography	80
	About the author	87
	Curriculum vitae	87
	List of publications	89

List of abbreviations and symbols:

Deposition	
CVD	chemical vapor deposition
HWCVD	hot wire chemical vapor deposition
PECVD	plasma enhanced chemical vapor deposition
PVD	physical vapor deposition
RF	radio frequency (13.56 MHz)
r_H	hydrogen dilution defined as $r_H = [H_2]/[SiH_4]$
r_d	deposition rate [nm/s]
T_S	substrate temperature [$^{\circ}C$]
T_V	vapor temperature [$^{\circ}C$]
Properties	
α	optical absorption coefficient of a material
d	thickness of the deposited film [nm]
DB	dangling bond
LGB	large grain boundary
σ_D	electrical conductivity
σ_r	total residual stress in the deposited film [GPa]
X_C	crystalline volume ratio [%]
Materials	
a-Si:H	hydrogenated amorphous silicon
μc -Si:H	hydrogenated microcrystalline silicon
Measurement	
AFM	atomic force microscope
C-AFM	conductive atomic force microscope
d_{RCD}	Raman collection depth [nm]
E	Young modulus
FT-IR	Fourier transform infrared spectroscopy
LAO	local anodic oxidation
N_A	numerical aperture
SEM	scanning electron microscope
SERS	surface enhanced Raman spectroscopy
TEM	transmission electron microscope
TERS	tip enhanced Raman spectroscopy
XRD	X-ray diffraction

Chapter 1

INTRODUCTION

1.1 Thin film silicon solar cells

Silicon is the second most common element in the Earth's crust and probably the most studied and used material in the end of the 20th and 21st centuries. It has found large-scale use in all kinds of electronic devices and because of the electronic industry its research is very important.

Thin films of amorphous silicon are used in thin film transistor liquid crystal displays (TFT-LCD) and as light absorber in solar cells. The attractiveness of silicon thin film solar cell is explained by several reasons:

- low material consumption
- low temperature deposition (energy saving)
- high productivity rate
- possibility of deposition onto large area and cheap flexible substrates

Of course, thin film solar cells technology also has its disadvantages. The main issues are low efficiency and Staebler-Wronski effect which reduces initial efficiency of amorphous thin film solar cells. On the contrary, p-i-n (i-intrinsic absorber layer) solar cells with i-layer of microcrystalline silicon thin films don't degrade. Furthermore, it was shown [1], that solar cells with i-layer of mixed phase silicon films have higher efficiency. Further advance of the technology was tandem solar cells (multi-junction devices) which consist of multiple thin films (individual cells with different bandgaps) to capture a larger portion of the solar spectrum. It has to be noted, that microcrystalline silicon has very comprehensive internal structure and till now it is not completely understood.

The solar panels market has a potential to be one of the most rapidly growing fields in the near future, mostly for its universal applicability. Techcet Group (<http://www.techcet.com/>), which specializes in market analysis and technical trend analysis for the semiconductor and related electronics industries, predicts substantial growth of thin film solar cell production in the next years (see Fig. 1.1).

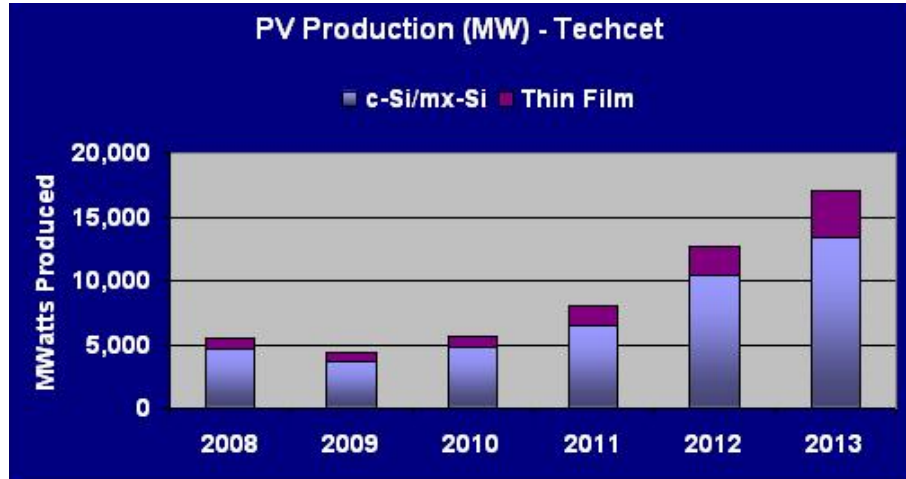


Figure 1.1: Predicted solar cell market growth by Techcet Group, LLC. The growth rate of the thin film solar cell production is expected to be 25 % in the next three years [<http://www.techcet.com/>]

The main obstacle of the solar panels market growth is still a very high initial price of commercially available solar panels. Therefore the main accent of research should be on reducing the cost of solar cell production. The possibility of using cheap substrates (for example, flexible polyethylene terephthalate - PET) is one of the ways how to significantly reduce the price. However, this opens new questions about the role of adhesion, mechanical properties and consequences for performance of devices. Another problem is the proper encapsulation of the solar cell to prevent its damage by the atmospheric humidity.

The main aim of this thesis is to investigate mechanical (elastic) properties of the microcrystalline silicon thin films and the charge transport mechanism at nanoscale. One approach is to use micro Raman scattering to find critical values of applied stress for different materials. Another method is to use atomic force microscopy (AFM) and to combine it with the local current detection in parallel to standard surface morphologies.

1.2 Outline of the thesis

The main emphasis in the thesis is focused on two aspects of studying the intrinsic layer (i-layer) used in the thin film silicon solar cells: *stress* (intrinsic or induced) and *charge transport*. Quality of i-layer has a major impact on the performance of the thin film solar cells. As explained in the previous paragraph, we were motivated by the usage of thin silicon film in solar cells on cheap (and even *flexible*) substrates. So, we mainly focused on the characterization of films prepared at rather low substrate temperatures (at 250 °C and 100 °C) by the conventional Plasma Enhanced Chemical Vapor Deposition (PECVD). Most emphasis will be put on the characterization of samples prepared under different deposition conditions with the aim to understand the relation between the complicated microstructure and electrical properties of these intrinsic layers.

The short introduction to the silicon thin films in the context of solar cells and renewable energy sources above is followed by the *chapter two* starting with the overview of the main structural properties of the amorphous and microcrystalline hydrogenated silicon (Section 2.1). The section 2.2 briefly describes the most common methods for the film deposition - vapor deposition methods and the emphasis is put on the glow discharge technique - Plasma Enhanced Chemical Vapor deposition (PECVD).

A second group of the presented techniques (Sections 3.1 and 3.2) concerns local probing, where the Raman scattering microscopy is introduced and a special attention is paid to the atomic force microscopy (AFM) and mainly its modification – conductive AFM (C-AFM). In this chapter we also consider possible artifacts of measurements and influence of the measurement itself on local properties of the sample and the resulting AFM image.

In the *chapter four* all experimental details are described and summarized. Main parameters of the PECVD depositions, used substrates and holders are given. Experimental setups, technical specifications of the instruments and devices, modes of measurements and settings of all our experiments including the software used are considered in detail. We present our original experimental setup for inducing stress in the thin films of $\mu\text{c-Si:H}$ which enabled us to measure the Raman spectra of the stressed samples.

Next, *chapter five* and *chapter six* contain author's original results. Most of them were published in impacted international scientific journals (see the List of Publica-

tions at the very end of the thesis). Results were selected and arranged with the aim to present the mechanical and electrical properties of mixed-phase Si films.

We discuss how to evaluate a sample crystallinity by Raman microspectroscopy and AFM. We present Raman maps of $\mu\text{c-Si:H}$ with high resolution which allowed us to detect microcrystalline grains as small as 160 nm (below the optical resolution limit). The accent of the *chapter five* was made on the stress investigation in silicon thin films. The dependences of the Raman peak position on the applied compressive stress are shown for microcrystalline as well as for amorphous silicon.

We also focus on local electronic properties of $\mu\text{c-Si:H}$ thin films. We compare C-AFM results measured in ultra high vacuum (UHV) and in ambient air as well. In case of UHV C-AFM measurements, samples were deposited in-situ, i.e., in the chamber which is directly connected to the Omicron AFM/STM microscope enabling the measurements of thin films which were never exposed to air.

The summary of precautions needed to avoid artifacts during Raman and C-AFM study of thin Si films was made.

In order to understand and control the properties of the thin film solar cells (including cells deposited onto flexible substrates), we attempted to study the properties of several series of amorphous and microcrystalline Si thin films prepared by conventional PECVD. We focused on the evolution of structure, influence of the microcrystalline grains on the transport properties and the changes of properties with induced stress. The samples were prepared in the Institute of Physics, Academy of Sciences of the Czech Republic. A complex characterization of these series was performed in our group using various methods, including the methods introduced in the chapter 3 and the results make up the chapters 5 and 6.

The author's contribution was in the designing of experiments, characterization of $\mu\text{c-Si:H}$ samples by AFM in different modes, partially by Raman spectroscopy, stress creation and creating the final interpretation of results obtained by all available techniques.

In the *last chapter* (Conclusions) the most important findings and interesting results of the thesis are summarized and author's personal opinion about an outlook in this field is presented.

Finally, as the last part of the introduction, we will summarize the objectives of the thesis:

- To understand the growth of the silicon thin films with microcrystalline structure.

- To understand the charge transport in intrinsic silicon films and its relation to the microstructure.
- To explore the behavior of thin intrinsic films at different stress conditions
- To summarize practical aspects of the Raman spectroscopy and C-AFM measurements to explain how to avoid artifacts in the resulting images

Chapter 2

MICROCRYSTALLINE HYDROGENATED SILICON

2.1 Structure of amorphous and microcrystalline hydrogenated silicon thin films

Both amorphous and microcrystalline silicon are wide classes of materials with properties strongly dependent on the growth conditions. Thin films of these materials can be deposited using the same deposition method. The layers are deposited at relatively low temperatures (below 400 °C) by plasma enhanced chemical vapor deposition (PECVD) or similar techniques (see below), either from pure silane (SiH_4) or, more commonly, from a mixture of silane and hydrogen. Advantages of the low temperature process are: firstly, a large variety of possible substrates and secondly, the hydrogen is incorporated into the layers, thereby passivating the electronic defects and grain boundaries.

Amorphous silicon absorbs solar radiation much more efficiently than the single-crystal silicon does and a film only about 1 micrometer thick can absorb more than 90 % of the Sun light (photons with energies $> 1.5 \text{ eV}$) shining on it [2]. This is one of the main reasons why the use of thin film silicon could reduce the cost of photovoltaics.

However, the best way of using microcrystalline silicon for photovoltaics appears at present to be in the micromorph tandem [3, 4], i.e. in the combination of a microcrystalline silicon bottom cell with an amorphous silicon top cell due to the optimal band gap combination.

Microcrystalline silicon is still subject of an intense research. Many aspects of the material properties are still being investigated. There is no widely accepted model which completely describes the structure and properties of the μc -Si:H.

2.1.1 Amorphous hydrogenated silicon

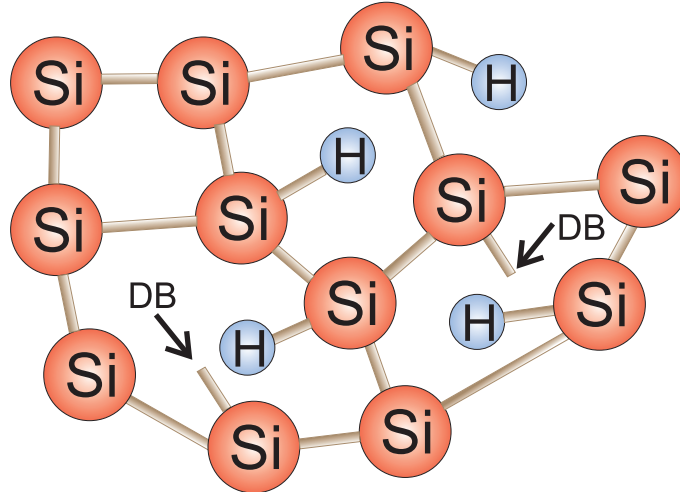


Figure 2.1: *Random structure of the amorphous silicon*

Hydrogenated amorphous silicon (a-Si:H) is a solid state material composed of silicon atoms which are arranged in a lattice lacking far order. Locally, the electronic bonds between neighboring Si atoms in the amorphous network are almost identical to their crystalline counterparts. Such material still shows an electronic density of states which may be compared to the one of crystalline semiconductors (Fig. 2.2). Amorphous silicon, however, has no long range periodicity (Fig. 2.1). As a result, Dangling Bonds (DBs) appear where atoms have no neighbor to which they can bond. These defects provide places for the recombination of the photogenerated electrons and holes, rather than contributing to the electrical circuit. Secondly, they may indirectly influence electronic transport via the electric charge associated with them. But hydrogenation (deposition with the presence of hydrogen - 1 part of SiH_4 to 20 \sim 50 parts of H_2) of the amorphous silicon leads that the hydrogen atoms combine chemically with many of the dangling bonds, which improves charge transport in the material.

Unfortunately not all dangling bonds can be passivated. The remaining ones can be charged either positively (by absence of an electron), they can be neutral (the energy level of such a state as shown in the band diagram corresponds to the electronic

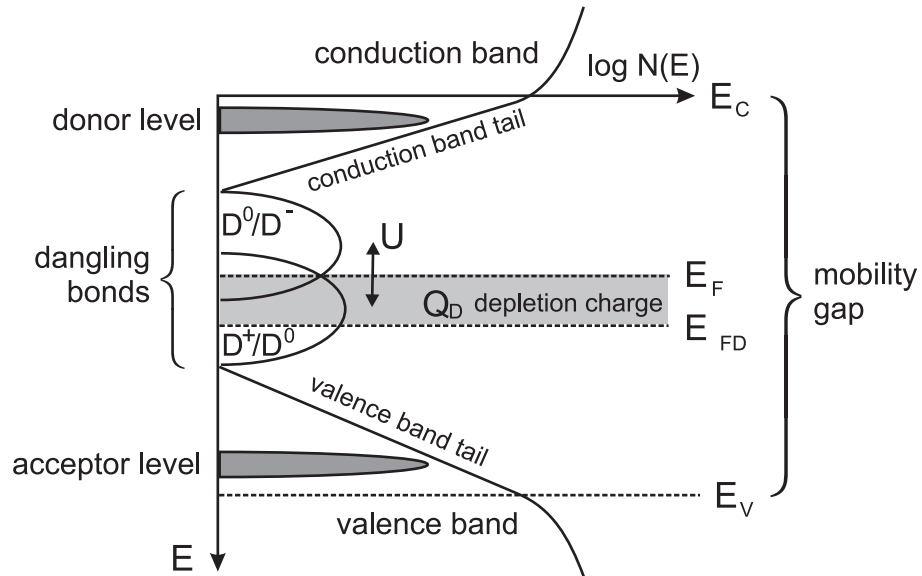


Figure 2.2: The schematic diagram of the density of states distribution in *a-Si:H* showing the conduction band edge (E_C), the valence band edge (E_V), the extended states, tail states, and defect states

transition D^+/D^0) or they can be doubly occupied (the energy level of such a state corresponds to the transition D^0/D^-).

Electronic transport in *a-Si:H* occurs mainly because of extended state conduction and hopping conduction at Fermi energy. Another process is the thermal excitation of the electrons to the conduction band (the activation energy for the amorphous hydrogenated silicon is 0.7 - 0.8 eV, for heavily doped n-type layer the value can be as low as 0.1 eV). For more details see [5].

Instability is the most important disadvantage of the amorphous silicon. These cells experience the Staebler-Wronski effect [6] where their electrical output decreases during exposure to sunlight. Eventually, however, the electrical output stabilizes. This effect can result in up to a 20 % loss in power output before the material stabilizes. Up to now it is not fully understood why this effect occurs. The degradation can be minimized by design of solar cells, but it cannot be completely eliminated because it is an inherent property of hydrogenated amorphous Si.

2.1.2 Microcrystalline hydrogenated silicon

On the contrary, the microcrystalline hydrogenated silicon ($\mu\text{c-Si:H}$) doesn't experience Staebler-Wronski effect and the electrical output of these cells doesn't decrease with time.

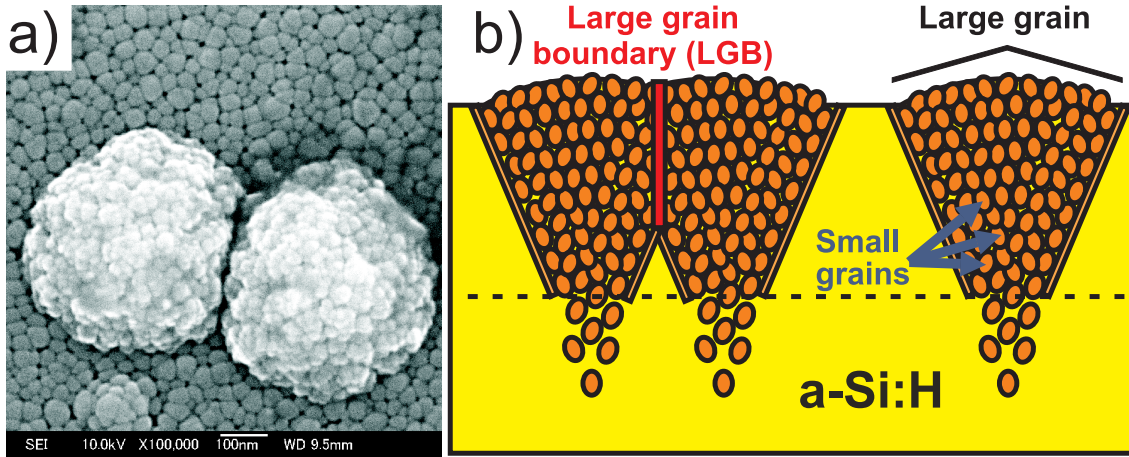


Figure 2.3: a) High resolution scanning electron microscopy image of two microcrystalline conglomerates embedded in amorphous tissue. b) Sketch of the microcrystalline thin film structure showing small nanocrystals and large grains participating in the formation of the structure

$\mu\text{c-Si:H}$ consists of the crystalline phase, made of silicon nanocrystals packed, with some amorphous silicon, into conglomerates (grains). Figure 2.3a shows a plane view of a $\mu\text{c-Si:H}$ grains consisting of silicon nanocrystals with a diameter between 10 and 20 nm, embedded into amorphous silicon. The conglomerates are separated by a varying amount of amorphous silicon, grain boundaries and/or cracks [7]. The cross-sectional sketch of $\mu\text{c-Si:H}$ is shown in Fig. 2.3b, which was constructed by taking into account experimental data from various techniques (such as atomic force microscopy, X-ray diffraction, electron microscopy etc.). This sketch demonstrates the complexity of the internal structure of microcrystalline thin films: in addition to the small nanocrystals, columnar conglomerates and amorphous tissue, there is also the amorphous incubation layer near the substrate, interface between big grains and amorphous tissue (grain edges), and interface between two columnar conglomerates – large grain boundary (LGB). All these factors and the tendency to the oxidation in ambient atmosphere make study of the local electronic properties of $\mu\text{c-Si:H}$ very problematic. Let's consider the growth of such films and describe physical processes and parameters that influence their internal structure.

2.2 Film deposition methods

Physical vapor deposition (PVD) and chemical vapor deposition (CVD) are the most common methods for transferring material atom by atom from one or more sources to the growing surface of a film. Vapor deposition refers to processes in which

materials in a vapor state are transferred to the growing film through condensation, chemical reaction, or conversion to form a solid material. The deposition is normally carried out in a vacuum chamber to control the vapor composition. Many variations of these basic methods have been developed for different strategies addressing the requirements of film purity, structural quality, temperature and other factors [8].

2.2.1 Physical vapor deposition (PVD)

If the vapor is created (by physical means) without a chemical reaction, the process is classified as PVD. It is a technique whereby physical processes, such as evaporation, sublimation or ion impingement on a target, facilitate the transfer of atoms from a solid or molten source onto a substrate. *Evaporation* and *sputtering* are the two most widely used PVD methods [9].

Evaporation In an evaporation process, thermal energy is supplied to a source from which atoms are evaporated for deposition onto a substrate. The simplest method of heating is resistive heating of a wire or stripe of refractory metal to which the evaporated material is attached. The evaporated atoms fly through reduced background pressure in the evaporation chamber and condense on the growth surface. Molecular beam epitaxy (MBE) is an example of an evaporative method. This growth technique can provide film materials of extraordinarily good quality which are ideal for research purposes. However, the growth is very slow compared to other methods.

Sputtering In sputter deposition, ions of a sputtering gas (typically Ar) are accelerated toward the target by electric field [10]. As the ions collide with the cathode, the initial concentration of charge carriers in the system is significantly increased. As the gaseous ions strike the target (the source material from which the film is made) dislodged surface atoms form the vapor in the chamber. These atoms reach the substrate or vacuum chamber wall and condense, thus providing film growth.

Different sputtering methods are widely used: dc sputtering, radio frequency (rf) sputtering, magnetron sputtering, and bias sputtering (small negative bias to substrate reduces contamination of a substrate). The film grain structure made by sputter deposition has many crystallographic orientations without preferred texture. However, evaporative deposition leads to highly textured films with greater grain sizes than that of the sputtered films. Sputter deposition offers better control in maintain-

ing stoichiometry and film thickness uniformity, and has the flexibility to deposit any crystalline and amorphous materials.

2.2.2 Plasma enhanced chemical vapor deposition (PECVD)

PECVD is the mostly used method for the deposition of microcrystalline and amorphous silicon thin films. The method is basically a special form of CVD. The necessary energy for the chemical reaction is introduced by plasma while the temperature of the substrate is kept low. This makes it possible to use substrates which are sensitive to high temperatures (such as polyethylene terephthalate (PET) or common glass).

In the PECVD chamber hydrogen (H_2) and silane gas (SiH_4) are excited by a radio-frequency (13.56 MHz) plasma, which causes molecules to dissociate. As a result, there are free radicals H and SiH_x ($x < 4$) which initiate chemical reaction, resulting in layer formation.

Despite the relative simplicity of the PECVD deposition process, there are many variables which must be controlled to obtain a material with desired properties:

Silane dilution The composition of the source gases (*dilution*) is one of the key parameters of PECVD. Dilution of silane with other gases modifies drastically most aspects of plasma-field and plasma-surface interactions due to different ionization potential, collision cross-sections, ion energy and ion current of the dilution gas compared to silane [11]. Usually, the dilution ratio parameter r_H is defined as the ratio of hydrogen [H_2] and silane [SiH_4] flows [12]:

$$r_H = \frac{[H_2]}{[SiH_4]} \quad (2.1)$$

This dimensionless parameter is related to the structure and electronic properties of the film [13]. To make a rough description of the influence of this parameter, let's assume the typical deposition with next parameters: substrate temperature of 250 °C, pressure in the chamber 70 Pa and 13.56 MHz rf-frequency. In case of high silane concentration ($r_H < 10$) the layer tends to be fully amorphous. At the same time such dilution increases the band gap of the a-Si:H. In case of high hydrogen concentration ($r_H > 40$) the layer tends to be fully microcrystalline [14]. Somewhere between these extreme values there is an interval of values of dilution that leads to the mixed structure of the layer. Solar cells with the highest efficiencies are usually deposited near the transition between amorphous and microcrystalline structures. This effect was also observed in other laboratories, see for example [15, 16].

Temperature The next very important parameter is the *substrate temperature* T_S . Low deposition temperature significantly decreases the cost of the thin films, moreover it allows the use of the cheaper plastic substrates, for example PET. The substrate temperature strongly influences the mobility of precursors on the surface, promoting their diffusion, desorption and chemical reactions, thus affecting the structure and properties of the deposited film. In case of the deposition of the μc -Si:H thin film precursors are moving over the growing film surface and "seeking" the most favorable equilibrium positions to settle. The probability of such process grows with the T_S . At sufficiently high T_S the result is crystalline structure. On the contrary, the low T_S prevents such "seeking" and precursors form the amorphous structure. The same considerations lead to the conclusion that with low T_S the number of DB increases, which is confirmed by experiments [17].

To deposit amorphous layer with minimal defect density the optimal substrate temperature was found to be around 250 °C [18]. Similar temperature was also adopted for the μc -Si:H [19].

But the $T_S = 250$ °C is still too high for the deposition on PET. This motivates many laboratories to look for new ways how to reduce the T_S with retention of the efficiency. Recently, an unexpected physical phenomena has been observed: at $T_S = 140$ °C suppressed oxygen donor formation has been reported by Nasuno et al. [17, 20]. In these works the world record efficiency of 9.4 % of the single junction μc -Si:H solar cell has been achieved. Another excellent result belongs to the group of Schubert who prepared the solar cell on plastic substrate at $T_S = 100$ °C with the efficiency of 6.3 % [21]. Later it was also reported that solar cells with high efficiencies can be prepared even at lower T_S , when the deposition conditions are close to the mixed phase between a-Si:H and μc -Si:H [22, 23].

Time of the deposition This parameter has an influence mainly on the thickness of the growing film. However, during the deposition the plasma parameters and the film growth can evolve [24].

The measurement of the film thickness d allows one to evaluate the deposition rate r_d :

$$r_d = \frac{d}{t} \quad (2.2)$$

where t is the duration of the deposition. The typical values of the r_d during a PECVD deposition of the μc -Si:H are around 0.3 nm/s. That means, in case of the layer deposition with thickness 2 μm the deposition time $t = 100$ min is necessary.

Increasing of the r_d with retention of the efficiency is another challenge for researchers. Some interesting results, which allow increase of the deposition rate more than ten times can be seen in the refs. [25, 26].

Pressure It is the pressure that has decisive influence on the deposition rate. The typical pressure in the chamber during the deposition of a-Si:H and μ c-Si:H thin films is in the range 10 - 100 Pa [27]. Higher pressure increases the total number of the collisions of ions and neutral atoms which leads to the decrease of their energy [23], and also leads to the powder formation (formation of the particles in the discharge) [28]. This effect can be compensated by varying of other deposition parameters, for example, by increasing the discharge power. It was reported, that after the optimization of the deposition parameters the efficiencies of 8.2 % at $r_d = 2.1 \text{ nm/s}$ and 7.9 % at $r_d = 3.0 \text{ nm/s}$ were achieved [29].

Plasma Properties of the plasma also have impact on the growth process of the films. To proceed with the previous paragraph, let's consider the *power* of the discharge. Increasing of this parameter stimulates the dissociation of the silane molecules (until the molecules are completely dissociated). On the other hand, high power leads to higher sheath voltages, and thus higher ion energy. High-energy ions cause defect formation and deterioration in crystallinity [30], decreasing the quality of the solar cell. One of the effective methods to reduce ion energies while maintaining high deposition rates are: firstly, *very high frequency* (VHF) excitation of the discharge (in this case lower peak-to-peak voltages for a given discharge power result in lower maximum-ion energies), and secondly, high working pressure (as considered above).

Another way to reduce ion energies is the use of a third electrode ("mesh"-electrode) in a triode arrangement [31, 32]. With an independent bias on this electrode with respect to the grounded substrate, ion energies can be controllably reduced.

2.3 Film growth process and the intrinsic stress evaluation

The growth process begins with a clean surface of the substrate material, which is at temperature T_S , exposed to a vapor of a chemically compatible film material, which is at the temperature T_V . To form a crystal film, atoms in the vapor must arrive at the substrate surface, adhere to it, and settle into possible equilibrium positions

before structural defects are left behind the growth front. To form an amorphous film, on the contrary, atoms must be prevented from seeking stable equilibrium positions when they arrive to the growth surface.

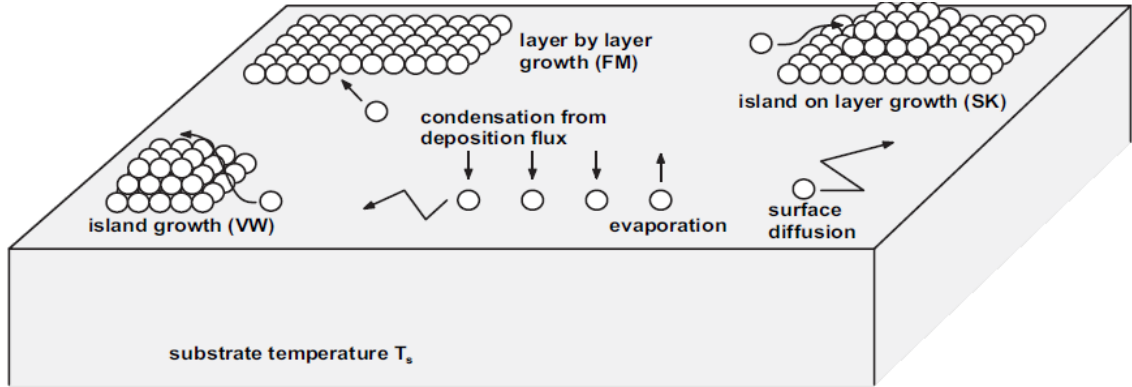


Figure 2.4: Schematic illustration of the film formation on substrates [9]

Atoms that appear very close to the substrate surface form chemical bonds with atoms in the substrate. For this purpose the temperature of the substrate must be low enough so that the vapor phase is supersaturated close to the substrate. Some of the attached atoms, which are called *adatoms*, may return to the vapor if their energies due to thermal fluctuations are sufficient to overcome the energy of attachment, as suggested in the schematic diagram in Figure 2.4 [9]. Once adatoms become attached to the substrate, they form a distribution on the substrate surface having the character of a two-dimensional vapor. The deposited material is believed to thermalize quickly to the temperature T_S .

Each adatom presumably resides within an equilibrium energy well on the surface most of the time, and this well is separated from adjacent energy wells by a barrier of height $E_d > 0$ with respect to the equilibrium position. The atoms oscillate at their positions due to thermal fluctuations and, if they acquire sufficient energy, they can hop into adjacent equilibrium wells. This provides the surface diffusion. For more details of variations of films growth see [9].

2.3.1 Nucleation

The growth surface always has some distribution of surface defects (crystallographic steps, grain boundaries and dislocations) which provide sites of preferable attachment for adatoms. If the diffusion distance is large enough (comparable with the defect spacing), then adatoms tend to find these defects and become attached

to them. This is the case of *heterogeneous* nucleation and growth of films. On the other hand, if the spacing of defects is large compared to the diffusion distance, then adatoms bind together and form clusters. The case of formation of such stable clusters is called *homogeneous* nucleation of film growth. Another feature which is connected to the nucleation is preferred crystallographic orientation. Initial crystallographic orientations of the nascent film which minimize surface and interface energies are favored over others, and the nucleation rates for clusters with lower energy orientations are greater than those for others.

It can be seen from the figure 2.3, that the crystallinity of μc -Si:H layers depends on the depth as the layers consist of the conical conglomerates, which nucleate either on the substrate or, for layers deposited close to the transition, after an initial thin amorphous incubation layer was grown.

It has been shown that the nuclei density of μc -Si:H deposited close to the transition on various flat and rough substrates depends mainly on the chemical nature of the substrate [7]. The local epitaxy is involved in the growth of i-layers onto doped microcrystalline layers (a situation encountered in p-i-n type and n-i-p type devices where the doped layer plays the role of a nucleation layer). Therefore, the first highly microcrystalline doped layer is beneficial in obtaining a high density of nuclei for the subsequent i-layer growth.

One of the most remarkable aspects of μc -Si:H thin film growth is that crystallites grow at temperatures much lower than the silicon melting temperature. The formation of the nanocrystals at such low temperatures is occurring far from equilibrium and consequently involves dynamical aspects. Models allowing one to simulate the growth of crystalline domains are generally based on the point of view of statistical mechanics, but until now no statistical growth model could reproduce the conical shape of the crystalline grains or the observations that growth occurs perpendicular to the local substrate plane. A certain progress in growth numerical simulations is a simple discrete dynamical crystalline growth model inspired by a Potts model which was introduced by group of Arvind Shah (for more details see [33]).

2.3.2 Origins of film stress

Following the initial nucleation of μc -Si:H grains, other stages typically include: grains growth, grain-to-grain contact and coalescence into larger grains, establishment of large area contiguity. In case of fully microcrystalline structure the film consists of many of these grains which are separated from each other by large grain boundaries.

The role of stress in these stages of microstructure evolution is not yet fully understood. However, the application of real-time stress measurement techniques has made it possible to identify some general trends in behavior [34, 35, 36].

In general, residual stress is the internal stress present in material when it is free of applied traction. The presence of residual stress results in that the material is trying to change its in-plane dimensions and/or to become curved. If the internal distribution of mismatch strain is incompatible with a stress-free state, then some residual stress distribution will remain.

Classification of film stresses and stress evolution Film stresses are usually divided into two broad categories. The first category comprises *growth stresses*, which are present in films following growth on substrates. Growth stresses are strongly dependent on properties of the involved materials, as well as on the growth conditions. Non-destructive observational methods for in-situ stress measurement and growth surface monitoring have made it possible to study the evolution of growth surface features and the evolution of average stress during film formation. These methods have led to a subdivision of the category of growth stresses into those stresses which arise during various phases of the growth process. Usually, growth stresses are reproducible for a given process and the values reached at the end of growth persist at room temperature for a long time following the growth. Growth stresses are also commonly called *intrinsic* stresses.

A second category of film stress represents stress conditions arising from changes in the physical environment of the film material. Such externally induced stresses are commonly called *extrinsic* stresses. In many cases, these stresses arise only when the film is bonded to a substrate. However, the distinction between growth stresses and induced stresses becomes hazy at times.

The development of growth or intrinsic stresses for a particular material depends on many factors. Perhaps the most important among these are the bonding to the substrate (epitaxial or not, for example), the mobility of adatoms on the film material itself, and the mobility of grain boundaries formed during growth. Except for the case of ideal epitaxy, the final structure is always metastable. Because of the huge number of degrees of freedom involved in establishing this metastable structure, the final structure can significantly differ from a completely stable equilibrium structure. Many mechanisms of stress generation during film growth take place. Most important of them in case of the thin films of $\mu\text{c-Si:H}$ are: surface and interface stress, grain growth, grain boundary relaxation, and shrinkage of grain boundary voids.

Extrinsic stresses can arise from different physical effects, such as: temperature change with a difference in coefficients of thermal expansion between bonded elements, chemical reactions, stress induced phase transformations, and plastic deformation. For more details see [9].

It has to be noted that the understanding of growth stresses and their origins is far from complete. All of the effects described above surely have impact on the growth stresses, but robust models for comparative estimates of stress magnitudes have remained elusive.

2.3.3 Stress induced nucleation

The origin of the compressive stress in a-Si:H has been attributed to 1) Si or H atoms introduced by ion bombardment [37], 2) H-H repulsive force [38], and 3) H₂ molecules trapped inside a-Si:H [39]. On the contrary, the compressive stress decreases by the formation of microvoids [40] and SiH₂ bonds [41] in the a-Si:H network.

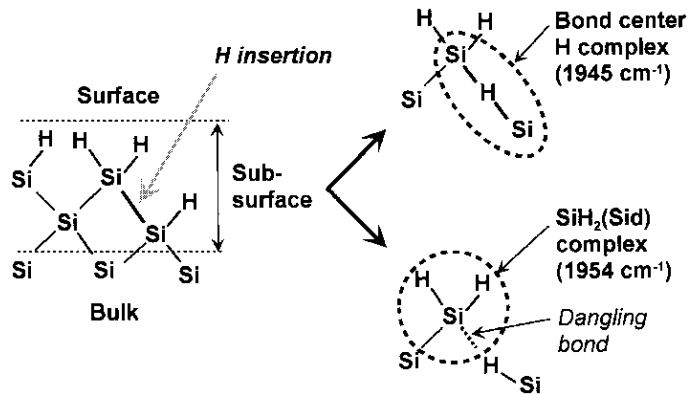


Figure 2.5: Schematic illustration of the SiH_n complex formation reactions in a two-monolayer thick region of a a-Si:H sub surface [42]

The mechanism of the stress induced nucleation of $\mu\text{c-Si:H}$ from amorphous phase was proposed by Fujiwara et al [43, 44]. They propose the stress generation by SiH bond formation (see Fig. 2.5). In the first step of the model, H is inserted into a strained Si-Si bond, generating the compressive stress in the a-Si:H bulk layer. The stress generation by H and the following strained Si-Si bond formation occur successively and increase the compressive stress and the number of strained Si-Si bonds with increasing total film thickness. In the sub-surface region, the increase in the strained Si-Si bond density in turn leads to the creation of more SiH_n complexes by H insertion. When the SiH_n complex concentration becomes high, $\mu\text{c-Si:H}$ nucleation

finally occurs. The nucleation process of μc -Si:H, however, shows a large substrate dependence.

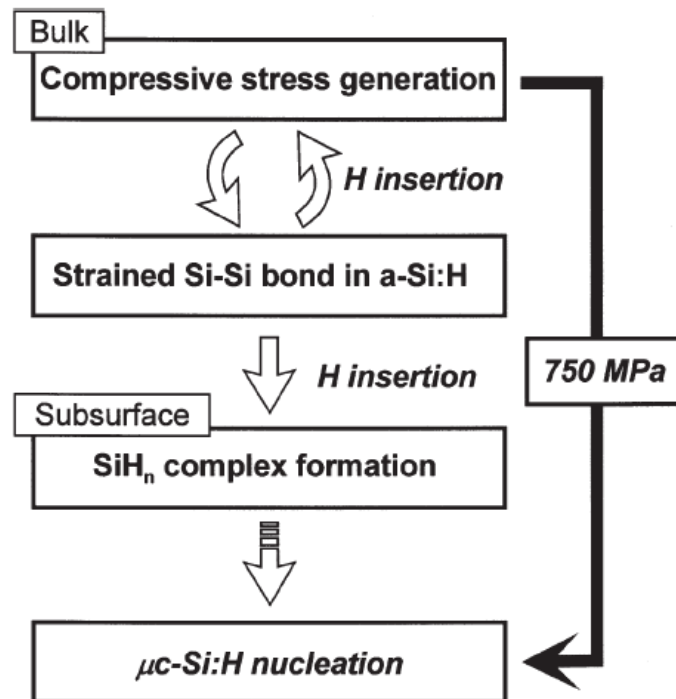


Figure 2.6: Flowchart of stress-induced μc -Si:H nucleation from the a -Si:H phase [43]

Summarized process of the μc -Si:H nucleation is shown in the Fig. 2.6. In [43] μc -Si:H nucleation was observed at ~ 750 MPa.

Chapter 3

RAMAN SPECTROSCOPY AND LOCAL PROBE TECHNIQUES

3.1 Raman micro-spectroscopy

Molecules consist of atoms which have a certain mass and which are connected by elastic bonds. They perform periodic motions around the equilibrium positions, i.e. they have *vibrational degrees of freedom*. All motions of the atoms in a molecule relative to each other are a superposition of so-called *normal vibrations*, in which all atoms are vibrating with the same phase and *normal frequency*. Polyatomic molecules with n atoms have $3n - 6$ degrees of freedom (normal vibrations) and linear ones have $3n - 5$ degrees of freedom, which define their *vibrational spectra*. These spectra depend on the masses of the atoms, their geometrical arrangement, and the strength of their chemical bonds. In a first approximation the normal vibrations do not interact. However, the elasticity of bonds does not strictly follow Hooke's law. Therefore overtones and combinations of normal vibrations appear. Raman spectroscopy is the most important tool for observing vibrational spectra, which provide us with plenty of information:

- The Raman spectra of two molecules are different, if these molecules have different constitutions, isotopic distributions, configurations or if their environments are different for whatever reason. So substances can be identified by their Raman spectra, interpreted like 'fingerprints'
- The spectra consist of certain bands, i.e., characteristic vibrations, which are typical of particular groups of atoms and which are defined by definite ranges of frequencies and intensities in the Raman spectra. The intensities of the bands

in the spectrum of a mixture are usually proportional to the concentrations of the individual components. It is thus possible to determine the relative concentration of one substance.

3.1.1 Raman scattering

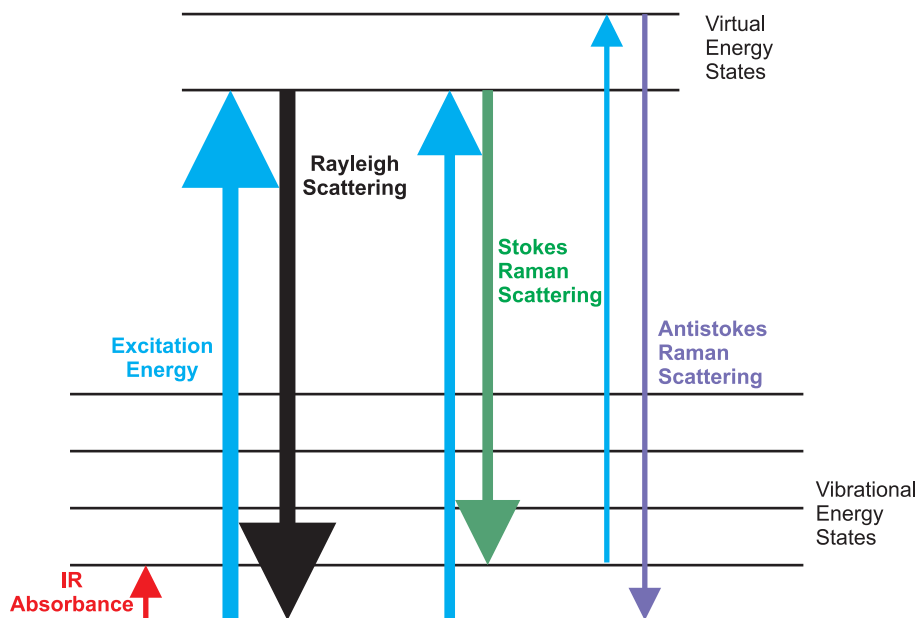


Figure 3.1: Energy level diagram showing the states involved in Raman scattering

The Raman effect occurs when a quantum of light hits a molecule and interacts with the electron cloud and the bonds of that molecule. The photon excites the molecule into a virtual state (see Fig. 3.1). In contrast to the Rayleigh scattering (i.e. *elastic* scattering), the spontaneous Raman effect is *inelastic* process during which a photon energy is exchanged with a molecule. The probability of the inelastic scattering is very low (typically about one photon of 10^7 is inelastically scattered). The Raman process, which transfers vibrational energy to the molecule and releases a light quantum of lower energy (*Stokes* lines in the spectrum), has a higher probability than the reverse process (*anti-Stokes* lines). Therefore Stokes lines are usually recorded as *Raman spectrum*.

3.1.2 Measurement of Raman spectrum

A Raman spectrum is excited by irradiating a sample with monochromatic radiation (usually by gas laser or solid-state laser) in ultraviolet, visible or near-infrared

range. Elastically scattered photons produce the strong Rayleigh line at the frequency of the exciting radiation. Inelastic scattering corresponds to weak lines at frequencies shifted from the frequency of the exciting radiation by certain, well defined frequency, the Raman spectrum. If a coherent radiation with a very high intensity is applied continuously or as pulse, non-linear effects can be observed which produce coherent Raman radiation. This technique is quite different from that of the 'classical' Raman effect, for more information see [45]. It has to be noted that Raman scattering is a coherent process, whereas fluorescence is not.

The classical Raman effect produces very weak signals. There are several techniques which can substantially enhance this effect. For example, the resonance Raman spectroscopy (RRS) is making use of the excitation of molecules in a spectral range of electronic absorption; the surface-enhanced Raman spectroscopy (SERS) employs the influence of small metal particles on the elementary process of Raman scattering. SERS and related technique - tip enhanced Raman spectroscopy (TERS) will be discussed later in this chapter.

There are two main setups for the measurement of classical Raman spectrum:

- *Macro-Raman*: exciting laser beam is not focused on the sample surface, scattered light is detected in backscattering or in 90° geometry. This setup is very effective in case of experiments which take place in solutions and for experiments when it is necessary to excite molecules in big volume, but with lower intensity.
- *Micro-Raman*: exciting laser beam is focused on the sample surface by the objective of optical microscope. The same objective (backscattering geometry) can be used for collecting of scattered light. This setup is used, for example, for strongly absorbing samples, small samples or thin films. But the biggest advantage of this method is the possibility to measure spectrum from very small area (less than $1 \mu\text{m}$ laterally), and/or *mapping* of a sample with such lateral resolution.

Advantages of the Raman probing There are many advantages of the Raman spectroscopy of $\mu\text{c-Si:H}$. The method is:

- very quick
- non-contact, damageless (at appropriate excitation power)

- lateral resolution - less than 1 μm , vertical resolution - tens of nm from the surface
- possibility of advanced combined techniques, such as tip-enhanced Raman, polarized Raman, etc.

Spatial resolution of the Raman mapping Raman micro-spectroscopy is an optical method, therefore its resolution is restricted by the Abbe fundamental limit of optical resolution - Rayleigh criterion R , given as:

$$R = 1.22 \frac{\lambda}{2N_A} \quad (3.1)$$

where λ is the wavelength of the light and N_A is numerical aperture of the used objective.

In general, the resolution of the micro-Raman mapping can be optimized. First of all, one has to choose shorter excitation wavelengths and lenses with higher numerical aperture to increase the resolution ability of the microscope as follows from the Rayleigh formula 3.1.

Second optimization of the optical microscope is using of a very small (tens of μm) pinhole - *confocal microscopy*. The pinhole is placed at intermediate image plane of the microscope. The light passes through the pinhole and is focused by the objective onto the sample surface. The main idea of the method is to illuminate a very small area (dot) only (at this step the illumination of other points is excluded), then the reflected or scattered light (from the illuminated dot only) passes through the objective and the image of the dot is created at intermediate image plane, but only the main diffraction maximum passes through tiny pinhole and one pixel of image is created. As only one point of the sample is illuminated at a time, imaging requires scanning over a regular raster.

Surface-enhanced Raman spectroscopy There are a number of advanced types of Raman spectroscopy, including surface-enhanced Raman, tip-enhanced Raman, polarized Raman which potentially can be used to study thin films of μc -Si:H.

Surface-enhanced Raman spectroscopy (SERS) is a surface sensitive technique, in which Raman scattering by molecules adsorbed on rough metal surfaces is significantly enhanced. The enhancement factor can be as much as 10^{14} - 10^{15} , which allows the technique to be sensitive enough to detect even single molecules [46].

The enhancement of the Raman signal for adsorbates on particular surfaces occurs because of an enhancement in the electric field provided by the metal surface. When the incident light strikes the surface, localized surface plasmons are excited. The field enhancement is greatest when the plasmon frequency, ω_p , is in resonance with the radiation. The incident light can excite a variety of phenomena at the surface. The complexity of this situation can be minimized by surfaces with features much smaller than the wavelength of the light, as only the dipolar contribution will be recognized by the system. The dipolar term contributes to the plasmon oscillations, which leads to the field enhancement. It has to be noted that the field enhancement occurs twice. Initially, the field enhancement magnifies the intensity of incident light, therefore increasing the signal of the Raman scattering. By turn, the Raman signal is then further magnified by the surface, resulting in a greater increase in the total output signal of the experiment [47].

Tip enhanced Raman spectroscopy The phenomenon of SERS can be used to improve the lateral resolution of Raman mapping. The idea is to illuminate the very end of a sharp tip by focused laser beam. The tip can be considered as small particle to enhance the incident light and Raman signal as well. In this case, the signal is enhanced in a very small volume only, while the signal coming from outside of the enhanced region is much smaller.

3.1.3 Artifacts of Raman spectroscopy

As it will be shown in section 5.2, stress in $\mu\text{c-Si:H}$ film as well as phonon confinement effect in the small nanometer-scale crystallites affect the position of Raman peak. This phenomenon is used, for example, for local stress investigation in such films with Raman micro-spectroscopy.

However, one has to keep in mind that these are not the only factors that can affect the position of Raman peak. Some care has to be taken when performing the experiments and while interpreting them. First source of errors is the heating of measured sample by the excitation laser. When too high laser power is used, this may change energy bands and phonons distribution, which leads to a shift of the Raman peak. Especially one must be careful with thin films, because the induced heating at the same output laser power is different than in bulk silicon. Even a difference of only $1\text{ }^\circ\text{C}$ will result in a shift of the Raman peak of about 0.025 cm^{-1} [48]. If small stresses are measured, a difference in heating on different surfaces may falsify

the stress results. To find out whether one is dealing with heating or stress, it is necessary to perform an experiment where the position of Raman peak is measured as a function of the laser power.

Other factors that can affect position of the Raman peak are

- laser instability
- spectrometer instability
- changes of the focusing of the laser on the sample
- temperature variations

Taking into account the fact that in case of crystalline silicon 0.1 cm^{-1} (resolution ability of a good Raman spectroscope) means stress of 50 MPa , the calibration of the instrument is needed. For these purpose peaks from the plasma radiation from the laser can be used. Monitoring of the position of these lines allows one to correct all measured data to eliminate shifts of the Raman signal which have nothing to do with stress.

3.2 Atomic Force Microscopy (AFM) based techniques

Scanning Probe Microscopy (SPM) is a field of microscopy where images of surfaces are constructed by using a physical probe that scans the specimen. During the raster scan of the specimen by the probe, the probe-surface interaction is recorded as a function of position. More detailed description of the applications of the SPM in science and technology can be found, for example, in [49]. Most of scanning probe microscopes can image several interactions simultaneously. The manner of using these interactions to obtain an image is generally called a *mode*. The resolution varies somewhat from technique to technique, but some probe techniques reach atomic resolution. In this work the typical lateral resolution of the rough surface of microcrystalline silicon is about several nanometers.

The atomic force microscope (AFM) is a very high-resolution type of scanning probe microscopy (more than 1000 times better than the optical diffraction limit). The AFM is one of the main tools used in this work.

The AFM consists of a cantilever with a sharp tip (probe) at its end that is used to scan the specimen surface. The cantilever has a tip radius of curvature on the order

of tens of nanometers. When the tip is brought into proximity of a sample surface, forces between the tip and the sample lead to a deflection of the cantilever according to Hooke's law. The image is constructed by "feeling" the surface with a mechanical probe.

Depending on the situation, forces that are measured in AFM include mechanical contact force, van der Waals forces, capillary forces, chemical bonding, electrostatic forces, magnetic forces (see magnetic force microscope, MFM), etc [50]. As well as force, additional quantities may simultaneously be measured through the use of specialized types of probe, for example a local current.

The primary modes of operation are *contact* mode, *semicontact* mode and *noncontact* mode. Contact mode is also called *static* mode while semicontact and noncontact modes are called *dynamic* modes. In the static mode operation, the static tip deflection is used as a feedback signal. Because the measurement of a static signal is prone to noise and drift, low stiffness cantilevers are used. However, close to the surface of the sample, attractive forces can be quite strong, causing the tip to 'snap-in' to the surface. Thus static mode AFM is almost always done in contact where the overall force is repulsive. In contact mode, the force between the tip and the surface is kept constant during scanning by maintaining a constant deflection.

In the dynamic mode, the cantilever is externally oscillated at or close to its fundamental resonance frequency or its higher harmonic. The oscillation amplitude, phase and resonance frequency are modified by tip-sample interaction forces; these changes in oscillation with respect to the external reference oscillation provide information about the sample's characteristics. Schemes for dynamic mode operation include frequency modulation (noncontact mode) and the more common amplitude modulation (semicontact or tapping mode). In frequency modulation, changes in the oscillation frequency provide information about tip-sample interactions. Frequency can be measured with very high sensitivity and thus the frequency modulation mode allows for the use of very stiff cantilevers. Stiff cantilevers provide stability very close to the surface and, as a result, this technique was the first AFM technique to provide true atomic resolution in ultra-high vacuum conditions. For more details see [51].

3.2.1 Conductive Atomic Force Microscopy (C-AFM)

In contact mode, the tip is dragged across the sample surface at a fixed normal force (set point). Feedback system of the microscope keeps the cantilever bent at the same curvature (at the same set-point) by extending or retracting the piezo scanner.

To Z-coordinate of the surface topography at each point corresponds the piezo stretch. If one connects AFM tip and a sample into an electrical circuit, as is shown in the Fig. 3.2, and applies a voltage, it is possible to measure local current simultaneously with the topography. This technique is called *Conductive Atomic Force Microscopy* (C-AFM). In this case the current is flowing through the metal-coated tip of the microscope (C-AFM microscopy uses conventional silicon tips coated with a metal or metallic alloy, such as Pt-Ir) and the conductive sample.

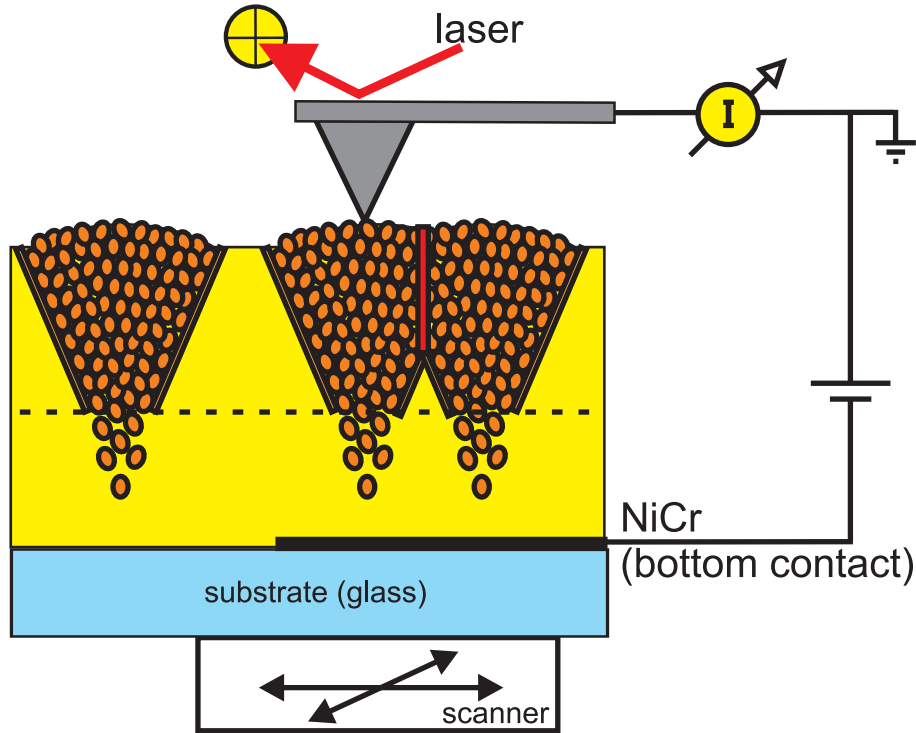


Figure 3.2: *Conductive Atomic Force Microscopy (C-AFM) technique*

Torsional Resonance Tunneling AFM Another modification of this technique is Torsional Resonance Tunneling AFM (TR-TUNATM) technique by Veeco. It allows C-AFM to be used on soft or otherwise delicate samples by using *torsional resonance* mode [52] instead of contact mode. In this case, a cantilever is oscillating along the cantilever's long axis, creating a rotational oscillation. This oscillation causes a dithering motion of the tip. As the probe encounters lateral forces on the sample surface, the corresponding changes in the cantilever's motion are measured. These oscillations take place very near the surface (about 1 nm away from the sample), but the tip doesn't touch it. At the same time the distance between the conductive tip and the conductive sample is short enough for existence of tunneling current between them

in case of non-zero bias voltage. The main advantage of this method is the absence of the physical contact with the sample, which ensures the same properties of the tip during the scan.

Difference between UHV and ambient AFM In case of the *ambient* contact mode C-AFM, the tip is not in direct electrical contact with the sample, because the surface of the $\mu\text{c-Si:H}$ sample is covered by a highly resistive thin oxide layer. So, even in contact C-AFM electrons are tunneling from the sample to the tip through the oxide.

Spectroscopic mode In the *spectroscopic mode*, the tip is stationary, while the voltage is being swept. This allows recording conventional current-voltage characteristics (IV-curves) from tiny areas of the sample, and thereby to extract information on the local electronic properties, such as local density of states [53]. However, in ambient atmosphere it is very complicated to measure repeated results from the same place in a series of measurements, because of the oxidation phenomenon. The practical aspect of the measuring of current-voltage characteristics will be discussed in the section 6.3.4

3.2.2 Artifacts of AFM

When recording images with AFM, surprising and strange results are often achieved. Different *artifacts* can appear due to physical interactions that are totally different from those used for image formation in conventional light and electron microscopy, and so, may not be recognized by users accustomed to conventional microscopy. Paragraphs below describe some common artifacts that occur in AFM, some of these might also occur in STM and other types of Scanning Probe Microscopy.

Piezo artifacts First of all, artifacts arise due to the peculiarities of the piezoelectric scanner. The real position of the piezo scanner is influenced by such effects as creep or hysteresis. This difference between the *desired* and *real* positions can be avoided by using so-called *closed loop* mode. In this mode, the real position of the piezo scanner is continuously measured by position sensors (mostly capacitance sensors) and any deviation from the desired position is corrected. The main disadvantage of closed loop mode is relatively high noise (generated by capacitance sensors) in the measured signal which significantly decreases the quality of the AFM image at fields of scan smaller than $1 \times 1 \mu\text{m}^2$.

Tip artifacts The various artifacts that can occur due to the interaction of the tip with the sample (generally tip-sample convolution). It could be double or triple contours, unexpected height shifts, sudden changes of the resolution in acquired images, etc. The reasons for such artifacts are:

- dirty or contaminated tip
- blunt tip
- double or multiple tips

Depending on the sample, tip can have different lifetime before it will become contaminated, blunt or damaged. It is very important to know what can happen while taking images with the AFM, how one can recognize the presence of the artifact, its origin and then try to avoid it or minimize it. In case of repetition of topographic features, rotation of the sample (not direction of scan) can confirm whether the features are real or tip artifact takes place. To check the sharpness and general state of the used tip it is good idea to use a known sample and make a benchmark measurement on it.

Other artifacts There are a lot of physical processes which can lead to different artifacts. Some of them can be easily defined (for example, sample drift or flying tip due to improper feedback settings), some can't. It is especially difficult to deal with artifacts in advanced measurement techniques, such as Kelvin force microscopy or C-AFM technique.

When coated cantilever is used, there is always a chance to wear off the metal coating deposited onto the standard body of Si cantilever. Thus the observed features could be erroneously related to sample features [54]. In ambient atmosphere the sample surface is always covered by a thin oxide film and water layer as well. These circumstances lead to the fact that AFM measurement itself can change the local properties of the sample. For example, whenever the voltage is applied between an AFM tip and silicon thin film, at least two processes can occur. Firstly, the charge injected by the tip may be trapped in deep states at the sample surface. Secondly, the electric field drives the migration of oxyanions or substrate cations through the surface oxide and leads to the Local Anodic Oxidation (LAO) of Si [55]. Possible artifacts caused by LAO will be considered in detail in section 6.3.2

Finally, various artifacts can be observed on the samples with unknown history of measurements, because some techniques modify the local properties of the sample (see, for example, Fig. 3.3 in section 3.3).

3.3 Memory effects

So called "memory effects" are often observed in various experiments. Such effects are the consequence of the fact that a measurement itself can have an influence on a sample properties, can modify and/or change them. This is of particular importance for local probe microscopic techniques where specific excitation can be very high. It is very important to recognize the influence of an instrument on a sample and make it as low as possible to avoid artifacts.

During our experiments we have had to face another non-obvious artifact. After measuring of the Raman map (see Fig. 5.5 in section 5.1.4) we imaged the same area of the same sample by C-AFM (see Fig. 3.3). Area marked by the white rectangle was previously probed by Raman. Note, that local current flowed through the grains inside the white rectangle was on average 23 fA , while in case of the grains outside the mapped region have average local current about 94 fA .

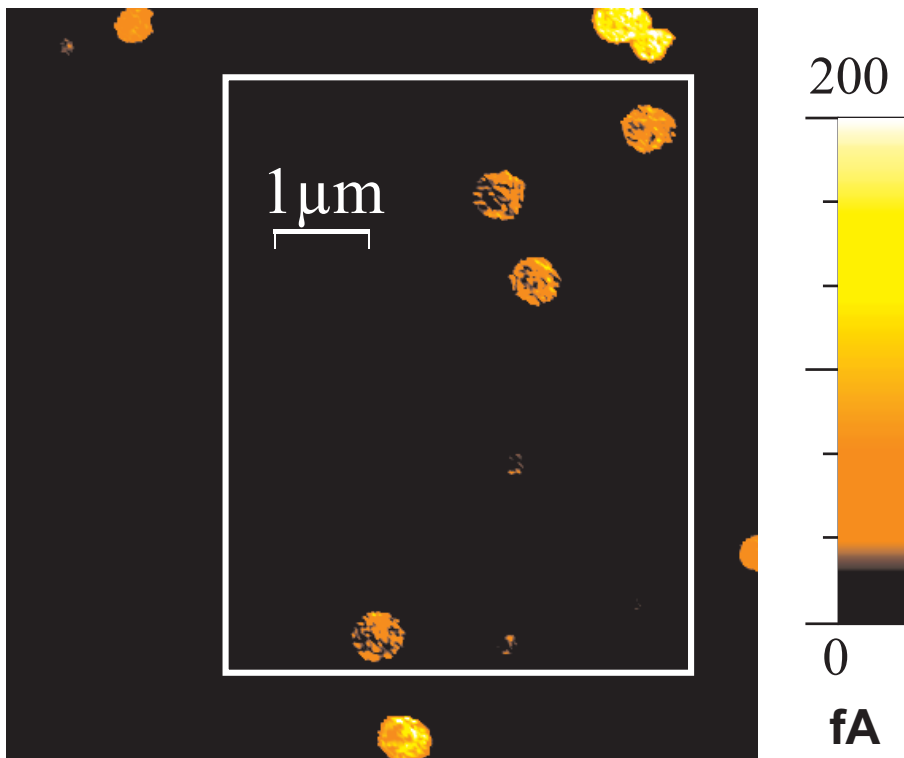


Figure 3.3: Map of local current measured by C-AFM on $\mu\text{c-Si:H}$ sample. White rectangle designates the place where the Raman map excited by 442 nm laser was measured

Chapter 4

SAMPLE PREPARATION AND MEASUREMENT DETAILS

4.1 Sample deposition

4.1.1 Regular substrates

Typical substrates for the studying of $\mu\text{c-Si:H}$ thin films were glass, crystalline silicon, p^+ and n^+ doped crystalline silicon. For measurements of the dark conductivity σ_d of $\mu\text{c-Si:H}$ thin films deposited on glass, two coplanar stripes made of metal with a low work function (e.g. Cr or Ti) are evaporated (see Fig.4.1). We used specialized type of glass - Corning # 7059 glass capable of T_S up to $800\text{ }^\circ\text{C}$. Substrates were cleaned in an ultrasonic bath for ten minutes and then immediately transferred into deposition chamber.

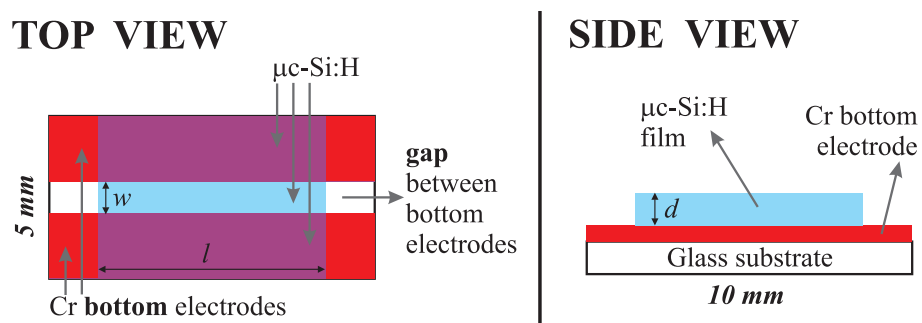


Figure 4.1: Typical design of thin film $\mu\text{c-Si:H}$ sample deposited on glass with a pair of metal bottom electrodes

4.1.2 Cantilevers as substrates for thin films

For stress investigation we used silicon cantilevers as substrates for $\mu\text{c-Si:H}$ thin films because of their excellent elastic properties. The cantilever chips consist of two parts: thick wafer base and the thin cantilever itself. We have chosen AFM-cantilevers for contact mode (the longest type) metalized by PtIr_5 coating from Nanosensors or BudgetSensors companies (see Fig. 4.2).

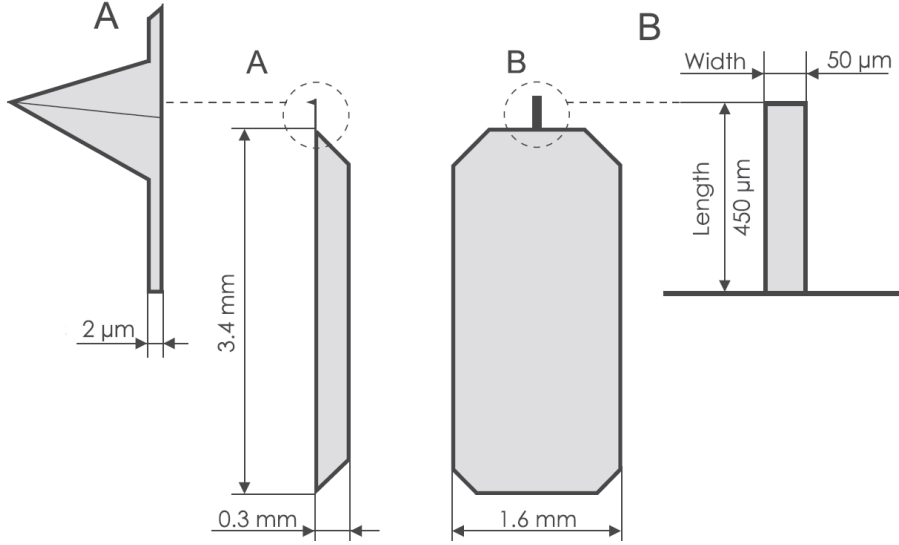


Figure 4.2: *BudgetSensors Cont-E cantilevers (from www.budgetsensors.com)*

BudgetSensors silicon AFM probes are 'carved out' from single crystal silicon wafers with orientation $\langle 100 \rangle$. The wafers are patterned in a micromachining process in order to obtain the desired structures. This is done using the photolithography process described in ref. [56]. The silicon is usually highly doped for higher conductivity in order to improve static charge dissipation. We have used metal coated cantilevers as a substrate to screen strong Raman signal from the silicon cantilever.

4.1.3 Thin film preparation

Thin films of $\mu\text{c-Si:H}$ were prepared by radio frequency (13.56 MHz) PECVD technique in a mixture of silane SiH_4 and hydrogen at discharge frequency 13.56 MHz, the dilution ratio of the gas flows $r_H = H_2/\text{SiH}_4$ varied from 12 for amorphous films to 32 for $\mu\text{c-Si:H}$ samples. For mixed phase samples, the conditions were close to the boundary between the amorphous and microcrystalline growth, resulting in the growth of films consisting of relatively few large conical microcrystalline grains

surrounded by the amorphous tissue. The pressure was around 70 Pa and substrate temperature was 100 °C or 250 °C. Film thickness was determined by using stylus profiler Tencor AlphaStep 100.

In one deposition run we usually deposited $\mu\text{c-Si:H}$ film on several pieces of different substrates (some of them were bare, some were covered with bottom contacts) to be able to perform a complex characterization of the film by several diagnostic techniques introduced in previous sections. Our typical samples are represented in Fig. 4.3.

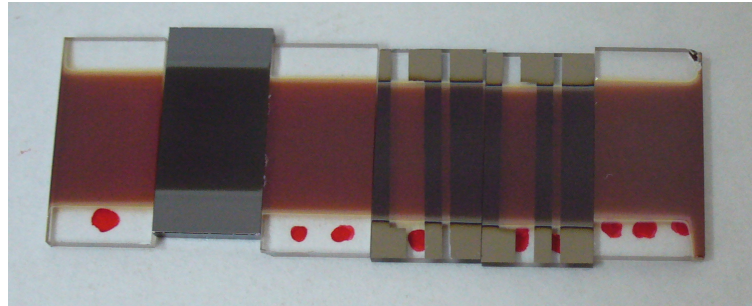


Figure 4.3: Typical samples after a deposition. Used substrates: glass, crystalline silicon, glass with bottom contacts.

For the case of deposition onto cantilevers, holder with cantilevers is shown in Fig. 4.4a, and Fig. 4.4b shows a cantilever after a deposition, which is bent due to the intrinsic stress in $\mu\text{c-Si:H}$ thin film.

During the deposition, the cantilever tips faced the discharge and there was a gap between the cantilever and substrate holder corresponding to the chip thickness ($\sim 300 \mu\text{m}$). The films with thicknesses from 0.2 to 0.6 μm were deposited.



Figure 4.4: Deposition onto cantilevers: a) holder with installed AFM cantilevers; b) a cantilever after deposition is bent due to the intrinsic stress in the deposited $\mu\text{c-Si:H}$ film

4.2 Raman spectroscopy setup

Raman spectra were obtained by Renishaw In Via Reflex Raman microspectrometer (see Fig. 4.5) with near infrared excitation wavelength 785 nm at which the penetration depth d_p for $\mu\text{c-Si:H}$ is greater than the thickness of the film. The wavelength of 325 nm ($d_p < 10\text{ nm}$) and 442 nm ($d_p \sim 50\text{ nm}$) were also used. Intensity of excitation light from the laser can be attenuated from 100% to $10^{-6}\%$ and it was kept low to avoid heating of the sample and artifacts of measurements (see section 3.1.3).

Optical microscope Leica with $100\times$ objective lens in combination with pinhole allows laser spot with minimal dimensions of $1\ \mu\text{m}$ in diameter. Mechanized table Prior ProScan II controlled by the computer (by Renishaw firmware) in combination with 442 nm excitation wavelength provide resolution less than $1\ \mu\text{m}$ in all three axes.

The edge filter of the spectrometer passes Raman signal shifted more than 200 cm^{-1} from the excitation wavelength. Dispersive element of the spectrometer in case of 785 nm laser is a grating with 1200 grooves per mm, and in case of 442 nm laser a grating with 2400 grooves per mm.

Scanning of the sample in Renishaw InVia Reflex Raman microspectrometer is implemented by the movement of the sample stage. The real position of the stage is monitored by capacitance sensors with resolution of $0.1\ \mu\text{m}$.

All spectra were processed by WIRE 2.0 Renishaw software.



Figure 4.5: View of Raman microspectrometer Renishaw InVia Reflex with Leica DMLM microscope

4.2.1 Stress creation and Raman measurements

Extrinsic stress was induced by bending the cantilever with film (see the experimental setup on Fig. 4.6a) by the Kleindiek Nanotechnik nanomanipulator MM3A-EM (Fig. 4.6b). The bending of the cantilever was determined by the position of the optical microscopy focus in the Raman microscopy setup.

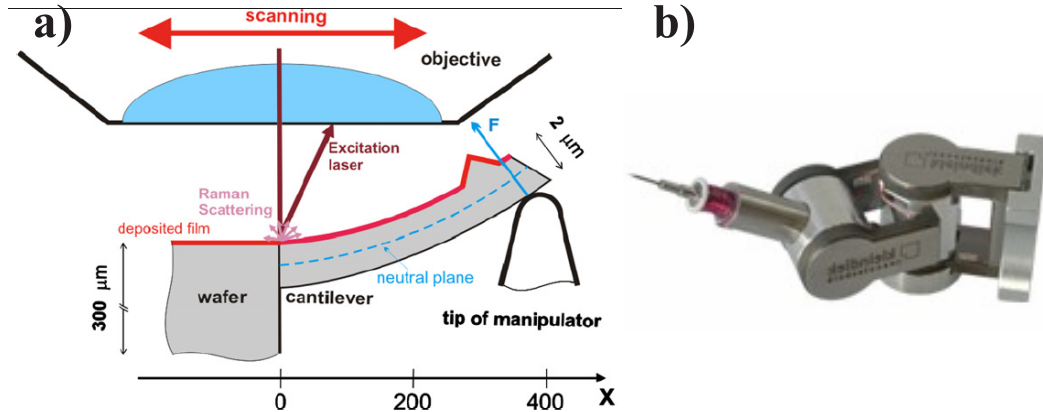


Figure 4.6: a) Experimental setup showing the cantilever coated by Si film bent by the tip of the manipulator. The position of the focal point of the Raman excitation laser was varied along the X-axis; b) View of MM3A Kleindiek Nanotechnik nanomanipulator

Excitation laser was focused by the objective of optical microscope, the same objective was used to collect Raman signal from the sample. We measured the data near the border between solid base and flexible cantilever of the AFM-tip to have a possibility to compare measurements from the stressed part (on cantilever) with non-stressed film (on solid base). The objective with long working distance was used.

4.3 3-D confocal optical microscopy

We used Olympus LEXT OLS3000 confocal microscope (see setup in Fig. 4.7) to obtain 3-D images of bent cantilevers. It allowed us to extract the precise profile of the cantilever at different bending states which were processed using the WSxM software package [57] (see inset in Fig. 4.7).

4.4 AFM characterization

The AFM images in this work were obtained by Omicron UHV AFM/STM (C-AFM, Fig. 4.8a) or by ambient Veeco Dimension DI3100 IV equipped by Extended

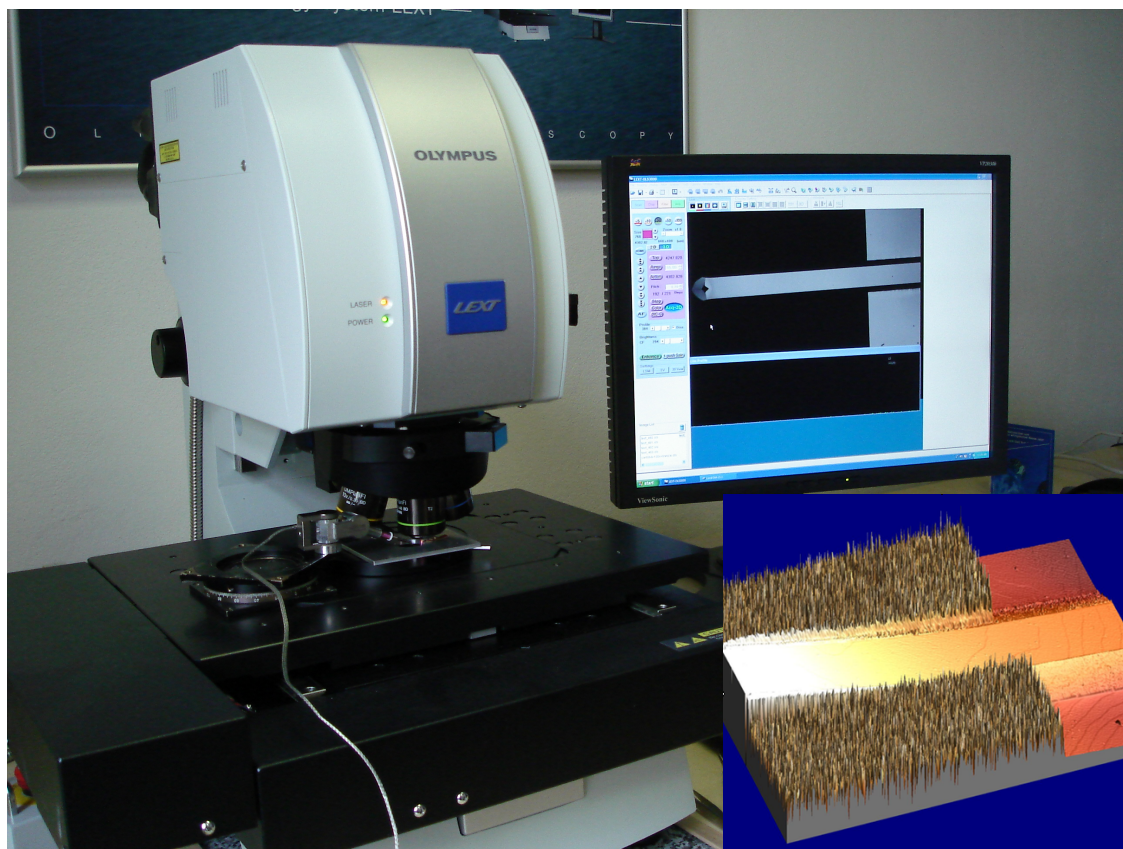


Figure 4.7: View of confocal optical microscope Olympus LEXT with experimental setup for stress studying installed on the microscope stage. Inset shows acquired 3-D image of bent cantilever processed by WSxM software package

TUNA module, which allows current detection as low as tens of fA (C-AFM, Fig. 4.8b). All AFM results reported below were performed in contact mode using the coated cantilevers (BudgetSensors ContE) with resonant frequency about 13 kHz and force constant $0.2 N/m$. Mostly we used fresh cantilevers to avoid artifacts due to the conductive layer abrasion. Local current flowing through the grounded cantilever was induced by a dc voltage bias applied to the bottom contact or to the conductive substrates.

Measurements in UHV were done at pressures about 10^{-10} mbar at room temperatures about $25\text{ }^{\circ}C$ on in-situ deposited samples (which were never exposed to open air, transfer pressure $p < 10^{-7} Pa$). This setup allowed us to apply sample biases in the range from $-10V$ to $+10V$ during C-AFM and I-V characteristic measurements.

During C-AFM in ambient atmosphere all C-AFM measurements were performed at $25\text{ }^{\circ}C$ and approx. 30 % humidity. The possible range of applied bias in Veeco system is from $-10V$ to $+10V$, but external applied higher voltages are also possible.

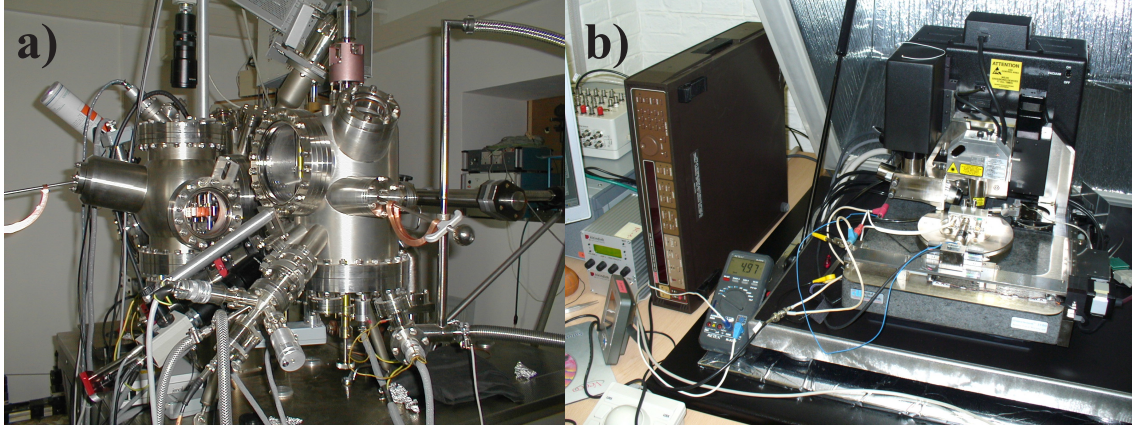


Figure 4.8: View of: a) the UHV apparatus, which includes AFM and STM microscopes connected to the in-house built PECVD deposition chamber; b) Ambient C-AFM microscope Veeco Dimension DI3100 IV

All C-AFM maps of local current were measured with minimal possible (for sufficient signal/noise ratio) negative sample bias. The applied normal force in contact mode was around 25 nN, and scanning speed was kept constant, mostly at 500 nm/s. These settings were chosen to avoid possible artifacts of measurements (see section 3.2.2).

To process AFM results we used Nanoscope 6.13 software, WSxM 4 [57], and Gwyddion [<http://gwyddion.net/>].

Chapter 5

RAMAN MICRO-SPECTROSCOPY OF $\mu\text{C-Si:H}$

5.1 Application of Raman spectroscopy to $\mu\text{c-Si:H}$

5.1.1 Spectra of crystalline Si, a-Si:H, and $\mu\text{c-Si:H}$

Silicon is a very suitable object for study by Raman spectroscopy. Crystalline Si has very intensive and sharp peak at 520.5 cm^{-1} (see fig. 5.1), which is often used for calibration purposes. In case of $\mu\text{c-Si:H}$ it is possible to distinguish amorphous (wide band near 480 cm^{-1}) and crystalline (band near 520.5 cm^{-1}) parts of the Raman spectra. This is commonly used to determine crystallinity of the samples in most laboratories.

5.1.2 Dependence on the excitation wavelength

It is necessary to note that there are two important factors which can cause an error in crystallinity calculations. Firstly, there is a difference in light absorption by amorphous and crystalline phases (See for example fig. 5.2 [58] for excitation wavelength of 514.5 nm). Secondly, the Raman collection depth of silicon can be estimated from the equation [59]:

$$d_p = \frac{1}{2\alpha} \quad (5.1)$$

where α is absorption coefficient of the material. In case of crystalline silicon the Raman collection depth varies from few tens of nanometers for 325 nm wavelength to several μm for 785 nm [60]. So, we used 785 nm excitation wavelength to equalize

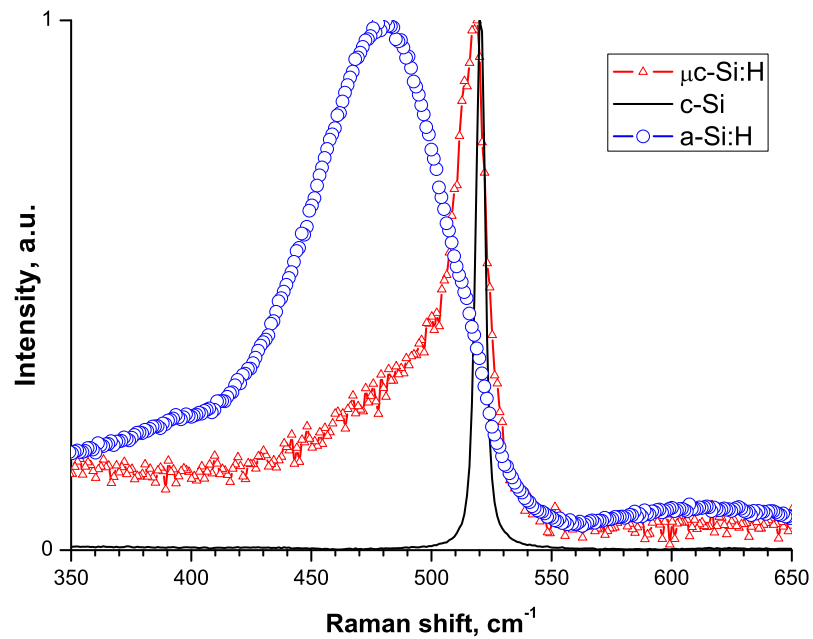


Figure 5.1: Typical Raman spectra of crystalline silicon (black solid line), micro-crystalline film (red with triangles) and amorphous film (blue with circles)

excitation power for both phases of the sample and collect the Raman signal from the whole depth.

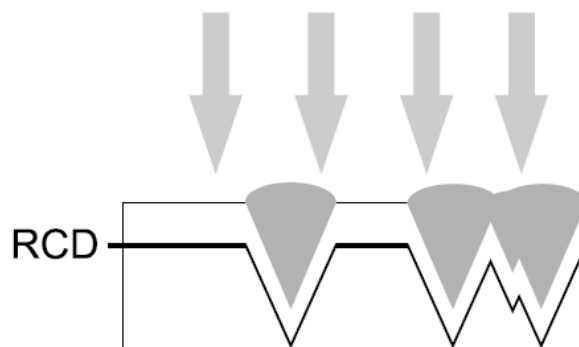


Figure 5.2: Optical model of absorption in mixed phase Si thin film. Black line shows Raman collection depth for this material for excitation wavelength of 514.5 nm

5.1.3 Crystallinity evaluation

For crystallinity calculation from the Raman spectrum of the material it is necessary to separate amorphous and crystalline parts of the signal (see fig. 5.3), then calculate areas under the bands which are proportional to the phase volumes [61].

First of all, the signal background (noise of a detector and luminescence of the substrate) must be removed. The background can be approximated as the polynomial of the 2^{nd} order [62]. The way how to separate two components (amorphous and microcrystalline) of the Raman spectrum is described in [63].

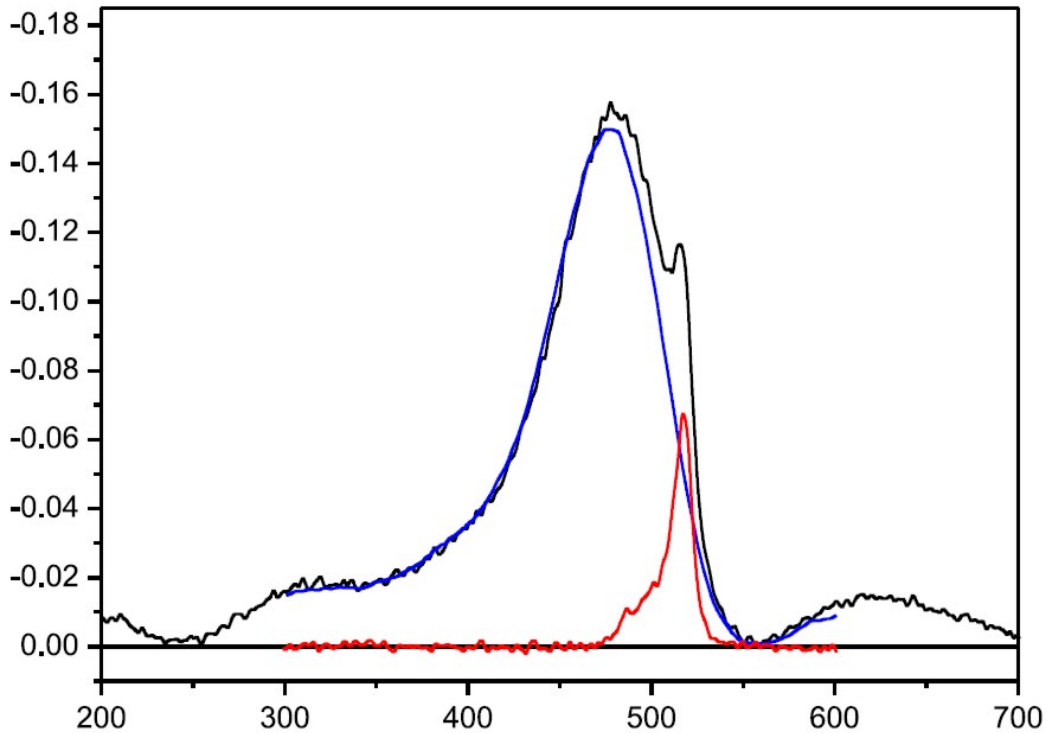


Figure 5.3: *Decomposition of the Raman spectrum of mixed phase Si thin film into components corresponding to two phases: micro-crystalline (red, at 521 cm^{-1}) and amorphous (blue, at 480 cm^{-1})*

We have evaluated the crystallinity as ratio [61]:

$$X_C = \frac{I_C}{I_C + yI_A}, y = \frac{\Sigma_C}{\Sigma_A} \quad (5.2)$$

where I_C and I_A are integral Raman signals (area under spectral band) of crystalline and amorphous phases respectively; Σ_C and Σ_A are integrated Raman cross-sections for crystalline and amorphous silicon.

To estimate ratio of integrated Raman cross-sections y it is necessary to determine crystallinity of a $\mu\text{C-Si:H}$ sample independently. This can be done by AFM topography

measurement of mixed phase sample. If we assume that the crystalline grains are conical and separated from each other (the nucleation density is low enough so that the grains do not constrain each other), bulk (X_C) and surface (X_{AFM}) crystallinities are proportional. Proportionality factor is in good approximation equal to 3 (cone to cylinder volume ratio). This approach ignores presence of the incubation layer and the contribution of spherical grain caps rising above the flat amorphous layer. However, the influence of these two factors on the bulk crystallinity is small and opposite, i.e., they partly compensate. From this consideration and Eq. 5.2 we can get a formula for y :

$$y = \frac{I_C - \frac{I_C X_{AFM}}{3}}{\frac{I_A X_{AFM}}{3}} \quad (5.3)$$

After evaluation of the y for current material and excitation wavelength, the constant can be used for estimation of $\mu\text{c-Si:H}$ samples crystallinity by Raman microscopy (with the same excitation wavelength) using Eq. 5.2.

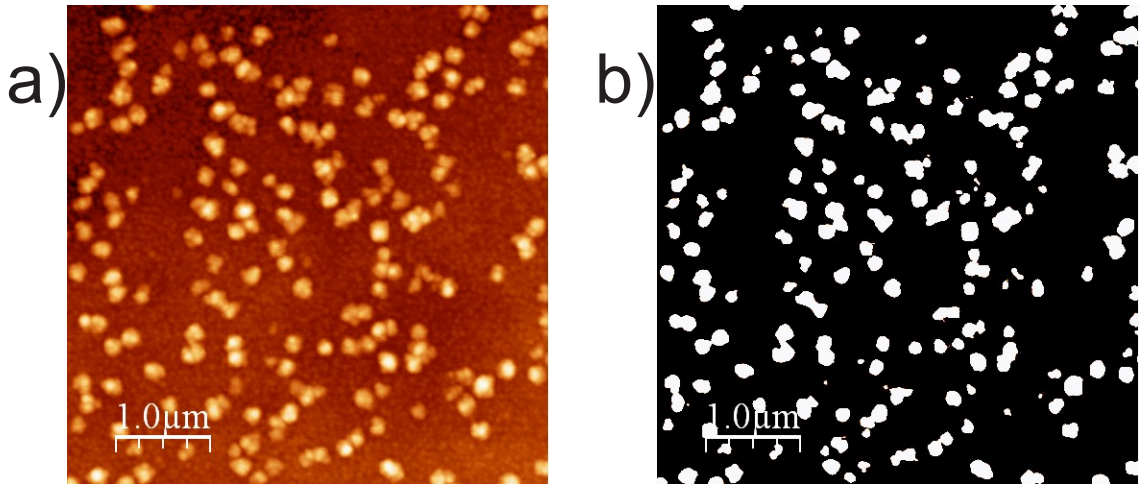


Figure 5.4: View of topography of $\mu\text{c-Si:H}$ measured by AFM. (a) - Microcrystalline grains as spherical "caps" on the sample surface. If one makes cross-section very near the height of the amorphous phase - (b) separation of areas of microcrystalline and amorphous phases

5.1.4 Raman mapping with high resolution

Here we discuss spatial resolution of the Raman spectroscopy for microcrystalline silicon mixed phase films. Is it possible to measure the Raman spectrum from a single grain (or even from a part of a single grain)?

One of the approaches how to overcome the optical resolution limit is to make a source of the Raman signal smaller than optical resolution of the microscope. This approach is used in TERS technique (see section 3.1.2). Another possibility to register structures smaller than the limit is the low concentration of the observed medium (in case of $\mu\text{C-Si:H}$ thin films - spatially separated grains). It may be possible to detect existence and characterize grains even smaller than the optical resolution limit. In figure 5.5 an example of the Raman mapping on the sample with mixed structure is shown, where grains are separated from each other.

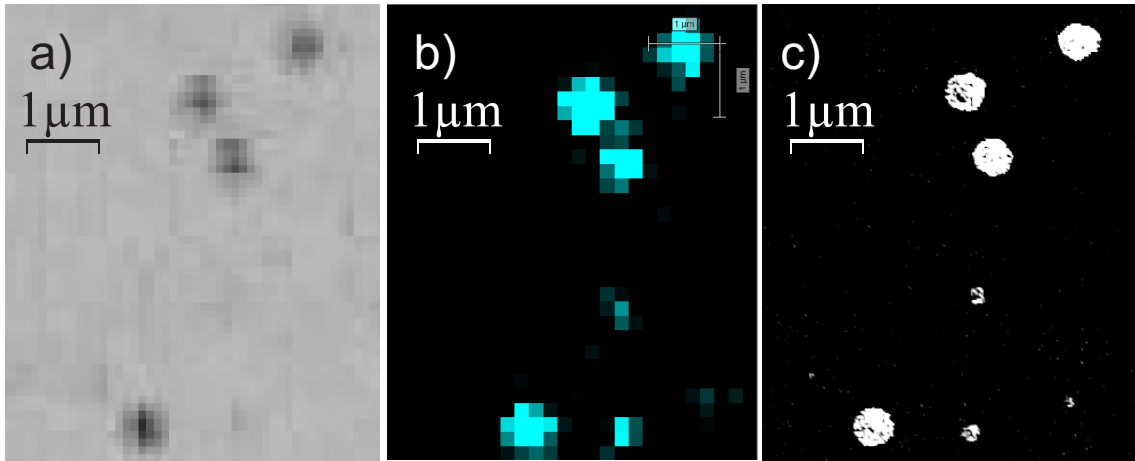


Figure 5.5: a) The optical microscope image of $\mu\text{C-Si:H}$ thin film with low density of microcrystalline grains; b) Raman map of the same place measured at excitation wavelength of 442 nm ; c) map of local currents measured by C-AFM at the same place

Figure 5.5a shows optical view of the sample imaged by 100x objective. In the image one can clearly recognize four dark objects (microcrystalline grains). Raman map in fig. 5.5b was measured with the 442 nm excitation wavelength and reflects the local crystalline volume fraction. The Raman map confirms that all four visible objects in the optical image are microcrystalline grains. In addition, it reveals the presence of three more microcrystalline grains in the bottom right part of the image which are not visible by the optical microscope. To verify the presence of these three small grains we have used the C-AFM. This technique allowed us to measure not only topography of the sample, but also had shown the conductivity of small structures. From comparison with the map of local current in figure 5.5c we can conclude that these three objects have microcrystalline structure. The size of larger grains estimated from C-AFM is slightly below 500 nm and diameters of small grains are around 200 nm , therefore they are not distinguishable by optical microscope thanks to the fundamental limit

of optical resolution (see Eq. 3.1). The smallest grain detected by Raman mapping had 160 nm in diameter.

To compare the resolution of Raman maps done with excitation wavelengths of 785 nm and 442 nm we used mixed phase sample deposited onto glass substrate (to avoid signal from the bulk Si in case of silicon substrate). Both maps are shown for the same place of the sample in fig. 5.6 in part b) for 785 nm and in c) for 442 nm excitations. AFM image of the same area in part a) shows that there is one large grain in the central part (approx. 2 μm in diameter) and few smaller grains with diameters from 200 to 800 nm around. The large grain is clearly visible in both Raman maps.

The limitations of optical microscopy (even in confocal mode) allow minimal laser spot sizes of 2 μm for 785 nm and 1 μm for 442 nm in diameter respectively. Of course, this has an impact on the resolution of Raman maps. But this is not the only reason for the difference in resolution of both maps.

Although the collection times and excitation intensities were the same for both excitation lasers, the spectrum excited by 785 nm is weaker with relatively higher amorphous component centered at 480 cm^{-1} . The sensitivity of 785 nm Raman spectra to amorphous phase is given by Raman collection depth (see equation 5.1), which is much larger than the thickness of the layer. Consequently the amorphous tissue below the conical microcrystalline grain contributes to the Raman spectra. On the contrary, small grains in the Raman map measured by 442 nm laser have almost the same maximal intensity as the large grain in the center. This high sensitivity is given by strong absorption of the 442 nm wavelength in the silicon thin film - Raman collection depth is around 50 nm . Therefore the conical shape of the grains does not play any role.

Line profiles of the AFM topography image and of the 442 nm Raman map along the white line drawn in the fig. 5.6 a) are shown in the same figure in d). The AFM topography cross-section shows two large grains separated by 350 nm wide gap of amorphous silicon. Raman integral intensity profile also indicates two individual grains. The ratio between the maximum Raman intensity at the smaller grain and at the minimum in the amorphous gap reaches to 65 %, which fulfills the Rayleigh definition of two resolvable objects. Therefore the resolution of Raman mapping with excitation by 442 nm laser is 350 nm . This value is close to the optical resolution limit given by Eq. 3.1 $R = 300\text{nm}$. If we measure large grain diameter from Raman mapping (defined as a full width in half maximum FWHM) we get the same value as from AFM measurement (1.65 and 1.64 μm respectively). This is somewhat unexpected as we would expect the limited optical resolution to enlarge the grains. The explanation is

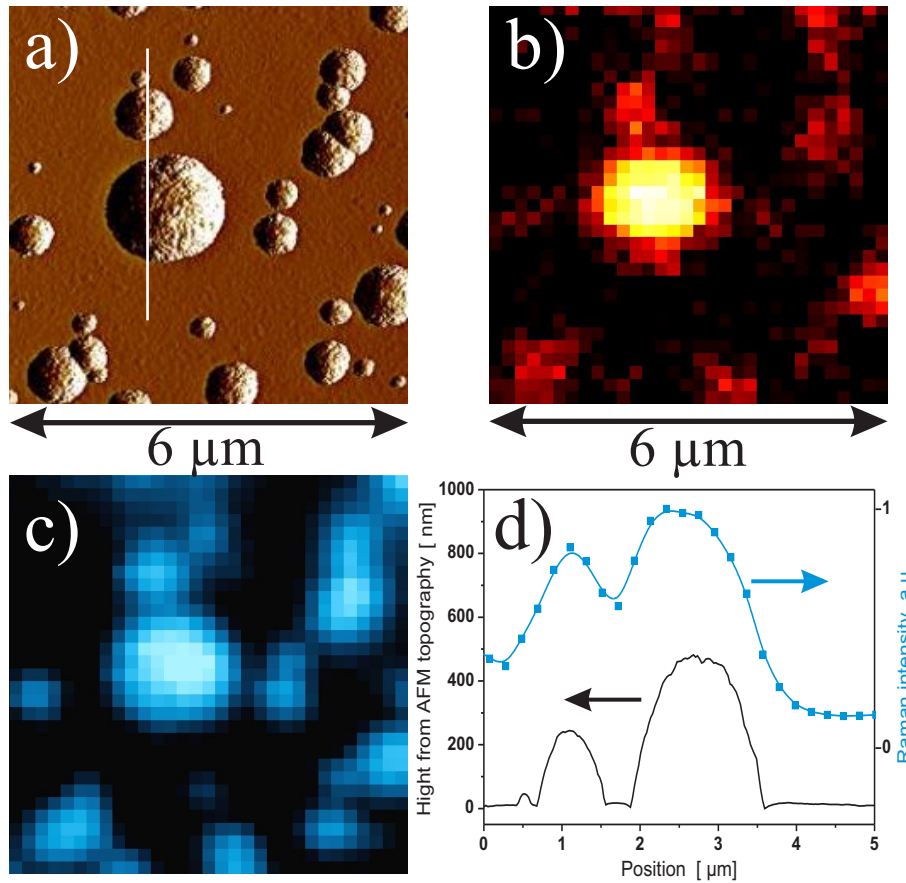


Figure 5.6: Comparison of the Raman mapping measurements at 442 nm and 785 nm: a) AFM image of the mapped area; b) Raman map measured with 785 nm excitation wavelength; c) Raman map measured with 442 nm excitation wavelength; d) Line profiles of the AFM topography image (black line, left arrow) and Raman map measured with 442 nm (blue squares, right arrow) along the white line in a); blue line is only guide for an eye

as follows: the integral intensity of microcrystalline silicon Raman spectra is in first approximation directly proportional to the area of grain illuminated by laser beam. If the laser beam is centered just on the boundary between grain and amorphous tissue, half of the beam is shining on the grain and therefore the integral Raman intensity is half of the maximum value measured at the center of the grain.

The Raman mapping proved that in case of a sample with strong Raman signal it is possible to characterize sample features smaller than the optical resolution limit.

5.2 Stress investigation and elastic properties of $\mu\text{C-Si:H}$

In this section it will be shown that micro-Raman spectroscopy is a unique technique for the measurement of local stress in thin films of $\mu\text{C-Si:H}$. Mechanical stress is an important reliability issue in various devices based on thin silicon films. Many problems of defective micro electro mechanical devices (MEMS) and solar cells (film adhesion, contacts, etc.) can be traced back to defects generated by stresses which exceeded a certain critical value during the processing.

5.2.1 Position of Raman peak

There are two basic effects contributing to the shift of crystalline silicon peak from the expected value of 520.5 cm^{-1} . The first one is the intrinsic stress of the material (residual or induced). If the peak is shifted to higher numbers then stress is *compressive* (negative value of σ) otherwise stress is *tensile* (positive value of σ) [64]. The relation between strain or stress in silicon and the Raman frequency is rather complex [60]. In some cases, however, the relation becomes simply linear:

$$\sigma[\text{GPa}] = -C(\omega - \omega_0)[\text{cm}^{-1}] \quad (5.4)$$

where:

- σ - total stress in the film
- C - constant which depends on the internal structure of the sample
- ω - position of the crystalline peak
- ω_0 - position of crystalline peak for stress-free sample (520.5 cm^{-1})

The second contribution to peak shift (crystalline and amorphous as well) is caused by the phonon confinement effect in the small nanometer-scale crystallites present in the material [65]. Paillard et al. [66] have shown that the size of silicon nanocrystals smaller than 6 nm shifts crystalline peak position by more than 1 cm^{-1} . The size of crystallites larger than 10 nm has a minor impact on the shift of the peak.

Again, one has to keep in mind that long excitation wavelength leads to collecting of Raman signal from the depth (see equation 5.1) of the sample. In this case Raman spectrum indicates "average" stress in the whole volume. On the contrary, using of

short excitation wavelength leads to stress measurement from thin layer very near the sample surface.

5.2.2 Stress creation

For studying stress in microcrystalline silicon we deposited thin films onto PET substrates and used a special four point holder (see fig. 5.7a) which allowed us to bend our samples for varying induced stress in the material. Unfortunately, this setup didn't work for us, because it wasn't clear what is softer: PET or $\mu\text{C-Si:H}$ film deposited on it? Did the substrate break first or the film (see AFM image on 5.7b)? The maximum curvature in this case was about 5 mm in diameter.

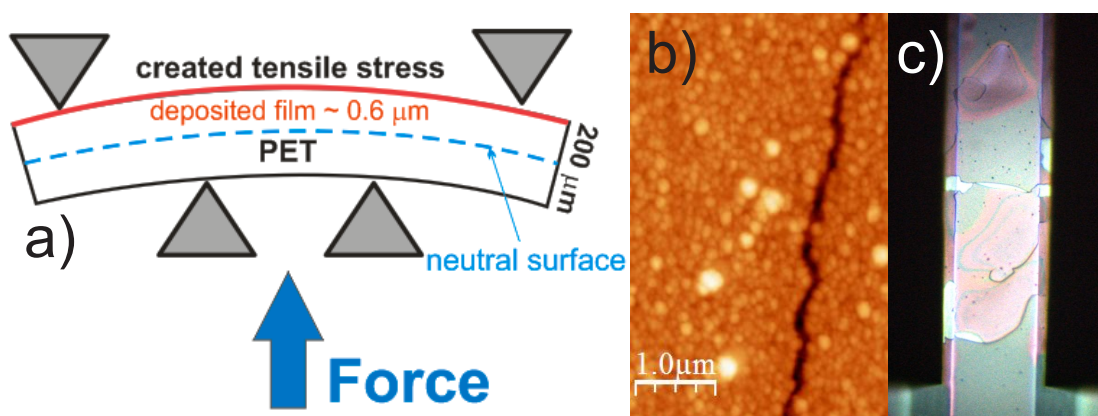


Figure 5.7: a) Schematic view of a sample of $\mu\text{c-Si:H}$ deposited onto PET substrate in the holder for stress creation. Blue dashed line shows the neutral (unstressed) plane inside the sample during bending; b) AFM image of the cracked sample; c) Optical image of broken film deposited onto a cantilever after applying high compressive stress

To resolve this problem, we decided to use AFM-cantilevers as a substrate for the film. Standard AFM-cantilever consists of thick wafer and cantilever itself. It is manufactured from highly doped, single crystal silicon (see details in section 4). Because of the perfect elastic properties of the cantilever we can bend our film to curvatures less than 1 mm in diameter. In this case the film broke first (see fig. 5.7c).

To leave the possibility of using long excitation wavelengths we used cantilevers with a metal coating, because the metals don't contribute to Raman signal and screen the signal from the bulk silicon of the cantilever.

5.2.3 Growth stress estimation. Stoney formula

After deposition the cantilever had initial bending (see fig. 4.4b), which provided us with information about the growth stress. Initial stress in the sample which is deposited onto flexible surface can be estimated using Stoney formula [43]:

$$\sigma = \frac{Y d_{sub}^2}{6d_t R} \quad (5.5)$$

where:

- σ - growth stress in the film
- Y - biaxial elastic modulus of the substrate
- d_{sub} - substrate thickness
- d_t - total film thickness
- R - radius of curvature

This formula can be used in case that the stiffness of the substrate is much higher than that of the deposited film, so bending of the substrate doesn't significantly reduce initial stress in the film. For this reason we deposited very thin film of $\mu\text{C-Si:H}$ (200 nm thick) onto the 2 μm thick cantilever. By using calculated elastic constant for the substrate (silicon $\langle 100 \rangle$) from [67] we estimated the growth stress of the microcrystalline film as 180 MPa.

It has to be noted, that during the deposition $\mu\text{C-Si:H}$ film grows on both sides of the cantilever. However, our measurements by Raman spectroscopy have shown, that the Raman signal from the film on the face (nearest surface to plasma discharge) side of the cantilever is more than 10 times stronger than Raman signal of the film from the other side. It means that thicknesses of the films on opposite sides differ more than ten times. So we neglect the influence of the backside film.

With our setup (see fig. 4.6) one can use another useful feature. It is possible to scan the exciting laser along the cantilever and probe by Raman spectroscopy the stress evolution in the film from the chip base (growth stress) to the partially relaxed state in the film on the cantilever. This is suitable for the films with comparable thickness with cantilever, when intrinsic stress of the film is high enough to bend the cantilever.

5.2.4 Profiling of bent cantilevers by confocal microscopy and curvature calculation

After the deposition the profile of the cantilever bent by the growth stress was extracted from 3-D image acquired by confocal microscope (see fig. 5.8a). Figure 5.8b shows a part (from $-10 \mu\text{m}$ to $200 \mu\text{m}$ in X coordinates) of the polynomial fit of the whole profile. We defined the origin of X-coordinates is on the face surface at the border where the solid silicon base ends and flexible cantilevers starts.

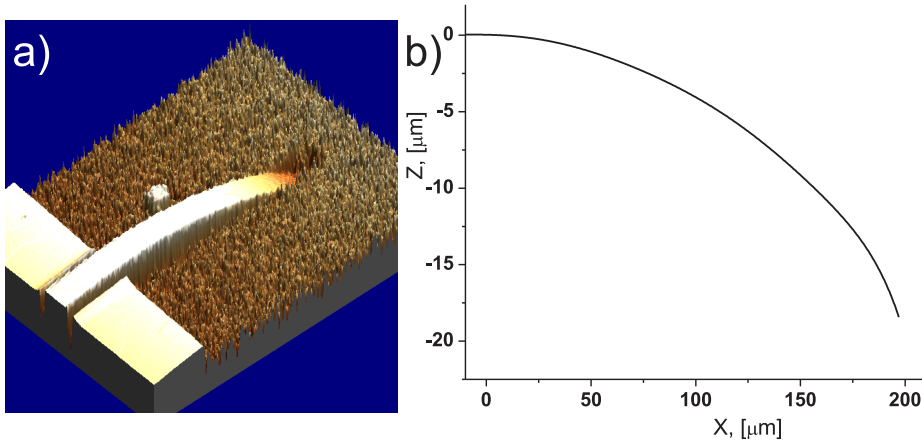


Figure 5.8: a) 3-D view of bent cantilever with deposited $\mu\text{c-Si:H}$ film showing the presence of growth stress; b) Polynomial fit of the profile of the cantilever which allows to estimate the curvature of the bent cantilever

The fitting procedure is necessary because the real measurement is influenced by a noise, which is amplified by differentiating needed for obtaining the curvature. After the fitting the curvature in each point of the profile can be easily calculated by the formula 5.6.

$$k = \frac{z''}{(1 + z'^2)^{3/2}} \quad (5.6)$$

During the bending we registered the Z-position of the end of cantilever. This parameter defines the bending state. Because of the low depth of focus of high magnification objective the position can be measured rather precisely. Fig. 5.9 shows an example of calculated local curvatures from the fitted profiles along the cantilever in different bent states. Again, the point $X = 0$ is the border between solid base and flexible cantilever of the AFM-chip.

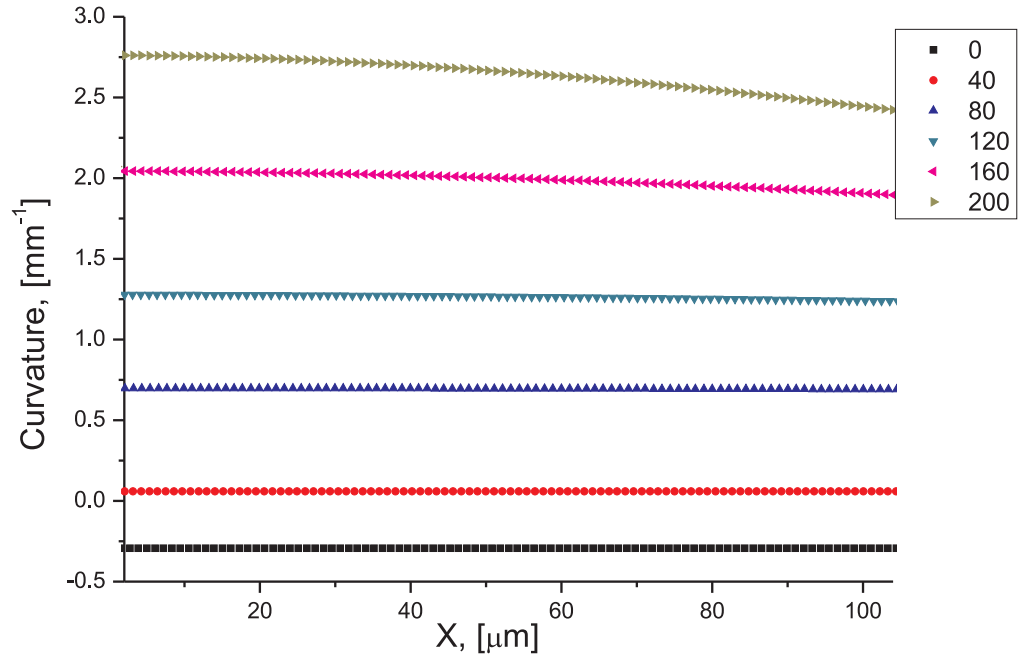


Figure 5.9: *Calculated curvatures of the bent cantilever in different bending states (Z-position of the end of cantilever). At small deviations from the initial state, the local curvature is the same along the cantilever. At curvatures with radius less than 1 mm near the base the profile of the cantilever becomes more parabolic.*

Fig. 5.9 shows that at high curvatures the profile of the bent cantilever becomes more parabolic. Therefore, the place of the maximum stress is the border between the base and flexible part of the cantilever. After a series of experiments with Raman mapping of bent cantilevers we found that the mostly stressed part of the film is at $X \approx 10 \mu\text{m}$ from the border. The reason of this small shift is the possibility for the film at the border to relax the induced stress at the expense of unstressed film on the solid cantilever base.

From geometrical reasons the calculated curvature is directly proportional to the shortening (elongation) of the film, i.e. to the stress induced in the film. The stress σ can be calculated as:

$$\sigma = \frac{Ed}{R} \quad (5.7)$$

where E - is Young modulus of the deposited film, R - the radius of curvature of the bent cantilever, and d - the distance of the film from the neutral plane (see fig. 4.5).

Therefore, the induced stress is proportional to the curvature of the bent cantilever.

5.2.5 Raman spectroscopy of the stressed $\mu\text{C-Si:H}$ thin films

After bending a cantilever with deposited $\mu\text{C-Si:H}$ thin film we measured Raman map along the cantilever and watched for the changes in microcrystalline peak or amorphous band position with induced stress. The dependence follows the expected shift to higher wavenumbers linearly with increase of the stress.

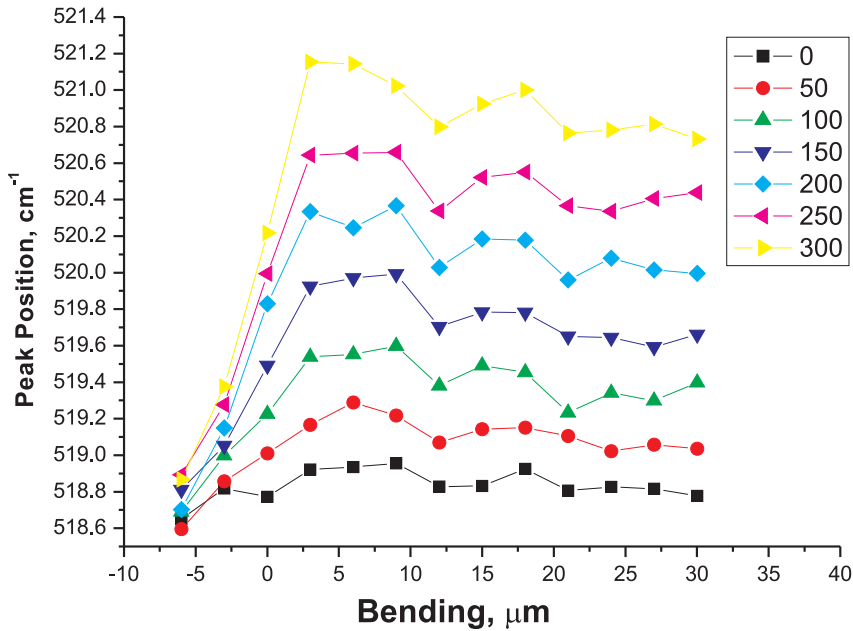


Figure 5.10: Maps of TO-LO phonon peak position along the bent cantilever near the border with solid base ($X = 0$) at different bent states. All points were calculated automatically by WIRE 2.0 (Renishaw software) - spectra were fitted by mixed Lorentzian and Gaussian peaks

Microcrystalline silicon Example of fully microcrystalline 300 nm thick film is presented on fig. 5.10. It shows measured Raman maps of the microcrystalline peak position near the border between solid base and flexible cantilever. States with bendings from initial to almost maximum possible (then silicon cantilever breaks) are measured.

Raman microcrystalline peak positions can be compared with measured curvatures for different bending states from fig. 5.9. Points in the graph 5.10 were calculated

automatically by WIRE 2.0 (Renishaw software) by fitting maps spectra by mixed (superposition of Gaussian and Lorentzian peaks) peak, where each component can have arbitrary weight. The reason of using of the mixed peak for fitting appears from the fact, that microcrystalline peak is not symmetrical while Gaussian and Lorentzian peaks separately are both symmetrical. So such combination of both peaks allows fitting the real spectrum more closely. On the other hand, such approach adds uncertainty into the fitting process.

For the purpose of making the fitting procedure more accurate we made two separate fittings: Gaussian and Lorentzian. Again the fitting procedure was done in WIRE 2.0 (Renishaw software). Fig. 5.11 shows resulting fits of microcrystalline silicon film of 300 nm thick.

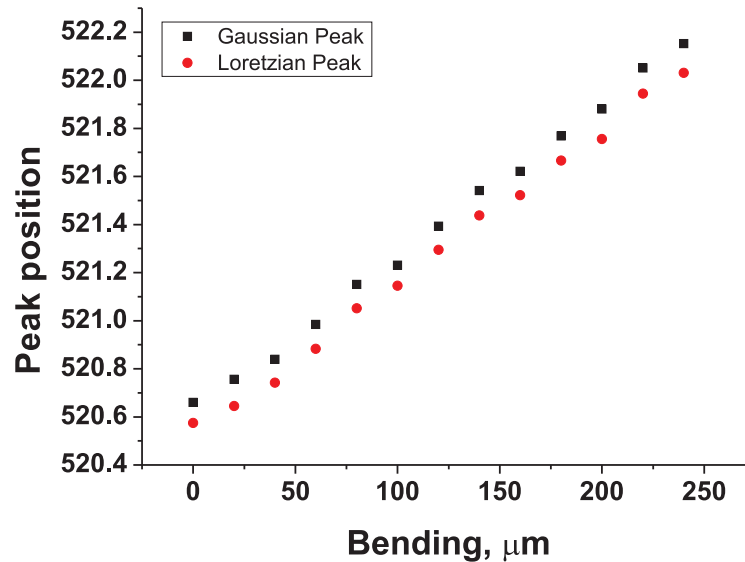


Figure 5.11: Positions of microcrystalline Raman peaks fitted by Gaussian and Lorentzian peaks at point on the cantilever with $X = 10\mu\text{m}$ from the border

The TO-LO phonon peak position fitted by Lorentzian and Gaussian peaks are shifted relative to each other because of non-symmetrical nature of the microcrystalline silicon peak. At the same time in case of using only Lorentzian (or only Gaussian) peak the fitting error is systematic and relationship between calculated positions of the Raman peak and stress is close to linear, as it is expected from Eq. 5.4.

Amorphous silicon In case of amorphous silicon band near 480 cm^{-1} , the fitting procedure by Gaussian or Lorentzian peaks is not precise enough to resolve automat-

ically 1 cm^{-1} position shift of approx. 60 cm^{-1} wide amorphous band due to applied stress. The fitting error is about several cm^{-1} .

To study the reaction of the amorphous silicon on the induced stress we used Factor Analysis (FA) [68]. This method is not based on fitting procedure, but on comparing of consecutive spectra to each other. Therefore, the method is very sensitive to changes in spectra of the same material under different stress conditions. Fig. 5.12 shows calculated positions of the amorphous band during the bending of the cantilever which were processed by FA method. The thickness of the mixed phase film was approx. 300 nm .

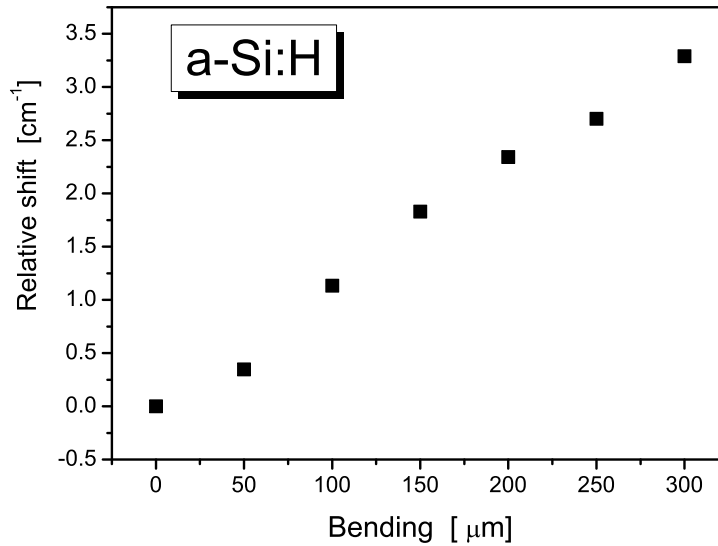


Figure 5.12: Positions of amorphous Raman peaks calculated by using Factor Analysis under different stress conditions.

Again, as it was in the case of microcrystalline peak (near 520.5 cm^{-1}) we have clear linear dependence of the Raman peak position on the applied compressive stress. Comparison of the graphs 5.11 and 5.12 shows, that the amorphous band has a little bit larger shift under the stress than microcrystalline peak.

To roughly estimate the maximum value of the applied stress, one can use equation 5.4 and $C = 250\text{ MPa/cm}^{-1}$ for microcrystalline silicon, which was reported by Anastassakis [69]. However, this is the only one reported value for the microcrystalline silicon and we didn't find any reported value for a-Si:H materials. Therefore, our next goal is to develop our current setup and measure the value of the constant for our samples.

Chapter 6

C-AFM OF μ C-Si:H. LOCAL ELECTRICAL PROPERTIES

6.1 Charge transport in μ c-Si:H

As described in the chapter 2, the hydrogenated microcrystalline silicon has a complicated micro-structure consisting of columnar grains surrounded by disordered tissue and/or amorphous phase. The variability of structure and resulting electronic transport properties has led to a controversy over the dominant charge transport mechanism and, in particular, over the location of the dominant transport route [70]. The capability of C-AFM to measure local currents with nanometer resolution offers a chance to look for the transport route directly by identifying more conductive parts of the μ c-Si:H samples [71, 72].

In this chapter, we mainly discuss electrical conductivity and C-AFM results. Details of sample preparation procedures are given in chapter 4. Results presented here have been measured both with a coplanar geometry (in which the transport parallel to the substrate is measured) as well as with a vertical geometry (in which the transport perpendicular to the substrate is measured).

6.1.1 Model of charge transport in μ c-Si:H

Before the discussion of C-AFM results our model of the charge transport will be considered. First of all, let's summarize widely accepted elements of the model. μ c-Si:H is composed of two phases:

- the small nanocrystals (10 - 30 *nm*)
- the large grains (100 - 1000 *nm*), formed from the small nanocrystals

- the small nanocrystals are connected by twin boundaries and stacking faults
- size of the small nanocrystals is not sufficient for the formation of the space-charge regions and potential barriers which could block the charge transport
- small grain boundaries form the localized tail states

Now we introduce the elements of our model of the charge transport. It is based on the existence of a third phase - the large grain boundaries (LGBs):

- represent a new form of tissue, into which hydrogen, probably oxygen and defects concentrate
- the increased content of hydrogen and oxygen increases the mobility band gap and the potential barriers are formed, blocking the transport at the conduction band edge
- the concentration of the defects does not increase the conductivity of LGBs

6.1.2 Macroscopic measurements of the μ c-Si:H resistance

For the macroscopic measurements of the conductivity of μ c-Si:H thin films we used the coplanar geometry of contacts. For this purpose we deposited gold contacts onto the sample of microcrystalline silicon thin film deposited onto non-conductive glass substrate as it is shown in the fig. 6.1. When a tenths of mm wide metal contacts are separated by a gap of about $1\ mm$ and applied to about $1\ \mu m$ or thinner silicon layer, the contact resistance can be neglected and the true conductivity is evaluated. For photovoltaic solar cells, the charge transport perpendicular to the substrate is important. However, in the corresponding sandwich geometry, the contact resistance cannot be neglected as in the dc measurements. As we have shown [73], a possible solution is to use the AC conductivity, for which the influence of the contacts is excluded at sufficiently high frequencies and the true perpendicular conductivity can be evaluated. However, the AC bias may enhance the LAO process [74] (it will be considered in Section 6.3.2).

We used two different samples A and B, which were grown at the same deposition conditions, but sample A was $300\ nm$ thick while the sample B was two times thicker ($600\ nm$). The surface crystallinity of the sample A was about 50 %, and in case of the sample B about 42 %.

We sequentially connected the gold contacts (stripes) varying the distance between anode and cathode and measured $I-V$ characteristics of the sample. Example of such

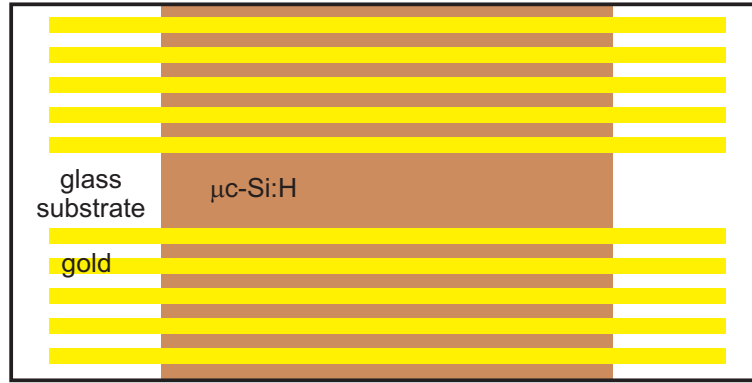


Figure 6.1: Sample for macroscopic conductivity measurement of the $\mu\text{C-Si:H}$ with coplanar geometry. Gold contacts in the form of stripes were deposited onto the standard sample

$I - V$ characteristic measured on the sample A is shown in fig. 6.2a for the distance between contacts of 0.6 mm . The measurement of the $I - V$ curve was started at zero voltage, then the voltage was increased up to 1.5 V , then the voltage was decreased down to -1.5 V , and finally it was increased up to the initial point - zero voltage. We used three different speeds of the voltage ramp: 50 mV/s , 150 mV/s and 500 mV/s .

The $I - V$ characteristics of thinner sample A are quite noisy because of the very high resistance of the film (note that currents are tens of pA), but it is clear that the $I - V$ curves are linear (contacting of the sample is Ohmic). Fig. 6.2a shows, that the deviations of individual points from the line at lowest speed of 50 mV/s are minimal, while in case of the highest speed of 500 mV/s one can distinguish measurements when the voltage was increased and vice versa. This difference is a consequence of the fact that the sample has its own electrical capacitance.

After fitting of all measured $I - V$ curves one can calculate electrical resistance for each combination of the sample contacting. Figure 6.2b shows the dependence of the resistance on the effective distance (real distance reduced by the gold stripes widths) between contacts. In result, the calculated volume resistivity ρ of the sample can be found from the equation:

$$\rho = R \frac{S}{l} \quad (6.1)$$

where R is measured resistance, S is cross-section and l is a distance between contacts. For the case of sample A ($S \approx 1.5 \cdot 10^{-9} \text{ m}^2$) the volume resistivity $\rho \approx 50 \text{ k}\Omega \cdot \text{m}$. This value is about 20 times smaller than in case of non-doped crystalline silicon. It has to be noted that this result is calculated for the thin film with the

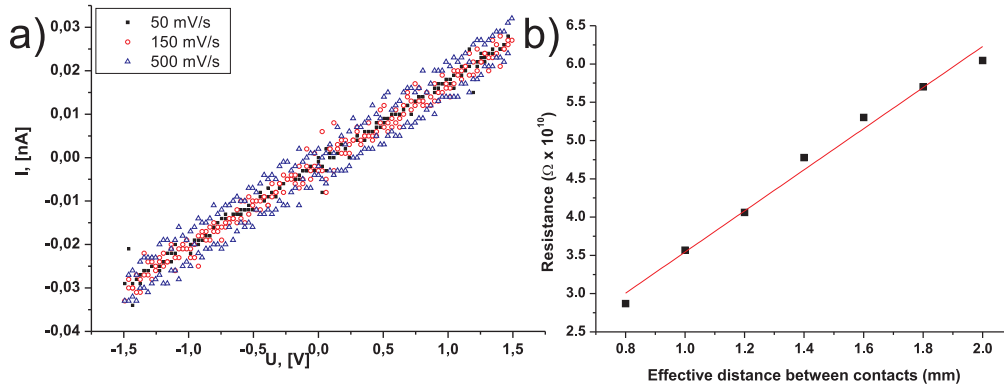


Figure 6.2: a) An example of I - V characteristics of the 300 nm thick μ c-Si:H thin film measured between the same contacts at three different speeds of the voltage changing: black dots - 50 mV/s, red circles - 150 mV/s, and blue triangles - 500 mV/s; b) Dependence of the resistance of the same sample on the effective distance between contacts calculated from I - V characteristics

same crystallinity as of sample A and can be much different for films with another crystallinity.

6.2 Ultra high vacuum C-AFM

Standard macroscopic measurement techniques can give only average values of transport characteristics such as conductivity or diffusion length of the carriers, but say nothing about charge transport between amorphous phase and microcrystalline grains. Various techniques can be used to find additional information about the microstructure and the electronic transport properties. One approach is to modify the macroscopic characterization methods, such as a light beam induced current, to probe the material properties locally with lateral resolution as high as possible [75]. Another possibility is to use inherently microscopic techniques, such as STM or AFM and to combine them with the detection of particular quantities of interest in parallel to standard surface morphologies [76]. These techniques were described in section 3.2. Here we will focus on the C-AFM as one of the main techniques for investigation of the electrical properties at nanoscale. First of all, the measurement of samples made in-situ in UHV conditions will be considered. The main advantage of UHV is the absence of contaminations on the sample surface, which significantly increase signal/noise ratio. In addition, such conditions facilitate the interpretation of measured data.

6.2.1 Charge trapping

It was already mentioned in the Section 3.2.2, that C-AFM measurement itself can change the local electrical properties of the sample. So-called "memory effect" was observed by Rezek et al. [77] during the subsequent scanning of the same area. They used Kelvin probe force microscopy [78] to measure the surface potential offset between scanned and pristine (not previously scanned) areas. The probable explanation of this result can be some kind of charge trapping which occurred in deep electronic states at the sample surface.

The charge trapping also complicates measurements of $I - V$ characteristic of a sample - the current is decreasing with time at the same applied voltage. Therefore, results of the sequence of the $I - V$ characteristics measurement from the same place are different. The first $I - V$ curve shows the highest currents and the last - smallest ones. To have some statistics of such experiments we measured $I - V$ curves at different pristine points of sample surface.

6.2.2 Results for in-situ samples

The typical C-AFM result of our $\mu\text{c-Si:H}$ samples with bottom contact (in this case the film was deposited onto n-doped crystalline silicon substrate) is shown in inset of the fig. 6.3. More conductive microcrystalline grain (bright) is surrounded by amorphous tissue (dark). The image shows, that even though the surface is clean in UHV, the local currents still fluctuate due to dynamic contact of the tip scanning the rough sample surface. Different effective contact area leads to scatter of the $I - V$ curves shown in fig. 6.3. Each curve was measured on a fresh spot to avoid the memory effect due to charge trapping.

We measured twelve $I - V$ curves on microcrystalline silicon (within the same grain) and twelve $I - V$ curves on surrounding amorphous tissue. Groups of these curves can be easily resolved from each other (see fig. 6.3). Amorphous silicon demonstrates noise-level conductivity, while current through microcrystalline silicon reaches hundred of pA at +10V sample bias. Note asymmetrical shape of microcrystalline $I - V$ curves, which wasn't observed in macroscopic measurements (see section 6.1.2). We explain this fact by existence of the Schottky barrier between Pt/Cr coated tip and slightly p-type nature of the microcrystalline grain. As it will be shown in section 6.3 in ambient condition the Schottky barrier is reduced by local charges which are situated in localized electronic states in the layer of native oxide and we do not observe such shape of $I - V$ curve.

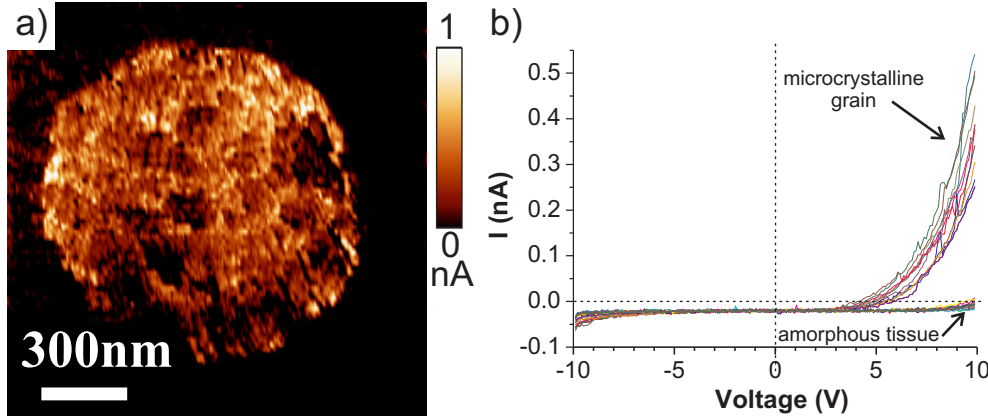


Figure 6.3: I - V characteristics measured at 12 different points of the same grain and at 12 different points of the surrounding amorphous tissue. Inset illustrates UHV C-AFM image of local current measured on the mixed phase μ c-Si:H with sample bias of +10 V

This experiment confirms that microcrystalline grains are much more conductive than the amorphous silicon. $I - V$ characteristics make it clear why one should use positive sample bias for good contrast between amorphous and microcrystalline silicon in UHV C-AFM experiments.

6.3 Ambient C-AFM

Unfortunately, the UHV C-AFM technique has two disadvantages which significantly reduce its wide usage. First of all, it is very expensive in maintenance and secondly, it is time consuming. For example, one needs several hours just for changing a sample or a blunt cantilever. Much more convenient way is using C-AFM in ambient atmosphere.

6.3.1 Main difficulties during ambient C-AFM

Measurements of local currents in ambient conditions are more complicated in comparison with UHV C-AFM. A surface is not so clear as in case of the vacuum, so measured currents are much lower. Fortunately, modern technologies of AFM production are advanced enough to enable ambient C-AFM microscopes with high sensitivity to measure currents as low as tens of fA. Let's consider main obstacles during ambient C-AFM in detail and how they are addressed.

Native oxide After removing a sample from the deposition chamber, it will be covered by a thin film of native oxide in few hours [79]. After several weeks the thickness of the native oxide stabilizes (for the c-Si the thickness of the native oxide is about 0.7 nm , which is a result of the growth limited by diffusion length). The electrical resistance of the SiO_2 is several orders higher than microcrystalline silicon which, in combination with a tiny contact area between AFM-tip and a sample surface, significantly reduces local currents. We also don't know if the native oxide thickness is the same for microcrystalline and amorphous parts, which adds some uncertainty into an interpretation of the measured data. In this work we suppose, that the thickness of the native oxide is the same for both amorphous and microcrystalline phases. Moreover, sample surface is also covered by various contaminants.

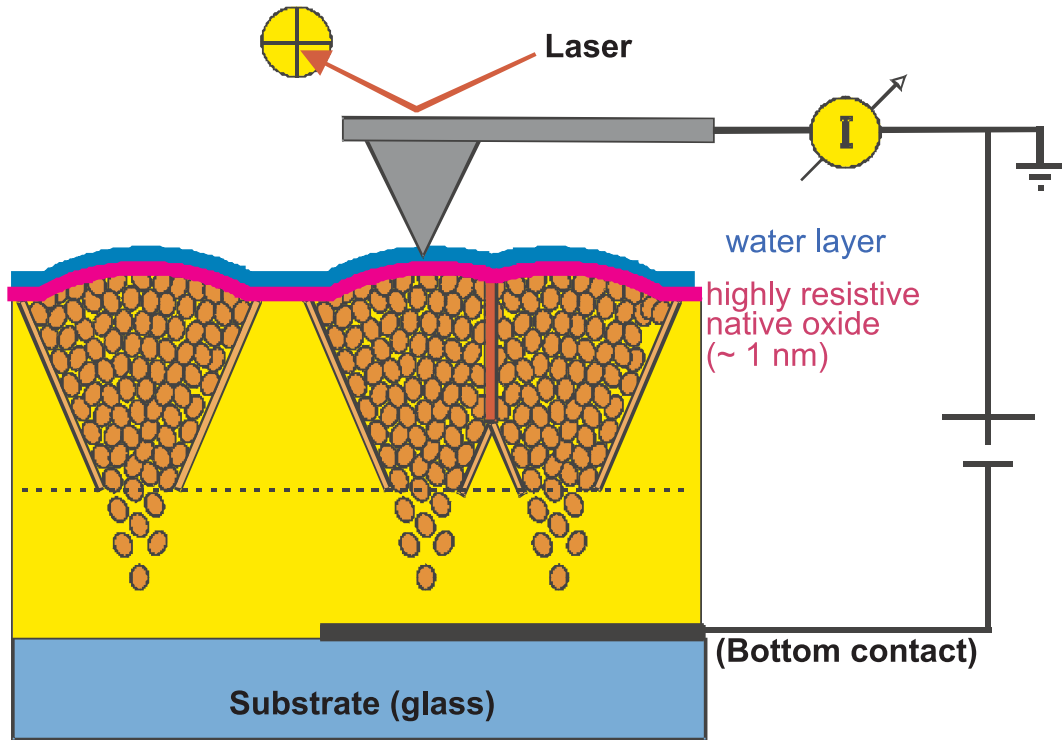


Figure 6.4: Scheme of the ambient C-AFM setup. Layer of native oxide as well as layer of condensed water are always present on the surface of $\mu\text{c-Si:H}$ sample

Layer of condensed water Next substantial problem of the ambient C-AFM is the layer of the condensed water on sample surface which is always present due to the non-zero humidity of air. In contact mode C-AFM (see fig. 6.4) the water meniscus is formed. The applied electric field creates oxyanions from water molecules and, in case of positive sample bias, transports them through native oxide. This leads to the known effect - local anodic oxidation (LAO) of the sample surface [55], which is

used in AFM-based nanolithography. The effect is widely studied and several models exist [55, 79, 80, 81, 82, 83].

”Memory effect” - Local anodic oxidation and charge trapping Now we consider two main constituents of the so-called ”memory effect”: LAO and charge trapping which take place for the crystalline silicon. Fig. 6.5 demonstrates the process of LAO on silicon surface in detail.

To enhance the process of oxidation, surfaces with native oxide are used [81]. Samples are prepared in the followed way. In the beginning the Si surface is etched by *HF* acid, resulting in a clean *H* or *HF* terminated surface. With time fluorine is replaced by *OH* from the water vapor. *H* is slowly replaced by *OH* and water begins to polarize/attack silicon back bonds. Then *OH* groups begin to form surface oxide layer. Native oxide grows by Mott-Cabrera mechanism [84].

Silicon surface LAO is observed when a positive bias is applied on the hydrogenated surface with respect to the SPM tip which is grounded. The electric field drives the migration of the oxyanions (from the water layer) through the surface oxide to the *Si* – *SiO₂* interface, resulting in surface oxide growth.

The height and width characteristics of the induced oxide line depend on the applied bias value, which evidences that the oxidation mechanism is linked to the tip-surface electric field. An electric field of $10^9 \text{ V} \cdot \text{m}^{-1}$ is commonly cited as the threshold value to produce oxidation. For the crystalline silicon and standard AFM-tip the threshold sample bias voltage is approx. 5 V [55].

In addition to the oxide growth a charged layer exists at the *Si/SiO₂* interface [85] due to the interface traps. The trapped charge is screening applied voltage which leads to decrease of the local currents. Gordon et al. [81] showed that trapped charge as well as native oxide (the presence of surface OH groups) substantially enhance the process of LAO.

6.3.2 Tip induced LAO during C-AFM on μ c-Si:H

In case of the microcrystalline silicon the situation is very similar. After the deposition the sample surface is *H* terminated and native oxide layer forms in a similar way as on the crystalline silicon. Therefore, in case of applied positive sample bias during C-AFM the tip induced LAO process will take place. LAO makes the interpretation of the local current in C-AFM difficult, see for example ”memory effect” in fig. 6.6. In the comment [86] we have shown that the LAO process can lead to controversial

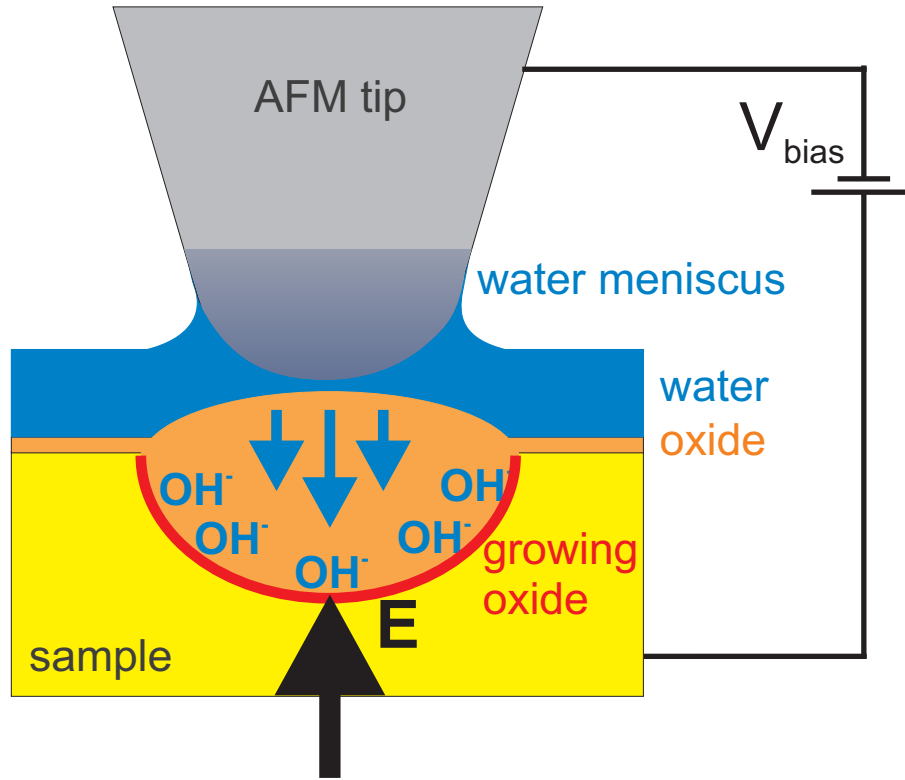


Figure 6.5: Schematic representation of the tip induced nano-oxidation mechanism on the surface of silicon

explanations of the local current maps, like in the work of Azulay et al. [70], where conductive rings at the GBs were observed and interpreted as the main transport route in μ c-Si:H). We consider below in this section how such artifact appears.

The "memory effect" was also observed by other groups, see for example [54, 87]. First, the μ c-Si:H sample was scanned in a smaller area with a high oxidizing voltage (+10 V). Then, the current map in fig. 6.6a was recorded across a bigger area with non-oxidizing voltage of -5 V. The previously scanned area appears dark as the current values were decreased by about one order of magnitude. The same area is rendered in fig. 6.6b in a finer current scale to visualize the details. It can be seen that the oxidation led not only to overall lower currents but also to a change of features in the current image. The current lowering is more pronounced on the grains than at grain edges and so the edges appear brighter than the grain interiors. As a result, the grain edges in the oxidized image form rings of relatively higher conductivity.

To confirm that the tip induced LAO takes place during the C-AFM measurement we designed a next experiment. LAO leads to characteristic topographical changes (see for example [55]), but up to now it was not possible to detect them in C-AFM experiments with typical μ c-Si:H due to the roughness of amorphous silicon (usually

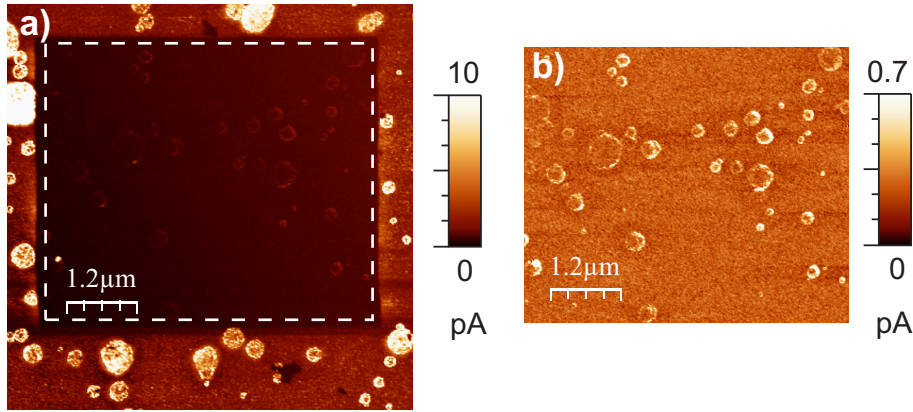


Figure 6.6: Memory effect in the local current image of $\mu\text{c-Si:H}$ thin film. The $6 \times 6 \mu\text{m}^2$ scan shown in a) was measured at -5 V bias after the previous $+10 \text{ V}$ scan of the central area $5 \times 4.5 \mu\text{m}^2$. The previously scanned (dark) area is not only less conductive, but it also shows a different character of local currents as seen in b) where it is plotted again with adjusted color scale. The grains now appear more conductive at the edges.

RMS roughness is around $5 - 10 \text{ nm}$ instead of 0.1 nm for polished c-Si). For this reason we made a special sample with very smooth surface of the amorphous parts (for amorphous tissue the RMS roughness was approx. 0.3 nm), which enabled us to observe directly the elevation of locally oxidized surface above its surroundings.

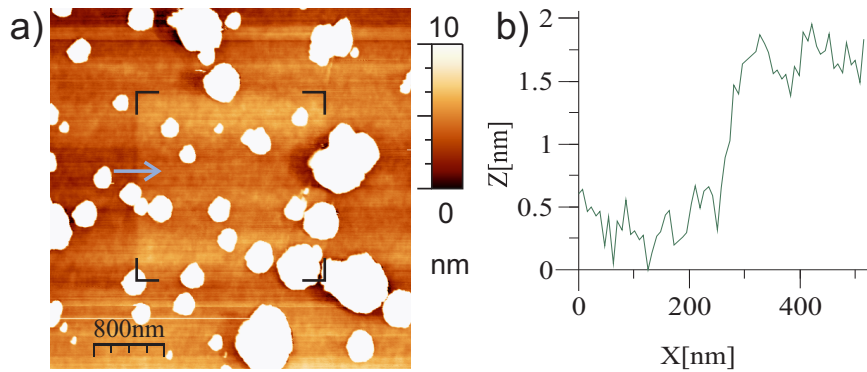


Figure 6.7: Topographical changes due to LAO during ambient C-AFM of the mixed phase sample: a) height image of $4 \times 4 \mu\text{m}^2$ area of the $\mu\text{c-Si:H}$ surface where the central $2 \times 2 \mu\text{m}^2$ area (marked by corners) was previously scanned at $+10 \text{ V}$ sample bias. b) Height profile across the boundary between the pristine and oxidized areas shows an increase of height by about 1 nm (marked by the arrow).

Fig. 6.7a shows the topographical image of the sample where the central area was oxidized by the previous scan at $+10 \text{ V}$. The grains are much higher than the 10 nm color range and therefore they appear just white. Increase of the local height of the amorphous surface due to oxidation can be seen in the area marked by dark corners

and was estimated to be about 1 nm from the line profile across a boundary of the oxidized area (as shown in fig. 6.7b). Note that this height does not correspond to the oxide thickness as there is already some native oxide on the surface and because LAO leads to the oxide growth also into the sample interior [80, 83].

Neighbor line oxidation artifact Because of the water meniscus between AFM-tip and scanned surface, the oxide growth induced by the AFM tip proceeds also laterally and the fig. 6.8 shows the result of another experiment on mixed phase sample designed to find the width of the oxide line. The sample was oxidized in a zig-zag pattern (along the path marked by the dashed line in fig. 6.8) at +10 V and then imaged as the local current map at -2.5 V. It can be seen that the scanning tip at oxidizing bias leaves behind an oxide line which influenced the local current within a cca 50 nm wide band, in agreement with the minimal line widths in LAO based lithography [55]. Thus the oxidized line is several times wider than the separation of the individual lines in the typical AFM scans: commonly used 256 lines per image lead to 8 nm separation of scan lines for a 2 μ m wide field of view. This means that at oxidizing conditions only the first line actually scans the pristine surface and all subsequent neighboring lines record the local current values on already locally oxidized surface.

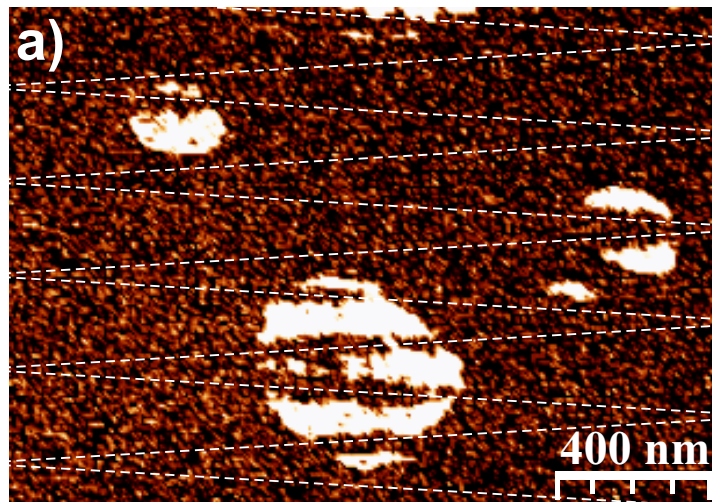


Figure 6.8: Local current map measured at non-oxidizing -2.5 V bias after the previous zig-zag scan (along the path marked by the white dashed line) at +10 V sample bias. The dark (less conductive) lines across the bright (more conductive) grains illustrate the width of the oxidized lines

The neighboring line oxidation artifact can lead to the conductive ring formation already in the very first scan of the sample. Fig. 6.9 shows C-AFM measurements

on the same μ c-Si:H sample which was measured at non-oxidizing -2 V sample bias (left) and at oxidizing $+10$ V (right). The expected width of the oxidized line (50 nm) is about 10 times bigger than the 5 nm separation of the scan lines in fig. 6.9b. Therefore before a point in the local current map is taken, it was already oxidized by approx. 10 passages of the AFM tip in the previous line scans. The local current image is similar to the image in fig. 6.6b, showing similar current scale and again the conductive rings at the grain edges.

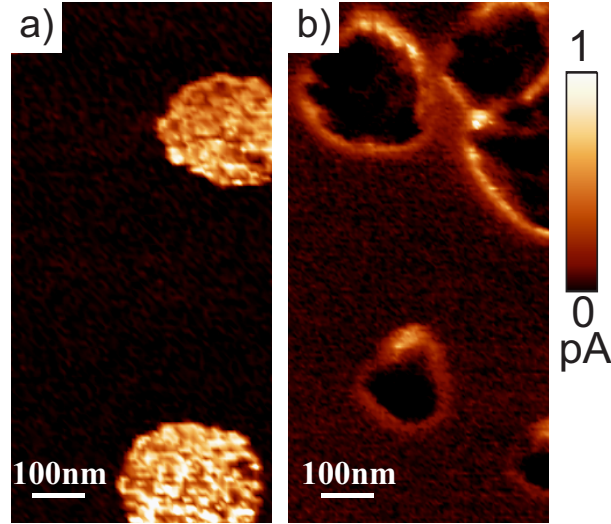


Figure 6.9: Comparison of the ambient C-AFM images of local current measured on the μ c-Si:H with native oxide at non-oxidizing -2 V sample bias (left) and at oxidizing $+10$ V (right). Both images have the same color scale. Note the conductive rings in part b which are an artifact due to neighboring line oxidation at the oxidizing voltage $+10$ V)

6.3.3 Discussion of C-AFM results affected by LAO

In particular, we have demonstrated that the choice of polarity and magnitude of the applied sample bias as well as place on a sample with unknown history complicates the reproducibility and interpretation of the C-AFM results.

The oxidation of the silicon surface by air or locally by the C-AFM tip presents a major complication for the quantitative as well as qualitative interpretation of the local currents observed in ambient C-AFM.

It is clear that the oxidation during C-AFM at high positive sample voltages alters μ c-Si:H conductivity maps. In particular, we have demonstrated how the local anodic oxidation can lead to a surprising artifact of the more conductive rings at the grain boundaries (see figs. 6.6 and 6.9b). The measurement conditions corresponded to the

experiments from [70], so we consider the interpretation of the grain boundaries as the main conduction transport route to be misleading. The higher conductivity at the grain edges reflects a state of the surface of the sample and so it cannot be used for arguing about the transport route within the material itself.

Hindering of anodic oxidation at the grain edges What is the actual mechanism which leaves the grain edges relatively more conductive after the oxidation? Several processes can play a role.

First of all, the grain edge geometry may offer a bigger contact area to the tip. This geometrical effect led to an appearance of the apparently more conductive grain boundaries in C-AFM with worn metal coating on the tip. However, we should observe the geometric effect also at the scans at a low or opposite (negative) bias voltages and we found no evidence for it.

A more probable explanation is that the anodic oxidation itself is hindered at the grain boundary. This can be due again to geometrical reasons (grain edges), to the decline in oxidation rate due to build up of space charge [80] or a higher resistance of the boundary between the grain and surrounding amorphous tissue. In particular, the voltage drop due to the higher boundary resistance would decrease the field assisting the migration of ions necessary for the anodic oxidation and hence lead to the oxide layer being thinner in the vicinity of the GB. In that case, the conductive rings at the grain edges in oxidized state would actually support the notion of less conductive GBs in μ C-Si:H to which the defects and impurities (hydrogen, oxygen and contaminants) concentrate.

The last possibility is electrical breakdown, which is more probable right at the GBs and grain edges again due to the space charge and geometrical reasons [74] and which may have been responsible for the current spikes observed in [87], attributed to the GB related short-circuits.

6.3.4 Measurement of local I-V characteristics in ambient

The tip induced LAO with charge trapping during ambient C-AFM makes it impossible to measure repeated $I - V$ characteristics on the same place. Most often it is not possible to measure correctly even one single $I - V$ curve. Positive sample bias and/or high voltage rapidly change the local properties of the sample surface (see fig. 6.10). It has to be noted that this is one of the best examples when LAO was excluded by low negative sample bias. If one would measure $I - V$ characteristic on

a silicon thin film at positive and/or high sample bias, the local current would drop to negligible small values (due to the "memory"-effect) during the very first run.

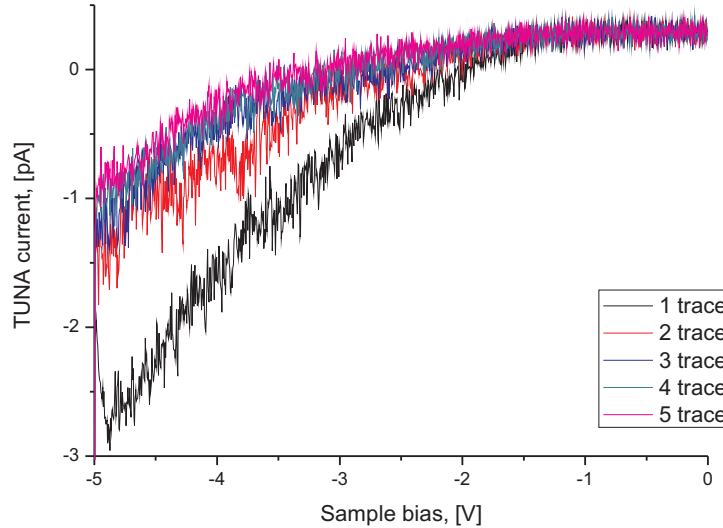


Figure 6.10: $I - V$ curves measured on microcrystalline grain on the same place. The first run shows maximum current, each next run demonstrates reduced local current compared to the previous one

Because of the fact that the sample bias voltage higher than a threshold of several volts is needed for the LAO process, one has to use low negative sample bias to prevent the oxide growth. Again, to make statistical evaluations of the measurements it is necessary to measure each $I - V$ curve on pristine surface. Fig. 6.11 shows results measured at ambient atmosphere: $I - V$ curves from 7 points on microcrystalline grains and 6 points on the amorphous tissue at low negative sample bias. We received very good reproducibility of the results from different grains.

These measured $I - V$ curves support our model of conductive microcrystalline grains embedded in much less conductive amorphous tissue.

6.4 HF etch for restoring local electrical properties of the sample

As it was already considered in this chapter, the native oxide as well as water layer, significantly complicates C-AFM measurements. Therefore, we experimented with stripping the oxide on mixed phase sample by brief etch in diluted HF acid.

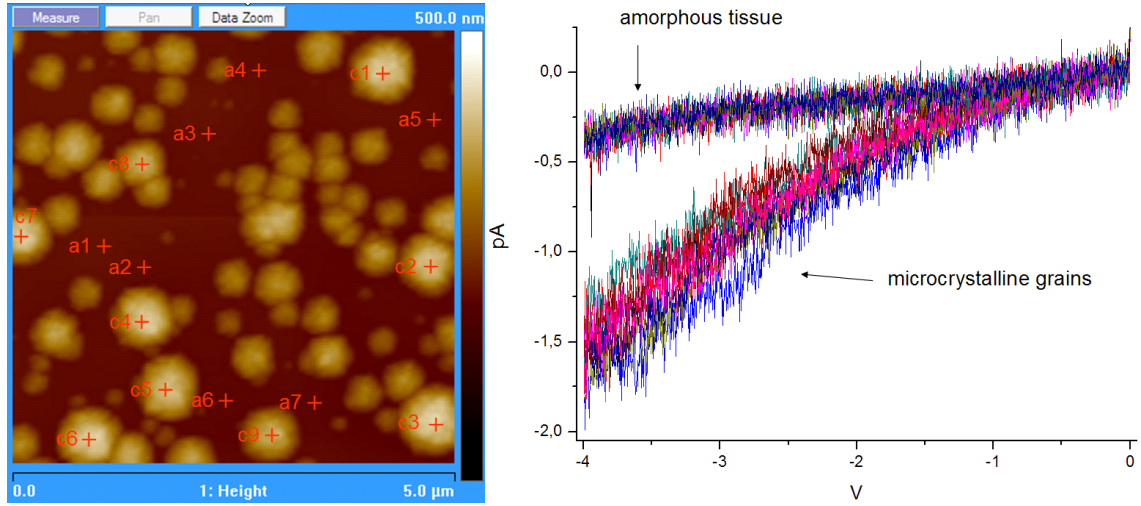


Figure 6.11: $I - V$ curves measured on microcrystalline grains (7 points, marked as "c" with number) and on the amorphous tissue (6 points, marked as "a" with number) at low negative sample bias.

We have used the following procedure for removing the oxide from the surface of the $\mu\text{c-Si:H}$ films: samples were put into 10 % water solution of HF for a few seconds, rinsed by deionized water and blown dry by an air jet. After that the sample surface is H-terminated, therefore it is hydrophobic. As a result the surface is clean with no native oxide on it for approx. 1 hour. This time is enough to make C-AFM scan on the sample.

Fig. 6.12 compares the local current maps measured on the same sample with a native oxide (left) and after the oxide stripping (right). The color scale for local currents is the same for both measurements. The oxide stripping increased the uniformity as well as the average value of local current registered on the grains (so much that we had to reduce the bias from -1.5 V to -0.7 V to adjust the currents to the range of the instrument sensitivity). The negative sample polarity and a low bias voltage lead to excellent reproducibility of the local current maps even after four repeated scans.

Restoration of the surface by HF etch not only increases the values of local currents in ambient C-AFM but also makes the character of the local current maps to resemble those obtained in UHV much more. However, direct comparison of the local current levels in UHV on an in-situ prepared sample and on the same sample after ageing in air and stripping the oxide has yet to be done.

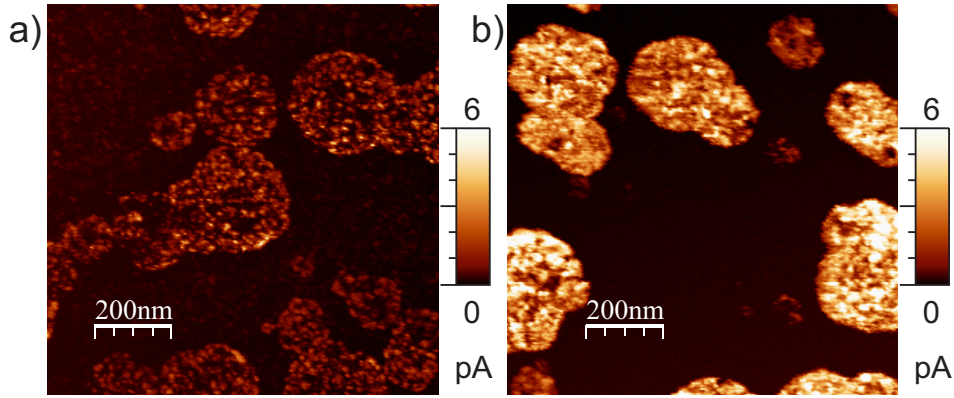


Figure 6.12: Comparison of the ambient C-AFM images of local current measured on $\mu\text{c-Si:H}$ with native oxide (left) and with the surface restored by HF etch (right). Both images have the same color scale.

6.5 Dependence of local current on the grain dimensions

Since sample deposition takes place in vacuum, there is no oxide on the sample surface immediately after removing it from deposition chamber. As opposite to the etching process which was described in previous section, the sample surface can be covered by thin amorphous layer. In our opinion, such layer can exist due to the unstable conditions at the very end of the deposition when plasma discharge was switched off. In this case an interface between $\mu\text{c-Si:H}$ and thin amorphous layer appears, which can be the reason for charge trapping even in UHV conditions.

Our C-AFM measurements on $\mu\text{c-Si:H}$ samples made immediately after removing from the deposition chamber show lower currents than on the samples after HF-etch, but the same uniformity of the local current as in case of UHV C-AFM (see fig. 6.13a).

We designed special technique to deposit $\mu\text{c-Si:H}$ thin film with different dimensions of microcrystalline grains. It is based on slightly changing of the deposition conditions during the film growth from predominantly amorphous to predominantly microcrystalline. As a result, microcrystalline grains start to nucleate at different depths which leads to grains with different sizes.

For the sample with different grain sizes we observed different local currents which flow from grains to the grounded AFM-tip. Fig. 6.13c shows line profile in the map of local currents. Microcrystalline grains which are connected to each other demonstrate the same high local current level regardless of grain size. Therefore, for calculation of average current flowing through a grain we made such profiles through centers of

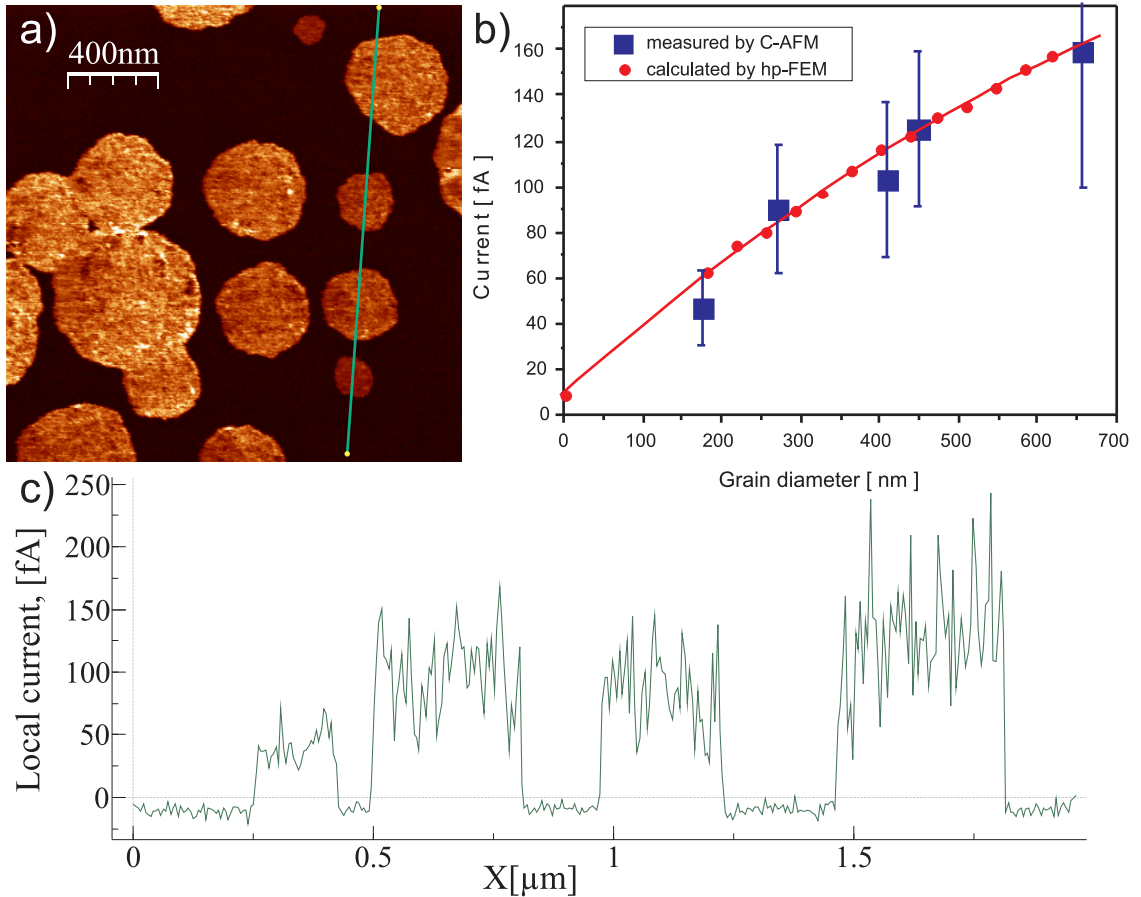


Figure 6.13: a) $2 \times 2 \mu\text{m}^2$ map of local currents observed by the tip of the ambient conductive AFM on the sample immediately after the deposition. Sample bias was applied to the bottom electrodes; b) The currents flowing from microcrystalline grains to the grounded tip depend on the grain sizes: the dependence of the local current on the dimensions of solitary grains is shown; c) The plot shows the line profile along the line used to find average current value on the grains.

solitary microcrystalline grains, the square under the grain profile was divided by its diameter. Resulting dependence is shown on fig. 6.13b.

These results were also used for comparison with numerical calculations of the internal field distributions in the C-AFM and $\mu\text{C-Si:H}$ sample by adaptive higher-order polynomial finite-element methods according to our model. The work is at initial stage, but the first results have been already presented here [88].

The local current dependence on the dimension of the microcrystalline grain was observed on a film over bottom contact and also on the same film over the gap (at distance of few tens of microns from the nearest bottom contact) between contacts as well (see fig. 4.1). Moreover, we didn't observe noticeable difference in the local currents in both cases. That means, the conductivity of the bulk material is much

higher than resistivity of the combination of AFM-tip - contact resistance - sample. This lead us to the experiments with coplanar contact geometry.

6.6 Coplanar contacts geometry

Further experiments with C-AFM of $\mu\text{C-Si:H}$ were done with the coplanar geometry (see fig. 6.14a), in which the transport parallel to the substrate is measured.

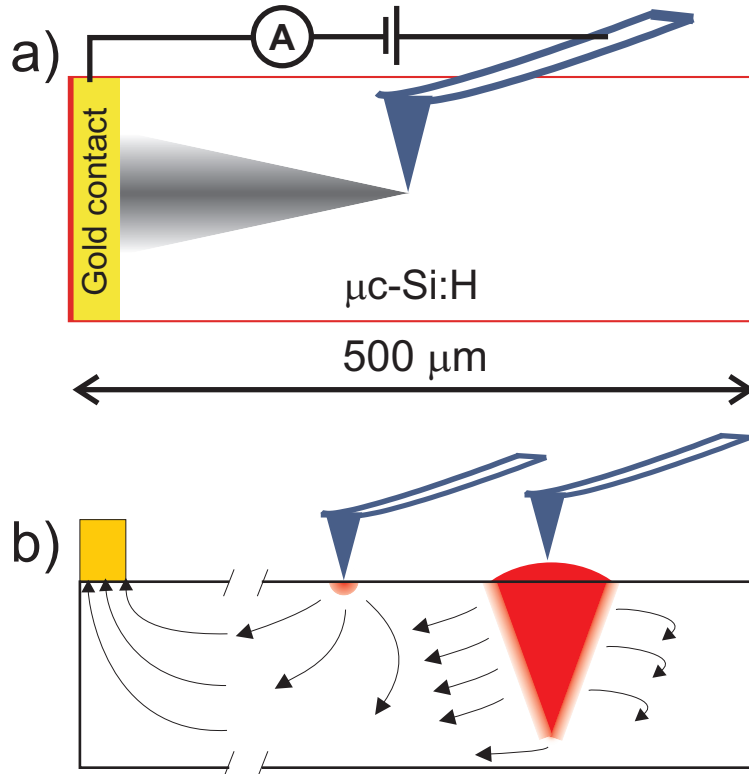


Figure 6.14: (a) Scheme of the experiment in which the local sample conductivity is measured by AFM with a conductive cantilever, and the current, spreading from the tip of the cantilever, is collected to the side electrode made by a lithographically defined evaporated layer of gold; (b) Cross-section of the side view in which the current flux lines are schematically shown at the gold contact and near the tip-surface junction at two different positions: on the amorphous surface and on a highly conductive microcrystalline grain

6.6.1 Model for mechanism of charge transport parallel to a substrate

We have suggested the model based on the density of states (DOS) for the components present in the films and the transport path within the DOS, as illustrated

in fig. 6.15. The scheme on the left shows the commonly accepted DOS for a-Si:H. The DOS for the isolated large grains of μ c-Si:H in the center of fig. 6.15 also shows the tail states due to the grain boundaries of the small grains. These two images are aligned according to the conduction band offset less or around 0.1 eV and the valence band edge offset around $0.2 - 0.6\text{ eV}$, corresponding to the mobility gap of μ c-Si:H fluctuating in the range $1.5 - 1.1\text{ eV}$ for different microstructures [89].

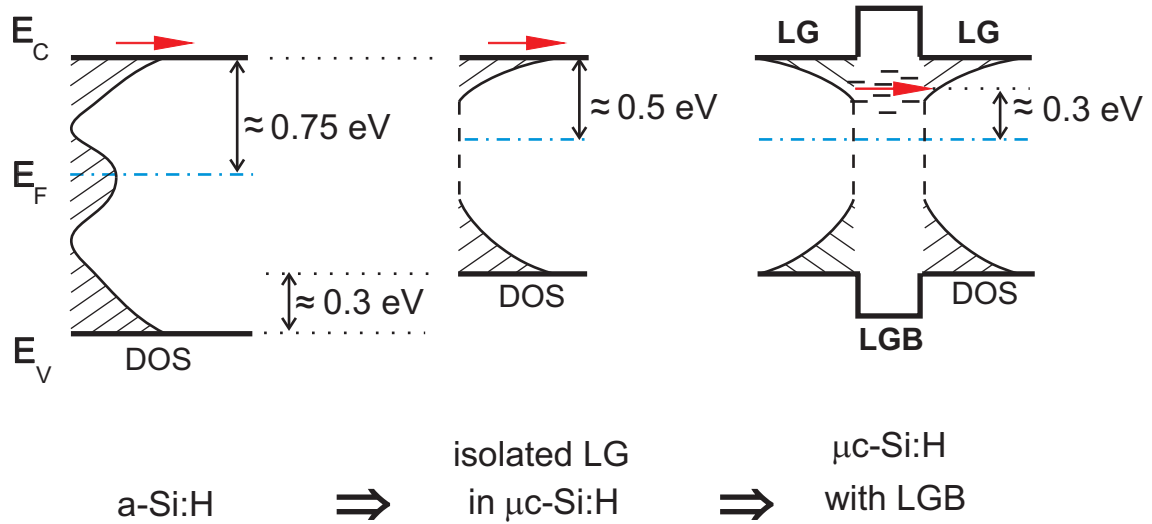


Figure 6.15: Schematic illustration of the components present in the mixed-phase silicon films. The components are present in various concentrations at different film crystallinity, increasing from left to right. Localized densities of states (DOS) are schematically marked and the transport paths through the transport-limiting step are marked by arrows.

The scheme on the right part of fig. 6.15 shows the μ c-Si:H with the densely packed large grains connected by grain tissue (large grain boundaries) with the band gap higher due to the concentration of oxygen or hydrogen into LGBs. The transport path (see the right scheme in fig. 6.15), which now takes place through the tail states within the large grains and by hopping or tunneling through the LGB and/or a-Si:H tissue, see fig. 6.16a).

We believe that this is the main conduction path for charge transport. One more argument for support of this theory is illustrated on fig. 6.13a. Note the same level of the local current flowed through coalesced grains with different dimensions. This means that all these grains are electrically connected and the resistance of large grain boundaries between them is much less than the resistance of amorphous layer between them and bottom contact.

We do not agree with the proposal that the path is fully and only through the LGB or a-Si:H tissue (see fig. 6.16b), as stated by [70]. The LGBs need to be seen

rather as the transport-limiting step which determines the resulting thermal behavior of the conductivity. Our model of transport is based on the existence of the third phase, the LGB, proposed to explain the changes of the prefactor and activation energy upon the a-Si:H/ $\mu\text{C-Si:H}$ transition, and the same conclusion has been drawn from the crystallinity value at which the percolation threshold occurs.

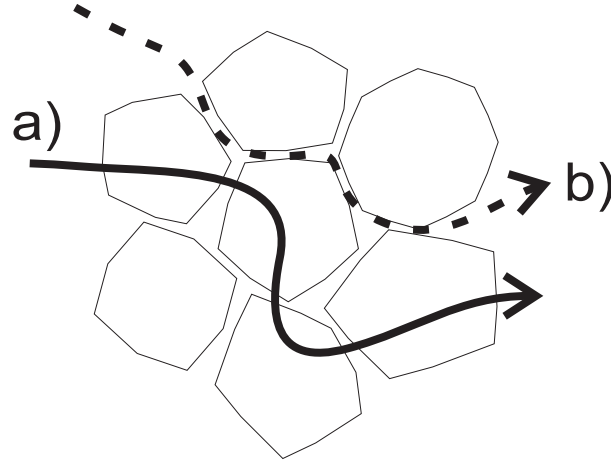


Figure 6.16: Schematic picture of the different possible transport routes

6.6.2 Dependence of the average current registered on the different grains at various distances from gold contact

Here we present the C-AFM results on a $\mu\text{C-Si:H}$ sample, with crystallinity $X_c \approx 50\%$, i.e. corresponding to the mixed phase $\mu\text{C-Si:H}$. The standard "macroscopic" coplanar contacts with the gap changing from 0.2 to 2 mm have been prepared on a 5×10 mm glass substrate and used to measure the coplanar conductivity (see Section 6.1.2), which for this sample was $\sigma_D = 8 \cdot 10^{-8} \Omega^{-1} \text{cm}^{-1}$. Using the sample deposited on glass from the same deposition (see Fig. 4.3), we have performed the C-AFM measurements. The current was collected laterally by a lithographically defined gold contact to which the voltage of -1.4 V was applied with respect to the grounded AFM tip. Several positions of the AFM field of view were chosen, at the gold contact edge and at distances up to $500 \mu\text{m}$ from it (see the scheme in fig. 6.14a). Figure 6.17 shows three current maps within the field of view $2 \times 2 \mu\text{m}^2$ at the tip for electrode distances of 0, 250 and $500 \mu\text{m}$. A surprising observation is that, in the left current map in fig. 6.17, the average current observed on the grains almost does not depend on the distance from the contact edge. We have expected that the current measured on the grains in contact with the Au electrode would be much higher but

this was not the case. This apparent paradox is probably due to the thin native oxide layer which was formed on the surface of $\mu\text{c-Si:H}$ in air.

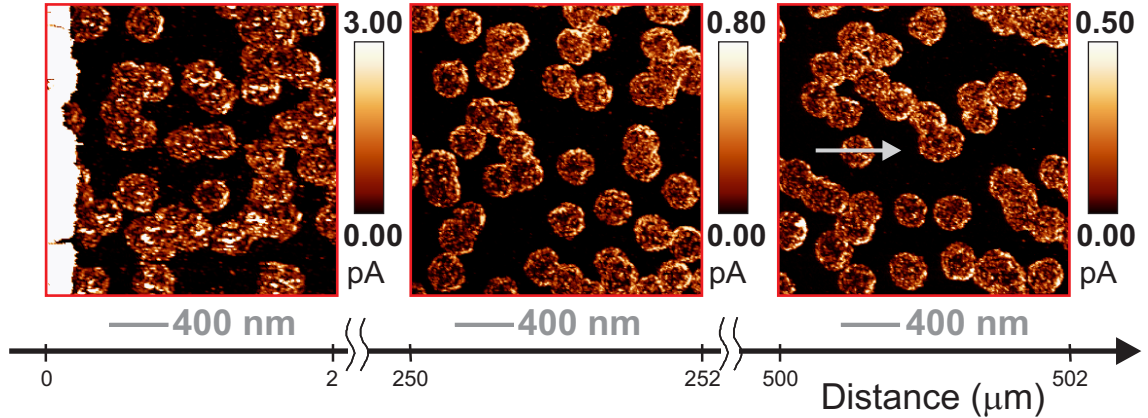


Figure 6.17: Local current maps measured by AFM with a conductive cantilever using the applied voltage of 1.4 V within the $2 \times 2 \mu\text{m}^2$ field of view. As shown in fig. 6.14, the current was collected through the film to a lithographically defined gold electrode at the distances indicated by the broken X axis. Note different current scale magnitudes shown as color scales. The arrow indicated in the right map marks the trace, along which the line profile is shown in fig. 6.18. About 300 nm large grains, composed of small crystallites, are evident.

The fact that the contrast of the scan, even at the distance 500 μm from the electrode, looks similar to the one at 0 mm may also seem rather surprising. But note that the maximum current, corresponding to the white color, decreases with the distance, as expected due to the current collection to the electrode aside from the tip. To quantify the changes of the current we had to average out the current noise due to the intermittent contact of the scanning tip. The current averaging was carried out along many line profiles over the grains (see fig. 6.18a) and the resulting currents are plotted as a function of the tip-contact distance in fig. 6.18b. The decrease of the current approximately corresponds to the additional film resistance expected for the observed film conductivity ($\sigma_D = 8 \cdot 10^{-8} \Omega^{-1} \text{cm}^{-1}$), which the current has to overcome on its way to the contact. The precise fit of the curve in fig. 6.18b is difficult due to geometry (tip versus coplanar electrode) and unknown transition resistances (tip native oxide, etc.).

The clearly expressed contrast between the grains and a-Si:H tissue even for the scan at 500 μm is given by the fact that on a-Si:H tissue the tip represents the real point contact (see fig. 6.14), whereas on the grains it contacts more conductive Si nanocrystals, which then pass the current to the a-Si:H layer through a substantially increased area. In other words, the difference of the current level on the grains and

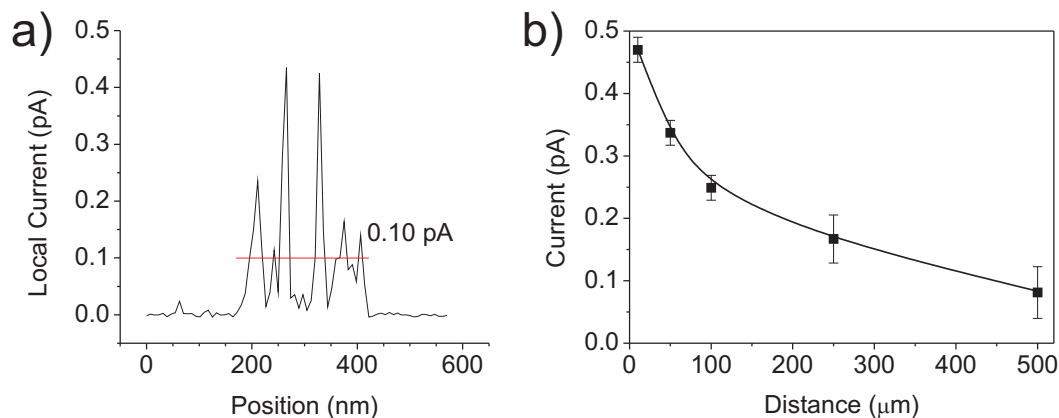


Figure 6.18: (a) Line profile of the local current measured by AFM with a conductive tip along the arrow in fig. 6.17 showing also the average local current measured on one of the grains. (b) Dependence of the average current registered on the different grains at various distances from the edge of the current collecting gold electrode. The line is a guide to the eye.

on the amorphous phase can be understood as the difference of the a-Si:H spreading resistance of the tip-a-Si:H and the tip-grain-a-Si:H junctions. At the same time, this is more proof that the Si grains are highly conductive in the whole volume, not just at the column boundaries.

Chapter 7

CONCLUSIONS

The present thesis has focused on two mutually dependent aspects of the films. The first one concerns the structure and mechanical properties of the mixed phase samples studied by Raman microspectroscopy. The second studied aspect was oriented to the local electrical properties studied by conductive atomic force microscopy. Understanding of all these aspects is important on the way to cheap and efficient thin film solar cells.

Raman microspectroscopy

In the thesis it was shown that the Raman microspectroscopy is a very important and easily applicable tool for investigation of thin films of microcrystalline silicon. It is excellent (fast, non-destructive and very sensitive) technique for crystallinity estimation of the whole range of possible sample structures: from fully amorphous to microcrystalline.

We also have shown, that the lateral resolution of the method was 350 nm with excitation wavelength of 442 nm. Furthermore, at certain conditions the Raman microspectroscopy can exceed the optical diffraction limit and microcrystalline grains as small as 160 nm can be detected.

The combination of Raman microspectroscopy and AFM promises further improvement of the resolution and, hopefully, in the near future it will be possible to resolve large grain boundaries in microcrystalline structure.

We developed the setup for stress creation in $\mu\text{c-Si:H}$ thin films deposited onto silicon flexible cantilevers. Elastic properties of thin silicon cantilever allows bending with curvatures less than 0.3 mm^{-1} which corresponds (for 2 μm thick cantilevers) to creating compressive or tensile stresses up to 1 GPa. We demonstrated that the positions of the Raman peaks change linearly with stress both for $\mu\text{c-Si}$ and for a-

Si:H films. Further development of the technique, namely, the adding of force detection during the cantilever bending will make it possible to measure other parameters, such as Young's module or constant for stress determination by Raman, quantitatively.

Conductive atomic force microscopy

Conductive atomic force microscopy is one of the main tools for studying of electrical properties at nanoscale. In the thesis we have considered peculiarities of the C-AFM measurements and $I - V$ characteristics obtained in ultra high vacuum and in ambient atmosphere as well.

We have demonstrated why the high positive sample bias during the C-AFM scan has to be avoided. It was shown that the local anodic oxidation can alter map of electronic properties (in particular leading to the appearance of the conductive rings at the grain boundaries). We also estimated the threshold for oxidation of $\mu\text{c-Si:H}$ surface to be approx. 5 V , which is similar to the case of crystalline silicon. We have shown how the tip induced LAO of the neighboring lines changes the local current maps measured at ambient conditions even at the very first scan of pristine surface. The recommendations how to properly set up the C-AFM measurement in order to avoid various artifacts were done.

We have compared results from UHV and ambient C-AFM and demonstrated how to strip the native oxide to achieve current values and maps comparable to the measurements in UHV.

In this work the C-AFM results with different contact geometry: vertical ("sandwich") and coplanar were compared. Relying on all our results we introduced new observations and concepts to be added to the model of transport in microcrystalline silicon (see Section 6.1.1).

One of the most important results of this work is that the methods described above can be applied to a wide range of other materials which are used in thin films solar cells. We continue to develop our methods and expand the number of studied samples. We already have some first results on such new materials as SiO_x films used as intermediate reflector, ZnO transparent contacts, polycrystalline silicon thin films, carbon nanowalls. And this list can be continued. At the same time, new measurement methods extend the range of material which can be studied. For example, TR-TUNA (see Section 3.2.1) allows one to make maps of local currents of soft or elastic structures which was impossible to do in contact mode. Of course, it is still desirable to improve these methods, namely: to achieve higher lateral resolution, reproducibility

of local I-V characteristics to have a possibility to compare the measurements made on the same place (for example, made under lighting and in the dark or before and after some processing), measuring of I-V characteristics of single grain boundaries, etc.

Bibliography

- [1] Takuya Matsui. PhD thesis, Graduate School of Engineering Science, Osaka University (2002).
- [2] W. B. Jackson. *Optical absorption spectra of surface or interface states in hydrogenated amorphous silicon*. Applied Physics Letters, **42**(1), 105 (1983).
- [3] A. Shah, J. Meier, E. Vallat-Sauvain, C. Droz, U. Kroll, N. Wyrsh, J. Guillet and U. Graf. *Microcrystalline silicon and 'micromorph' tandem solar cells*. Thin Sol. Films, **403–404**, 179–187 (2002).
- [4] J. Meier, J. Spitznagel, U. Kroll, C. Bucher, S. Fay and A. Shah. *High efficiency micromorph tandem solar cells*. In *Proceedings of the 3rd World Conference on Photovoltaic Energy Conversion*, Osaka, Japan (2003). WCPEC.
- [5] R. A. Street. *Hydrogenated amorphous silicon*. Cambridge Solid State Science Series. Cambridge University Press, Cambridge (1991).
- [6] D.L. Staebler and C.R. Wronski. *Reversible conductivity changes in discharge produced amorphous Si*. Appl. Phys. Lett., **31**, 292–294 (1977).
- [7] Jef Poortmans and Vladimir Arkhipov. *Thin film solar cells : fabrication, characterization, and applications*. John Wiley & Sons Ltd, The Atrium, Southern Gate, Chichester, West Sussex PO19 8SQ, England (2006).
- [8] D. M. Mattox. *Handbook of physical vapor deposition (PVD) processing: film formation, adhesion, surface preparation and contamination control*. William Andrew (1998).
- [9] L. B. Freund and S. Suresh, editors. *Thin Film Materials: Stress, Defect Formation and Surface Evolution*. Cambridge University Press (2004).
- [10] Peter Sigmund. *Mechanisms and theory of physical sputtering by particle impact*. Nuclear Instruments and Methods in Physics Research Section B: Beam Interactions with Materials and Atoms, **27**(1), 1–20, June 1987.
- [11] D. Mataras, F. Coutelieris, P. Kounavis and D. E. Rapokoulis. *Dilution-enhanced radical generation in silane glow discharges*. J. Phys. D: Appl. Phys., **29**, 2452–2458 (1996).
- [12] A.S. Ferlauto, R.J. Koval, C.R. Wronski and R.W. Collins. *Extended phase diagrams for guiding plasma-enhanced chemical vapor deposition of silicon thin films for photovoltaics applications*. Appl. Phys. Lett., **80**(15), 2666–2668 (2002).
- [13] S. Okamoto, Y. Hishikawa and S. Tsuda. *New interpretation of the effect of hydrogen dilution of silane on glow-discharged hydrogenated amorphous silicon for stable solar cells*. Jpn. J. Appl. Phys., **35**, 26–33 (1996).

- [14] Atif Mossad Ali. *Mechanisms of the growth of nanocrystalline Si:H films deposited by PECVD*. Journal of Non-Crystalline Solids, **352**(28-29), 3126–3133, August 2006.
- [15] J. Koh, A.S. Ferlauto, P.I. Rovira, C.R. Wronski and R.W. Collins. *Evolutionary phase diagrams for plasma-enhanced chemical vapor deposition of silicon thin films from hydrogen-diluted silane*. Appl. Phys. Lett., **75**(15), 2286–2288 (1999).
- [16] Y. Ziegler, V. Daudrix, C. Droz, R. Platz, N. Wyrsh and A. Shah. *More stable low gap a-Si:H layers deposited by PE-CVD at moderately high temperature with hydrogen dilution*. Sol. Energy Mater. Sol. Cells, **66**, 413–419 (2001).
- [17] Y. Nasuno, M. Kondo and A. Matsuda. *Passivation of oxygen-related donors in microcrystalline silicon by low temperature deposition*. Appl. Phys. Lett., **78**(16), 2330–2332 (2001).
- [18] G. Ganguly and A. Matsuda. *Defect formation during growth of hydrogenated amorphous silicon*. Phys. Rev. B, **47**, 3661 (1993).
- [19] A.V. Shah, R. Platz and H. Keppner. *Thin-film silicon solar cells: A review and selected trends*. Sol. Energy Mater. Sol. Cells, **38**, 501 (1995).
- [20] Y. Nasuno, M. Kondo and A. Matsuda. *Effects of substrate surface morphology on microcrystalline silicon solar cells*. Jpn. J. Appl. Phys., **40**, L303–L305 (2001).
- [21] M. B. Schubert. *Low temperature silicon deposition for large area sensors and solar cells*. Thin Sol. Films, **337**, 240–247 (1999).
- [22] M. Ito, C. Koch, V. Švrček, M. B. Schubert and J. H. Werner. *Silicon thin film solar cells deposited under 80 °C*. Thin Sol. Films, **383**, 129–131 (2001).
- [23] Y. Mai, S. Klein, R. Carius, J. Wolff, A. Lambertz, F. Finger and X. Geng. *Microcrystalline silicon solar cells deposited at high rates*. Journal of Applied Physics, **97**(11), 114913–12, June 2005.
- [24] T. Mates, A. Fejfar, I. Drbohlav, B. Rezek, P. Fojtík, K. Luterová, J. Kočka, C. Koch, M.B. Schubert, M. Ito, K. Ro and H. Uyama. *Role of grains in protocrystalline silicon layers grown at very low substrate temperatures and studied by atomic force microscopy*. J. Non-Crystal. Solids, **299–302**, 767–771 (2002).
- [25] T. Matsui, M. Kondo and A. Matsuda. *Origin of the improved performance of high-deposition-rate microcrystalline silicon solar cells by high-pressure glow discharge*. Jpn. J. Appl. Phys., **42**, L901–L903 (2003).
- [26] M. Matsumoto, M. Shima, S. Okamoto, K. Murata, M. Tanaka, S. Kiyama, H. Kakiuchi, K. Yasutake, K. Yoshii, K. Endo and Y. Mori. *Extremely high-rate deposition of silicon thin films prepared by atmospheric plasma CVD method with rotary electrode*. In *Proceedings of the 3rd World Conference on Photovoltaic Energy Conversion*, Osaka, Japan (2003). WCPEC.
- [27] R. E. I. Schropp and M. Zeman, editors. *Amorphous and microcrystalline silicon solar cells: Modeling materials and device technology*. Kluwer Academic Publishers, Dordrecht, The Netherlands (1998).

- [28] B. Strahm, A.A. Howling, L. Sansonnens, Ch. Hollenstein, U. Kroll, J. Meier, Ch. Ellert, L. Feitknecht and C. Ballif. *Microcrystalline silicon deposited at high rate on large areas from pure silane with efficient gas utilization*. Solar Energy Materials and Solar Cells, **91**(6), 495–502, March 2007.
- [29] T. Matsui, M. Kondo and A. Matsuda. *Origin of the improved performance of high-deposition-rate microcrystalline silicon solar cells by high-pressure glow discharge*. Jpn. J. Appl. Phys., **42**, L901–L903 (2003).
- [30] S. Veprek, F. -A. Sarrott, S. Rambert and E. Taglauer. *Surface hydrogen content and passivation of silicon deposited by plasma induced chemical vapor deposition from silane and the implications for the reaction mechanism*. Journal of Vacuum Science & Technology A: Vacuum, Surfaces, and Films, **7**(4), 2614–2624, July 1989.
- [31] S. Suzuki, M. Kondo and A. Matsuda. *Growth of device grade c-Si film at over 50 Å/s using PECVD*. Solar Energy Materials and Solar Cells, **74**(1-4), 489–495, October 2002.
- [32] M. Kondo, S. Suzuki, Y. Nasuno, M. Tanda and A. Matsuda. *Recent developments in the high growth rate technique of device-grade microcrystalline silicon thin film*. Plasma Sources Sci. Technol., **12**(4), S111–S116 (2003).
- [33] J. Bailat, E. Vallat-Sauvain, A. Vallat and A. Shah. *Simulation of the growth dynamics of amorphous and microcrystalline silicon*. Journal of Non-Crystalline Solids, **338-340**, 32–36, June 2004.
- [34] G. van Elzaker, V. Nádaždy, F.D. Tichelaar, J.W. Metselaar and M. Zeman. *Analysis of structure and defects in thin silicon films deposited from hydrogen diluted silane*. Thin Solid Films, **511-512**, 252–257, July 2006.
- [35] T. Sugano, T. Kitagawa, Y. Sobajima, T. Toyama and H. Okamoto. *Hybrid-phase growth in microcrystalline silicon thin films deposited by plasma enhanced chemical vapor deposition at low temperatures*. Journal of Applied Physics, **97**(9), 094910–6, May 2005.
- [36] Hiroyuki Fujiwara, Michio Kondo and Akihisa Matsuda. *Interface-layer formation in microcrystalline Si:H growth on ZnO substrates studied by real-time spectroscopic ellipsometry and infrared spectroscopy*. Journal of Applied Physics, **93**(5), 2400–2409, March 2003.
- [37] R. B. Wehrspohn, S. C. Deane, I. D. French, I. Gale, J. Hewett, M. J. Powell and J. Robertson. *Relative importance of the Si–Si bond and Si–H bond for the stability of amorphous silicon thin film transistors*. Journal of Applied Physics, **87**(1), 144–154 (2000).
- [38] Yoshihiro Hishikawa. *Raman study on the variation of the silicon network of a-Si:H*. Journal of Applied Physics, **62**(8), 3150–3155, October 1987.
- [39] U. Kroll, J. Meier, A. Shah, S. Mikhailov and J. Weber. *Hydrogen in amorphous and microcrystalline silicon films prepared by hydrogen dilution*. Journal of Applied Physics, **80**(9), 4971–4975, November 1996.

- [40] J. P. Harbison, A. J. Williams and D. V. Lang. *Effect of silane dilution on intrinsic stress in glow discharge hydrogenated amorphous silicon films*. Journal of Applied Physics, **55**(4), 946–951, February 1984.
- [41] Hiroaki Kakinuma. *Intrinsic stress of phosphorus- and boron-doped amorphous silicon films*. Philosophical Magazine Part B, **57**(5), 671 (1988).
- [42] Hiroyuki Fujiwara, Michio Kondo and Akihisa Matsuda. *Microcrystalline silicon nucleation sites in the sub-surface of hydrogenated amorphous silicon*. Surface Science, **497**(1-3), 333–340 (2002).
- [43] Hiroyuki Fujiwara, Michio Kondo and Akihisa Matsuda. *Stress-Induced Nucleation of Microcrystalline Silicon from Amorphous Phase*. Japanese Journal of Applied Physics, **41**, 2821–2828 (2002).
- [44] Hiroyuki Fujiwara, Michio Kondo and Akihisa Matsuda. *Nucleation mechanism of microcrystalline silicon from the amorphous phase*. Journal of Non-Crystalline Solids, **338-340**, 97–101, June 2004.
- [45] Bernhard Schrader. *Infrared and Raman Spectroscopy: Methods and Applications*. Wiley-VCH, March 1995.
- [46] Shuming Nie and Steven R. Emory. *Probing Single Molecules and Single Nanoparticles by Surface-Enhanced Raman Scattering*. Science, **275**(5303), 1102–1106, February 1997.
- [47] Katrin Kneipp, Martin Moskovits and Harald Kneipp, editors. *Surface-Enhanced Raman Spectroscopy: a Brief Perspective*. Springer (2006).
- [48] Ingrid De Wolf. *Stress measurements in Si microelectronics devices using Raman spectroscopy*. Journal of Raman Spectroscopy, **30**(10), 877–883 (1999).
- [49] K. S. Birdi. *Scanning Probe Microscopes: Applications in Science and Technology*. CRC Press, 1 edition, February 2003.
- [50] Bharat Bhushan. *Springer handbook of nanotechnology*. Springer, November 2006.
- [51] Yang Gan. *Atomic and subnanometer resolution in ambient conditions by atomic force microscopy*. Surface Science Reports, **64**(3), 99–121, March 2009.
- [52] Lin Huang and Chanmin Su. *A torsional resonance mode AFM for in-plane tip surface interactions*. Ultramicroscopy, **100**(3-4), 277 – 285 (2004). Proceedings of the Fifth International Conference on Scanning Probe Microscopy, Sensors and Nanostructures.
- [53] L. Zhang, T. Sakai, N. Sakuma, T. Ono and K. Nakayama. *Nanostructural conductivity and surface-potential study of low-field-emission carbon films with conductive scanning probe microscopy*. Appl. Phys. Lett., **75**(22), 3527–3529, November 1999.

- [54] Daniela Cavalcoli, Marco Rossi, Andrea Tomasi and Anna Cavallini. *Degeneracy and instability of nanocontacts between conductive tips and hydrogenated nanocrystalline Si surfaces in conductive atomic force microscopy*. *Nanotechnology*, **20**(4), 045702 (2009).
- [55] Didier Stiévenard and Bernard Legrand. *Silicon surface nano-oxidation using scanning probe microscopy*. *Progress in Surface Science*, **81**(2-3), 112–140 (2006).
- [56] Peter Van Zant, editor. *Microchip Fabrication, 5th Ed.* McGraw-Hill Professional (2004).
- [57] I. Horcas, R. Fernández, J.M. Gómez-Rodríguez and J. Colchero. *WSXM: A software for scanning probe microscopy and a tool for nanotechnology*. *Rev. Sci. Instr.*, **78**(1), 013705 (2007).
- [58] M. Ledinský, L. Fekete, J. Stuchlík, T. Mates, A. Fejfar and J. Kočka. *Characterization of mixed phase silicon by Raman spectroscopy*. *Journal of Non-Crystalline Solids*, **352**, 1209–1212 (2006).
- [59] V. Paillard, P. Puech, R. Sirvin, S. Hamma and P. Roca i Cabarrocas. *Measurement of the in-depth stress profile in hydrogenated microcrystalline silicon thin films using Raman spectrometry*. *Journal of Applied Physics*, **90**(7), 3276 (2001).
- [60] Ingrid De Wolf. *Micro-Raman spectroscopy to study local mechanical stress in silicon integrated circuits*. *Semiconductor Science and Technology*, **11**(2), 139–154 (1996).
- [61] M. Ledinský, A. Vetushka, J. Stuchlík, T. Mates, A. Fejfar, J. Kočka and J. Štěpánek. *Crystallinity of the mixed phase silicon thin films by Raman spectroscopy*. *Journal of Non-Crystalline Solids*, **354**(19-25), 2253–2257 (2008).
- [62] C. Droz, E. Vallat-Sauvain, J. Bailat, L. Feitknecht, J. Meier, X. Niquille and A. Shah. *Electrical and microstructural characterisation of microcrystalline silicon layers and solar cells*. In *Proceedings of the 3rd World Conference on Photovoltaic Energy Conversion*, Osaka, Japan (2003). WCPEC.
- [63] C. Smit, R. A. C. M. M. van Swaaij, H. Donker, A. M. H. N. Petit, W. M. M. Kessels and M. C. M. van de Sanden. *Determining the material structure of microcrystalline silicon from Raman spectra*. *Journal of Applied Physics*, **94**(5), 3582–3588 (2003).
- [64] V. Paillard, P. Puech, M. A. Laguna, P. Temple-Boyer, B. Caussat, J. P. Couderc and B. de Mauduit. *Resonant Raman scattering in polycrystalline silicon thin films*. *Applied Physics Letters*, **73**(12), 1718–1720 (1998).
- [65] Z. Iqbal, S. Vepřek, A.P. Webb and P. Capezzuto. *Raman scattering from small particle size polycrystalline silicon*. *Solid State Comm.*, **37**, 993–996 (1981).
- [66] V. Paillard, P. Puech, M.A. Laguna, R. Carles, B. Kohn and F. Huisken. *Improved one-phonon confinement model for an accurate size determination of silicon nanocrystals*. *J. Appl. Phys.*, **86**, 1921–1924 (1999).

- [67] W. A. Brantley. *Calculated elastic constants for stress problems associated with semiconductor devices*. Journal of Applied Physics, **44**(1), 534 (1973).
- [68] Edmund R. Malinowski. *Factor Analysis in Chemistry*. John Wiley, 3 edition (2002).
- [69] E. Anastassakis. *Physical Problems in Microelectronics*. In *Proceedings of the 4th International School ISPPM*, Varan, Bulgaria (1985).
- [70] D. Azulay, I. Balberg, V. Chu, J. P. Conde and O. Millo. *Current routes in hydrogenated microcrystalline silicon*. Physical Review B, **71**(11), 113304, March 2005.
- [71] B. Rezek, J. Stuchlík, A. Fejfar and J. Kočka. *Microcrystalline silicon thin films studied by atomic force microscopy with electrical current detection*. Journal of Applied Physics, **92**(1), 587–593, July 2002.
- [72] B. Rezek, J. Stuchlík, A. Fejfar and J. Kočka. *Local characterization of electronic transport in microcrystalline silicon thin films with submicron resolution*. Applied Physics Letters, **74**(10), 1475–1477, March 1999.
- [73] J. Kočka, A. Fejfar, H. Stuchlíková, J. Stuchlík, P. Fojtík, T. Mates, B. Rezek, K. Luterová, V. Švrček and I. Pelant. *Basic features of transport in microcrystalline silicon*. Solar Energy Materials and Solar Cells, **78**(1-4), 493–512, July 2003.
- [74] J. A. Dagata, T. Inoue, J. Itoh, K. Matsumoto and H. Yokoyama. *Role of space charge in scanned probe oxidation*. Journal of Applied Physics, **84**(12), 6891–6900, December 1998.
- [75] C. Eisele, C. E. Nebel and M. Stutzmann. *Spatially resolved photocurrent measurements of microstructured a-Si:H solar cells*. Journal of Non-Crystalline Solids, **266-269**(Part 2), 1109–1113, May 2000.
- [76] C. Shafai, D. J. Thomson and M. Simard-Normandin. *Two-dimensional delineation of semiconductor doping by scanning resistance microscopy*. In *Second international workshop on the measurement and characterization of ultrashallow doping profiles in semiconductors*, volume 12, pages 378–382, Res. Triangle Park, North Carolina (USA) (1994). AVS.
- [77] B. Rezek, T. Mates, E. Šípek, J. Stuchlík, A. Fejfar and J. Kočka. *Influence of combined AFM/current measurement on local electronic properties of silicon thin films*. Journal of Non-Crystalline Solids, **299-302**(Part 1), 360–364, April 2002.
- [78] M. Nonnenmacher, M. P. O’Boyle and H. K. Wickramasinghe. *Kelvin probe force microscopy*. Applied Physics Letters, **58**(25), 2921–2923, June 1991.
- [79] Takeshi Aiba, Ken Yamauchi, Yuichi Shimizu, Naoto Tate, Masatake Katayama and Takeo Hattori. *Initial Stage of Oxidation of Hydrogen-Terminated Si(100)–2 × 1 Surface*. Japanese Journal of Applied Physics, **34**(Part 1, No. 2B), 707–711 (1995).

- [80] J. A. Dagata, F. Perez-Murano, C. Martin, H. Kuramochi and H. Yokoyama. *Current, charge, and capacitance during scanning probe oxidation of silicon. I. Maximum charge density and lateral diffusion*. Journal of Applied Physics, **96**(4), 2386 (2004).
- [81] A. E. Gordon, R. T. Fayfield, D. D. Litfin and T. K. Higman. *Mechanisms of surface anodization produced by scanning probe microscopes*. In *The 38th International symposium on electron, ion, and photon beams*, volume 13, pages 2805–2808, Scottsdale, Arizona (USA), November 1995. AVS.
- [82] E. S. Snow, G. G. Jernigan and P. M. Campbell. *The kinetics and mechanism of scanned probe oxidation of Si*. Applied Physics Letters, **76**(13), 1782 (2000).
- [83] Phaedon Avouris, Tobias Hertel and Richard Martel. *Atomic force microscope tip-induced local oxidation of silicon: kinetics, mechanism, and nanofabrication*. Applied Physics Letters, **71**(2), 285 (1997).
- [84] N Cabrera and N F Mott. *Theory of the oxidation of metals*. Reports on Progress in Physics, **12**(1), 163 (1949).
- [85] Winfried Mönch. *Electronic Properties of Semiconductor Interfaces*. Springer, 1 edition, November 2004.
- [86] A. Vetushka, A. Fejfar, M. Ledinský, B. Rezek, J. Stuchlík and J. Kočka. *Comment on "Current routes in hydrogenated microcrystalline silicon"*. Physical Review B, **81**(23), 237301, June 2010.
- [87] Zhenhua Shen, Tamihiro Gotoh, Mototaka Eguchi, Norimitsu Yoshida, Takashi Itoh and Shuichi Nonomura. *Study of Nano-Scale Electrical Properties of Hydrogenated Microcrystalline Silicon Solar Cells by Conductive Atomic Force Microscope*. Japanese Journal of Applied Physics, **46**, 2858–2864 (2007).
- [88] A. Fejfar, A. Vetushka, V. Kalusová, O. Čertík, M. Ledinský, B. Rezek, J. Stuchlík and J. Kočka. *Relation of nanoscale and macroscopic properties of mixed-phase silicon thin films*. physica status solidi (a), **207**(3), 582–586 (2010).
- [89] B. E. Pieters, H. Stiebig, M. Zeman and R. A. C. M. M. van Swaaij. *Determination of the mobility gap of intrinsic c-Si:H in p-i-n solar cells*. Journal of Applied Physics, **105**(4), 044502 (2009).

About the author

Curriculum Vitae

Personal data

Name: Aliaksei Vetushka
Date of birth: 8th February 1979
Place of birth: Minsk, Republic of Belarus
Nationality: Belarusian
e-mail: vetushka@fzu.cz

Education

2004–2010 Post-graduate studies at the Faculty of Mathematics and Physics, Charles University in Prague.
(specialization: Quantum optics and optoelectronics)
PhD thesis on *Mechanical and electrical properties of micro-crystalline silicon thin films*.

1996–2001 Graduate studies at the Physics Department of Belarusian State University, Magister degree ‘Mgr.’.
(specialization: Physics of lasers and spectroscopy.)
Master thesis on *Principles of creation of raster images and theirs use in confocal microscopy*.

Research interests

- Structure and electrical properties of amorphous and micro-crystalline silicon thin films, application to solar cells.
- Atomic force microscopy and related scanning probe techniques.
- Raman microspectroscopy and combination with atomic force microscopy.

Work experience

2000–2004 Design engineer of optic equipment, KBTEM-OMO of PLANAR Concern, Minsk, Republic of Belarus.

since 2005 Research worker at Department of Thin Films, Institute of Physics, Academy of Sciences of the Czech Republic, Prague.

Languages

Czech, English, Russian

List of Publications

Impacted scientific journals

1. A. Vetushka, A. Fejfar, M. Ledinský, B. Rezek, J. Stuchlík, J. Kočka *Comment on Current routes in hydrogenated microcrystalline silicon*, Physical Review B **81**, 237301 (2010).
2. A. Fejfar, A. Vetushka, V. Kalusová, O. Čertík, M. Ledinský, B. Rezek, J. Stuchlík, J. Kočka *Relation of nanoscale and macroscopic properties of mixed-phase silicon thin films*, Physica Status Solidi A **207**, 582 (2010).
3. J. Kočka, A. Vetushka, A. Fejfar, *Some controversial points related to transport in microcrystalline silicon*, Philosophical Magazine **89**, 28-30, 2557 (2009).
4. B. Rezek, Šípek, M. Ledinský, J. Stuchlík, A. Vetushka, J. Kočka, *Creating nanocrystals in amorphous silicon using a conductive tip*, Nanotechnology **20**, 4 (2009).
5. T. Baše, Z. Bastl, M. Šlouf, M. Klementová, J. Šubrt, A. Vetushka, M. Ledinsky, A. Fejfar, J. Macháček, M. J. Carr, M. G. S. Londesborough *Gold micrometer crystals modified with carboranethiol derivatives*, Journal of Physical Chemistry C **112**, 14446 (2008).
6. A. Vetushka, M. Ledinský, J. Stuchlík, T. Mates, A. Fejfar, J. Kočka *Mapping of mechanical stress in silicon thin films on silicon cantilevers by Raman microspectroscopy*, Journal of Non-crystalline Solids **354**, 2235 (2008).
7. M. Ledinský, A. Vetushka, J. Stuchlík, T. Mates, A. Fejfar, J. Kočka, J. Stepanek *Crystallinity of the mixed phase silicon thin films by Raman spectroscopy*, Journal of Non-crystalline Solids **354**, 2253 (2008).

Conference proceedings

8. M. Ledinský, A. Vetushka, J. Stuchlík, A. Fejfar, J. Kočka, *Determination of Single Microcrystalline Silicon Grains Preferential Crystallographic Orientation by Polarized Raman spectroscopy*, AIP Conference Proceedings Volume 1267, Pages 1109–1110, 22nd International Conference on Raman Spectroscopy 08. - 13. 08. 2010, Boston, USA

9. A. Vetushka, A. Fejfar, M. Ledinský, B. Rezek, J. Stuchlík, J. Kočka, *Studying of Charge Transport Mechanism in Thin Films of Hydrogenated Microcrystalline Silicon by Conductive Atomic Force Microscopy*, 2nd International Forum on Multidisciplinary Education and Research for Energy Science, 12. - 16. 12. 2009, Okinawa, Japan.
10. M. Ledinský, A. Vetushka, J. Stuchlík, A. Fejfar, J. Kočka, *Investigation of Microcrystalline Silicon Films by Raman Microspectroscopy*, 2nd International Forum on Multidisciplinary Education and Research for Energy Science, 12. - 16. 12. 2009, Okinawa, Japan.
11. Fejfar, A. Vetushka, M. Ledinský, B. Rezek, J. Kočka, *Nanostructured Silicon Thin Films for Solar Cells*, 2nd International Forum on Multidisciplinary Education and Research for Energy Science, 12. - 16. 12. 2009, Okinawa, Japan.
12. Fejfar, A. Vetushka, M. Ledinský, T. Mates, B. Rezek, V. Kalusová, O. Čertík, J. Stuchlík, H. Stuchlíková, E. Šípek, A. J. Kočka, *Relation of Nanoscale and Macroscopic Properties of Mixed Phase Silicon Thin Films*, 2nd Annual Review Meeting of the Thin Film Full Spectrum Solar Cells with Low Concentration Ratios, 20. - 21. 10. 2009, Tokyo Institute of Technology, Japan.
13. A. Vetushka, A. Fejfar, M. Ledinský, B. Rezek, J. Stuchlík, J. Kočka, *Role of the tip induced local anodic oxidation in the conductive atomic force microscopy of mixed phase silicon thin films*, 23. - 28. 8. 2009, Utrecht, The Netherlands, published in *Physica Status Solidi (c)* **7**, 728 (2010).
14. M. Ledinský, A. Vetushka, J. Stuchlík, A. Fejfar, J. Kočka, *Raman mapping of microcrystalline silicon thin films with high spatial resolution*, 23. - 28. 8. 2009, Utrecht, The Netherlands, published in *Physica Status Solidi (c)* **7**, 704 (2010).
15. A. Fejfar, A. Vetushka, V. Kalusová, O. Čertík, M. Ledinský, B. Rezek, J. Stuchlík, J. Kočka, *Relation of Nanoscale and Macroscopic Properties of Mixed-Phase Silicon Thin Films*, 23. - 28. 8. 2009, Utrecht, The Netherlands.
16. A. Vetushka, A. Fejfar, M. Ledinský, B. Rezek, J. Kočka, *The influence of the tip-induced local anodic oxidation on the conductive atomic force microscopy results*, 17th International Symposium NANOSTRUCTURES: Physics and Technology, 26. - 29. 6. 2009, Minsk, Belarus.
17. A. Vetushka, A. Fejfar, M. Ledinský, B. Rezek, J. Stuchlík, J. Kočka, *Probing Charge Transport in Hydrogenated Micro-crystalline Silicon Thin Films with Nanometer Resolution*, EuroNanoForum 2009, Nanotechnology for Sustainable Economy, European and International Forum on Nanotechnology, 2. - 5. 6. 2009, Prague, Czech Republic.

18. M. Ledinský, J. Stuchlík, A. Vetushka, A. Fejfar, J. Kočka, *Decomposition of Mixed Phase Silicon Raman Spectra*, MRS Spring Meeting, 13. 17. 4. 2009, San Francisco, CA, USA.
19. M. Ledinský, A. Vetushka, J. Stuchlík, T. Mates, A. Fejfar and J. Kočka, *Magnetic Field Influence on Deposition of Microcrystalline Silicon Thin Film*, Proceedings of the 21th European Photovoltaic Solar Energy Conference, Dresden, 4.-8. 9. 2006, 3DV.3.50, (2006) WIP-Münich, Germany.

Czech conference proceedings

20. M. Ledinský, A. Vetushka, J. Stuchlík, A. Fejfar, J. Kočka, *Výpočet krystalinity tenké vrstvy křemíku ze spektra Ramanova rozptylu*, 3. česká fotovoltaická conference, 3. - 5. 11. 2008 Brno
21. M. Ledinský, A. Vetushka, J. Stuchlík, J. Čermák, B. Rezek, A. Fejfar and J. Kočka, *Micro-Raman spectroscopy*, Proceedings of the International Summer School – Science and Technology at Nanoscale, Devět Skal, 16.-20. 6. 2008, (editors A. Vetushka, A. Fejfar), FZÚ AV ČR, Praha (2008).
22. A. Vetushka, M. Ledinský, A. Fejfar, J. Kočka, *Raman measurement of intrinsic stress in nanocrystalline silicon thin films*, Proceedings of the International Summer School – Science and Technology at Nanoscale, Devět Skal, 16.-20. 6. 2008, (editors A. Vetushka, A. Fejfar), FZÚ AV ČR, Praha (2008).
23. M. Ledinský, A. Vetushka, J. Stuchlík, T. Mates, A. Fejfar and J. Kočka, *Vliv magnetického pole na depozici tenkých vrstev mikrokrytalického křemíku*, 2. Česká fotovoltaická konference, 12. - 14. 6. 2006, Brno, Oral presentation, Published in conference proceedings.

Unpublished conference contributions

24. A. Vetushka, M. Ledinský, A. Fejfar, J. Stuchlík, J. Kočka, *Charge Transport through Grain Boundaries in Mixed Phase Silicon Thin Films Studied by Conductive Atomic Force Microscopy*, 25th European Photovoltaic Solar Energy Conference, 6. - 10. 09. 2010, Valencia, Spain, oral presentation
25. M. Ledinský, A. Vetushka, A. Fejfar, J. Kočka, *Relative Measurement of Light Trapping in Silicon Thin Films by Raman Spectroscopy*, 25th European Photovoltaic Solar Energy Conference, 6. - 10. 09. 2010, Valencia, Spain.

26. A. Fejfar, V. Kalusová, O. Čertík, A. Vetushka, M. Ledinský, J. Červenka, J. Kočka, *Internal Fields in Nanostructured Silicon Thin Films for Photovoltaics*, 25th European Photovoltaic Solar Energy Conference, 6. - 10. 09. 2010, Valencia, Spain.
27. A. Hospodková, J. Pangrác, J. Vyskočil, J. Oswald, A. Vetushka, O. Caha, P. Hazdra, K. Kuldová, E. Hulicius, *InAs/GaAs quantum dot capping in kinetically or diffusion limited MOVPE growth regime*, 15th International Conference on MOVPE, 23. - 28. 05. 2010, Hyatt Regency lake Tahoe, NV, USA.
28. M. Ledinský, A. Vetushka, J. Stuchlík, A. Fejfar a J. Kočka, *Mapping of semiconducting structures with sub-micron resolution by Raman and photoluminescence spectroscopy*, XII. konference Optické vlastnosti pevných látek v základním výzkumu a aplikacích, 22. - 24. 6. 2009, Brno, PřF, Masarykova univerzita
29. A. Vetushka, A. Fejfar, M. Ledinský, B. Rezek, J. Stuchlík, J. Kočka, *The influence of the tip induced local anodic oxidation on the conductive atomic force microscopy results*, Seminář o metodách blízkého pole, 23. - 24. 3. 2009, Valtice, oral presentation
30. A. Vetushka, M. Ledinský, B. Rezek, A. Fejfar, J. Kočka, *Study of electrical properties of mixed-phase of c-Si:H thin films by ambient conductive AFM*, 3. česká fotovoltaická conference, 3. - 5. 11. 2008 Brno, Oral presentation
31. A. Fejfar, B. Rezek, T. Mates, S. Honda, J. Čermák, M. Ledinský, A. Vetushka, O. Čertík, J. Stuchlík, H. Stuchlíková, E. Šípek, J. Kočka, *Mapping electronic properties of thin films for solar cells with nanometer resolution*, ICN+T 2008, Keystone Resort and Conference Center, Colorado, USA, July 20-25, 2008
32. A. Vetushka, M. Ledinský, J. Stuchlík, T. Mates, A. Fejfar and J. Kočka, *Raman measurement of intrinsic stress in nanocrystalline silicon thin films*, oral presentation, International Conference on Nanoscience + Technology (ICN+T) 2007 2-6.7.2007, Stockholm, Sweden.